Spring 2011

Boundary-constrained inverse consistent image registration and its applications

Dinesh Kumar
University of Iowa

BOUNDARY-CONSTRAINED INVERSE CONSISTENT IMAGE REGISTRATION AND ITS APPLICATIONS

by

Dinesh Kumar

An Abstract

Of a thesis submitted in partial fulfillment
of the requirements for the Doctor of
Philosophy degree in
Electrical and Computer Engineering
in the Graduate College of
The University of Iowa

May 2011

Thesis Supervisor: Professor Gary E. Christensen

ABSTRACT

This dissertation presents a new inverse consistent image registration (ICIR) method called boundary-constrained inverse consistent image registration (BICIR). ICIR algorithms jointly estimate the forward and reverse transformations between two images while minimizing the inverse consistency error (ICE). The ICE at a point is defined as the distance between the starting and ending location of a point mapped through the forward transformation and then the reverse transformation. The novelty of the BICIR method is that a region of interest (ROI) in one image is registered with its corresponding ROI. This is accomplished by first registering the boundaries of the ROIs and then matching the interiors of the ROIs using intensity registration. The advantages of this approach include providing better registration at the boundary of the ROI, eliminating registration errors caused by registering regions outside the ROI, and theoretically minimizing computation time since only the ROIs are registered. The first step of the BICIR algorithm is to inverse consistently register the boundaries of the ROIs. The resulting forward and reverse boundary transformations are extended to the entire ROI domains using the Element Free Galerkin Method (EFGM). The transformations produced by the EFGM are then made inverse consistent by iteratively minimizing the ICE. These transformations are used as initial conditions for inverse-consistent intensity-based registration of the ROI interiors. Weighted extended B-splines (WEB-splines) are used to parameterize the transformations. WEB-splines are used instead of B-splines since WEB-splines can be

defined over an arbitrarily shaped ROI. Results are presented showing that the BICIR method provides better registration of 2D and 3D anatomical images than the small-deformation, inverse-consistent, linear-elastic (SICLE) image registration algorithm which registers entire images. Specifically, the BICIR method produced registration results with lower similarity cost, reduced boundary matching error, increased ROI relative overlap, and comparable inverse consistency error than the SICLE algorithm.

Abstract Approved: _____
Thesis Supervisor

_____
Title and Department

_____
Date

BOUNDARY-CONSTRAINED INVERSE CONSISTENT IMAGE REGISTRATION AND ITS APPLICATIONS

by

Dinesh Kumar

A thesis submitted in partial fulfillment of the
requirements for the Doctor of
Philosophy degree in Electrical and Computer Engineering in
the Graduate College of
The University of Iowa

May 2011

Thesis Supervisor: Professor Gary E. Christensen

Graduate College
The University of Iowa
Iowa City, Iowa

CERTIFICATE OF APPROVAL

PH.D. THESIS

This is to certify that the Ph.D. thesis of

Dinesh Kumar

has been approved by the Examining Committee for the thesis requirement for the Doctor of Philosophy degree in Electrical and Computer Engineering at the May 2011 graduation.

Thesis Committee: _____
Gary E. Christensen, Thesis Supervisor

_____
Joseph M. Reinhardt

_____
Hans J. Johnson

_____
Er-Wei Bai

_____
Mona K. Garvin

ACKNOWLEDGEMENTS

I would like to thank all those who have made this work possible.

First, I would like to thank my advisor, Prof. Gary E. Christensen for providing the opportunity to work with him, for his continued support, guidance and patience. Working with him has been a very enriching and learning experience at an educational as well as personal level. I am grateful to him for being such a great mentor and he remains a role model for me.

I would like to acknowledge the help and support I received from my fellow students and friends, especially Dr. Xiujuan Geng, Paul Joo-Hyun Song, Kunlin Cao and Karthik Alamelumangapuram.

I thank Prof. Gary E. Christensen and Prof. Milan Sonka for providing a productive lab environment and facilities. I would also like to thank the faculty and staff in Electrical and Computer Engineering department for their support. I would like to thank Dr. Joseph M. Reinhardt, Dr. Eric Hoffman and the late Dr. Geoffrey McLennan for their valuable suggestions at various stages of my research.

I would also take this opportunity to thank my parents, Sh. Jai Raj and Smt. Krishna Devi for their continued support and encouragement. Their support made it possible for me to pursue my academic interests. At last, I express my gratitude for my life partner, Ting Ting for her continued support and enduring it with me. It was mainly because of her that I remained motivated and never had any doubts regarding my thesis.

ABSTRACT

This dissertation presents a new inverse consistent image registration (ICIR) method called boundary-constrained inverse consistent image registration (BICIR). ICIR algorithms jointly estimate the forward and reverse transformations between two images while minimizing the inverse consistency error (ICE). The ICE at a point is defined as the distance between the starting and ending location of a point mapped through the forward transformation and then the reverse transformation. The novelty of the BICIR method is that a region of interest (ROI) in one image is registered with its corresponding ROI. This is accomplished by first registering the boundaries of the ROIs and then matching the interiors of the ROIs using intensity registration. The advantages of this approach include providing better registration at the boundary of the ROI, eliminating registration errors caused by registering regions outside the ROI, and theoretically minimizing computation time since only the ROIs are registered. The first step of the BICIR algorithm is to inverse consistently register the boundaries of the ROIs. The resulting forward and reverse boundary transformations are extended to the entire ROI domains using the Element Free Galerkin Method (EFGM). The transformations produced by the EFGM are then made inverse consistent by iteratively minimizing the ICE. These transformations are used as initial conditions for inverse-consistent intensity-based registration of the ROI interiors. Weighted extended B-splines (WEB-splines) are used to parameterize the transformations. WEB-splines are used instead of B-splines since WEB-splines can be

defined over an arbitrarily shaped ROI. Results are presented showing that the BICIR method provides better registration of 2D and 3D anatomical images than the small-deformation, inverse-consistent, linear-elastic (SICLE) image registration algorithm which registers entire images. Specifically, the BICIR method produced registration results with lower similarity cost, reduced boundary matching error, increased ROI relative overlap, and comparable inverse consistency error than the SICLE algorithm.

TABLE OF CONTENTS

LIST OF TABLES

Table

LIST OF FIGURES

Figure

CHAPTER 1
INTRODUCTION

1.1 Overview

In medical imaging, image registration between two similar anatomical objects may be described as finding a mapping that defines a point-to-point correspondence between the objects in the images. This correspondence may be established using set of known corresponding points, contours, surfaces, difference in intensities, mutual information or any combination of these. A "perfect" registration, if obtainable would define such a correspondence uniquely and exactly across the two images and matches each tissue or structure between the two images perfectly up to infinitesimal detail in the continuum. In practice however, a perfect registration is not achievable due to limited information, finite maximum degrees of freedom of the deformation model and lack of precise description of actual process. Instead, the registration problem is often posed as an optimization problem with certain constraints thought to be representative of the actual deformation of the objects. Based on different sets of constraints, there can theoretically be infinite ways of registering two objects together. It is therefore necessary for the mapping defining correspondences to have properties that approximate the desired correspondences.

Splines present an important class of functions and have been very popular as basis functions for image registration.The advantages of splines include spatial parametrization, localization, computational ease, smoothness and good approxima-

tion properties of splines. Most registration methods including popular spline based methods such as Bookstein's Thin Plate Spline method [2], Rueckert et al.'s Free Form Deformation [48], Rohr et al.'s approximating thin plate spline method [46] either perform a landmark based registration or register images based on intensity or mutual information based cost functions. The algorithms of Johnson and Christensen [21] and Kybic et al. [25], [27] combine landmark and intensity information and attempt at finding a registration function that minimizes both. All these methods can perform relatively better than others under certain conditions depending on the application. However, all these methods assume a continuity in deformation across the image. Continuity is imposed by using transformations constructed from continuous functions. Such a framework does not allow for discontinuities anywhere in the image, including outside the region of interest.

The continuity assumption fails to hold when matching anatomical objects. For example, while matching two instances of human lung from same subject at different points in breathing cycle, the lobes slide or rotate against one another. Sliding along lung boundaries is an example of a discontinuity that cannot be accommodated by registration algorithms that use a continuous transformation. This work proposes a new method that matches the object boundaries exactly while performing registration only inside the domain of the object instead of entire image. This approach uses a basis function that is uniformly zero outside the region of interest to parametrize a transformation. Basis functions defined over entire image such as Fourier and B-splines fail to meet this criterion. Hollig's [17] Weighted Extended B-splines (WEB

splines), which are constructed from B-splines using the geometry of the object, have non-zero support only over the region of interest of the defined object and are suitable for the task. WEB-splines provide the motivation for the presented work aimed at developing a new consistent intensity based registration algorithm that registers only region inside object of interest while matching the boundaries exactly. The presented algorithm will be referred to as Boundary-Constrained Inverse Consistent Image Registration (BICIR).

1.2 Previous Work

1.2.1 Registration Methods

Broadly, registration techniques may be classified into two approaches based on the similarity metric: Geometric-Feature based e.g., points or surfaces and Voxel-Feature based, such as intensity, mutual information, etc.

Landmark-based methods rely on identifying corresponding feature points in the two images to be registered and then interpolating the correspondences everywhere else in the image. Bookstein's thin plate spline method [2] offers a closed form solution for landmark registration based on minimizing the thin plate bending energy. This approach is extremely popular among point based techniques. Bookstein's method assumes absolute correspondence between the landmarks and hence assumes that the landmark acquisition is error free. However, it is nearly impossible to acquire perfect landmark locations due to sampling rate of images and a lower limit on errors remains [47]. The problem of landmark localization has been addressed by various researchers. In their work, Chui and Rangarajan [14], [7], [6] address this problem

by finding correspondences between the images using soft-assign and evaluating the confidence in this correspondence iteratively. Rohr et al. [44], [46], [45] compute the correspondence using approximating thin-plate splines, which has a modified matching criterion incorporating the variance of landmark localization error. Johnson and Christensen [21] and Kybic and Unser [25], [27] address this problem by fine tuning the registration using intensity information.

Surfaces represent another type of geometric feature that has been used for image registration. Besl's iterative closest point algorithm [1] matches two point sets or shapes using a rigid body transformation. Thomson and Toga [59], [58] presented surface based elastic registration technique and used it to construct a probabilistic atlas of brain for detection of abnormalities. Finite element methods have also been used to perform surface registration [11], but suffer from the computational overhead of creating meshes. Contour and surface registration techniques typically perform matching based on sampled points along the curves or vertices on the surfaces [13], [3], [62]. Some recent techniques compute correspondences in a parametric space, which is mapped back onto the surface [22], [23], [60].

Voxel based methods employ similarity measures involving intensity of the voxels. Absolute intensity differencemutual information [34], [33], [64], [42], [32] and normalized cross-correlationare the most popular measures of similarity between the two images. While intensity difference measure is ideal for images from same modality, mutual information based measure is more appropriate when comparing images from different modalities. Based on regularization and parametrization, there are a variety

of intensity based registration methods [48], [52], [57], [16], [4], [21]. While most methods are uni-directional, recently there has been emphasis on finding a consistent and transitive correspondence [13], [55].

In general, the landmark and intensity information have been treated separately. Recently, efforts have been made at unifying all the available information to establish the correspondence [21] [61], [25], [26]. The correspondence of images at landmarks obtained based on anatomy may not always be well supported by the surrounding intensity information and vice versa. As a result, the available methods tend to find a trade-off between matching landmarks and matching intensities. The presented method is expected to provide an agreeable solution to the above problem.

1.2.2 Applications of Registration Methods

Image registration has numerous applications in medical imaging ranging from diagnosis, such as registering functional data with structural data, to treatment and monitoring of diseases such as cancer as well as establishing normality vs. abnormality. Image registration is also used to evaluate emerging technologies such as dual energy scans, which is used to enhance contrast in subtraction images of various tissues based on the difference in energy levels of the X-rays. In pulmonary imaging, image registration is used for a number of applications that include construction of a normal lung atlas [28], [29], [31], radiation treatment dose planning [15], atlas based segmentation [65], cancer diagnosis [9], [63], computing regional lung mechanics [41], [53], [12], and modeling of breathing lung [24], [5].

Although there are a wide variety of image registration methods available, reg-

istration of lungs presents specific problems compared to registration of fixed anatomical objects such as brains. For human brains, standards are available for a standard space to which brains can be initially aligned in the form of Talairach space [56]. Likewise, it is easy to identify sulci structures on the surface of brain that can be used as features for surface based registrations. For human lungs, however, there is no standard way of choosing a standard frame of reference for initial alignment as the lung surface is quite smooth and no landmarks can be reproducibly and reliably chosen on it. Likewise, the structure of airway tree differs among individuals. In addition, the deformation model chosen, in general, does not represent the motion of lungs with respect to each other and with respect to the chest wall and even within the lung. The lung lobes have been shown to slide and rotate against each other during a breathing cycle making it hard to address these issues. Researchers have tried to address these issues in different ways to suit various applications and the approaches range from surface/contour based methods to volumetric registration methods.

In their work on computing object shape model for segmentation of human lung, Li and Reinhardt [31] use a contour based approach, in which 2-D boundary contours of the object are registered with each other by curvature minimization. The statistical shape model obtained is used to initialize the lung segmentation through a modified active shape model approach [8]. Although the algorithm was shown to produce good results, it remains application specific and can not be used to register internal structures. The method of segmentation using deformable atlas was also used by Zhang and Reinhardt [65]. The segmentations were defined over the atlas

manually and the atlas was registered with the candidate image. The segmentations defined on the atlas were deformed into the the frame of reference of the candidate image and used as initialization for finer segmentation. The registration is performed by dividing the lungs into small cubes and finding best match fields to register the images based on similarity of cubes. The registration is obtained based on the outer contour using no information from the interior of the object. Li et al. [10] use a feature-points and surface-based approach that evaluates correspondence over sample points on surface along with identifiable feature points to obtain a sparse deformation field. The sparse fields are interpolated over the lung volume using regularization constraint and intensity constraint based on optical flow. This approach combines surface and feature-points correspondence with intensity profile inside the object producing better results at locations away from surface and landmark points.

A contour based approach developed by Mitsa and Qian [38] combines the contour correspondence with internal landmarks. Contours are matched iteratively using Burr's dynamic model [43] based on discretization of contour and iterative deformation of one contour into the shape of a target contour. The landmark points on contour together with internal landmarks are matched using an inverse distance weighted function and thin plate spline method based interpolation, respectively. Woods et al. [63] use feature-points to define "sparse" correspondence at landmark locations and interpolates the deformation to get dense displacement fields. They assume a divergence free, mass conserving model to interpolate the deformation, which is not a valid assumption for lungs. These methods provide a perfect correspondence

at landmark feature-points and use an a priori model to extend correspondence everywhere else. In feature based registration techniques, lack of sufficient feature points and inaccurate models may lead to poor correspondence at locations away from landmarks. While they may be suitable for some applications such as creating a shape model based only on contour or surface, in general, they do not provide accurate correspondence at the voxel level.

Among volumetric methods for lung registration, the usage of inter-modality mutual information based registration has been used for rigid alignment of CT with PET by Haneishi et al. [15]. Their main purpose is to define the segmentations computed on structural scan in the frame of reference of functional images and analyze that data. Mattes et al. [36] use a combination of rigid registration and a b-spline based deformation method to maximize the mutual information between the PET and CT chest scans. The deformation is however is not regularized and relies on smoothness of the underlying b-spline basis function used to parametrize the transformation.

Other intensity based methods used for lung registrations include the following. Gee et al. [12] use an elastic energy regulated model that registers the serial MRI data obtained across breathing cycle of an individual. Dougherty et al. [9] use an unconstrained optical flow method to compute registration between serial CT lung images. Christensen and Johnson's inverse consistent linear elastic image registration method [4] has been used for registering human lungs for quantifying regional lung mechanics [53] and for computing a normative lung atlas [28], [29]. Johnson and

Christensen's consistent intensity and landmark registration method [21] takes advantage of the landmark correspondence with intensity registration has been used in registering sheep lungs for computing regional mechanics [41]. The inverse consistency constraint ensures that the correspondences defined are consistent and ambiguity in correspondences are minimized.

The methods discussed above perform relatively better than others under certain conditions and no single method provides a perfect registration. In some cases such as inter-subject registration, the correspondence problem is ill-posed as the airways across individuals may not correspond. Likewise, the small deformation model assumed by most volumetric registration methods may not be valid when registering FRC (Functional Residual Capacity) to TLC (Total Lung Capacity) images. Due to limitations of the individual methods listed above, it is a good idea to combine all the available information to improve registration results. As already discussed, methods of Johnson and Christensen [21] and Kybic and Unser [27] combine landmark registration with intensity based registration to get a better registration. An inverse consistent registration generates confidence in the results obtained, since the correspondences are consistent regardless of direction of registration, and is therefore a desirable quality.

As previously stated, most volumetric registration methods assume a continuity in deformation across the image. Such an assumption may not be valid for organs such as lungs which slide against chest wall during breathing. The lobes of lungs slide and rotate against each other during breathing making such an assumption invalid.

Some researchers address this by treating both lung separately by extracting and registering them separately [30], [65], [54], [41], but in all cases, the images are treated and registered as a whole. Registration methods tend to register the entire images or a rectangularly shaped region and implicitly impose unnatural boundary conditions for registrations. The b-spline based methods [48], [27], [6] require an extension of boundaries to account for deformation near the image boundaries and methods using Fourier series parameterizations [4], [21] assume periodic boundary conditions. Based on the deformation model, the image boundaries act as hard constraints, thus limiting the deformation of the object of interest through energy regularization constraints. The problem is often addressed using padding with slices having zero values such that the object has enough "room" to deform. Padding may also be required for Fourier series parametrization to obtain appropriate image dimensions to take advantage of Fast Fourier Transform. While image boundaries present unnatural and unnecessary boundary constraints on deformation, padding increases the image size and adds to computation time. Likewise, registration of features outside the region of interest adds computational costs and may adversely affect the registration inside the object.

The Boundary-constrained Inverse Consistent Image Registration (BICIR) algorithm described in this work, provides a better correspondence for irregularly shaped ROIs by registering only region inside the object of interest. The BICIR method does not require padding and treats everything outside the region of interest as a "don't care". This avoids interference of background with the registration of object.

The remainder of the thesis is organized as follows:

Chapter 2 provides the details of algorithm and the methods used in implementation and characeterization of algorithm and comparison methods used against Small Deformation Inverse-Consistent Linear Elastic (SICLE) image registration technique [4], which is similar to the presented technique except the boundary constraints.

Chapter 3 presents the results obtained for the methods described in Chapter 2. Finally, conclusions of the studies are presented in Chapter 4.

CHAPTER 2
METHODS

This chapter presents the theoretical framework and methods involved in development of the boundary-constrained inverse consistent image registration (BICIR) algorithm. The theoretical framework is discussed along with the characterization and validation methods as well as computation of average lung shape using the presented registration technique. The chapter is organized as follows:

Section 2.1 provides the details of theoretical framework and implementation of the BICIR algorithm. This section describes the three steps of the BICIR algorithm starting with the boundary matching, extension of boundary match to the interior of the region and finally, the intensity registration of the interior region.

Section 2.2 provides the details for experimental validation and comparison with existing small-deformation inverse consistent linear elastic (SICLE) image registration method [4].

2.1 Boundary-Constrained Inverse Consistent Image Registration (BICIR) Algorithm

Boundary-constrained inverse consistent image registration (BICIR) assumes that the boundary correspondence is given as input and kept fixed throughout registration. The boundary correspondence is interpolated to the interior of the region of interest using the Element Free Galerkin Method (EFGM). The ROI internal correspondence is then fine-tuned using the intensity information inside the ROI while

keeping the boundaries fixed. The BICIR framework uses a shape-based basis function called WEB-splines (Weighted Extended B-splines), which are derived from regular B-splines to parametrize the correspondence map or transformation between ROIs.

2.1.1 Overall Scheme

Fig. 2.1.1 shows the flowchart describing the steps of the BICIR algorithm. The algorithm has the following steps:

1. Extraction of the object surface (section 2.1.2): The first step is to extract the boundaries of ROI from the gray-scale image. The current work does not focus on the segmentation techniques and uses standard techniques.

2. Consistent boundary matching (section 2.1.3): The extracted boundaries are registered using transitive, inverse-consistent, boundary matching method (TICMR) [13] . The boundary correspondences are treated as essential boundary conditions for the Element Free Finite Element Method.

3. Interpolation Using Element Free Galerkin Method (section 2.1.4): The boundary correspondences are extended to the interior of the object using the Element Free Galerkin approach based on the differential equation describing the energy functional. The images are subdivided into a uniform rectangular (for 2-D, and cubic for 3-D) grid. A WEB-spline basis is constructed based on object boundaries over this grid. The system equations are solved for coefficients of the basis functions using the essential boundary conditions described in step 2. The closed form solution interpolates the correspondence over within the entire

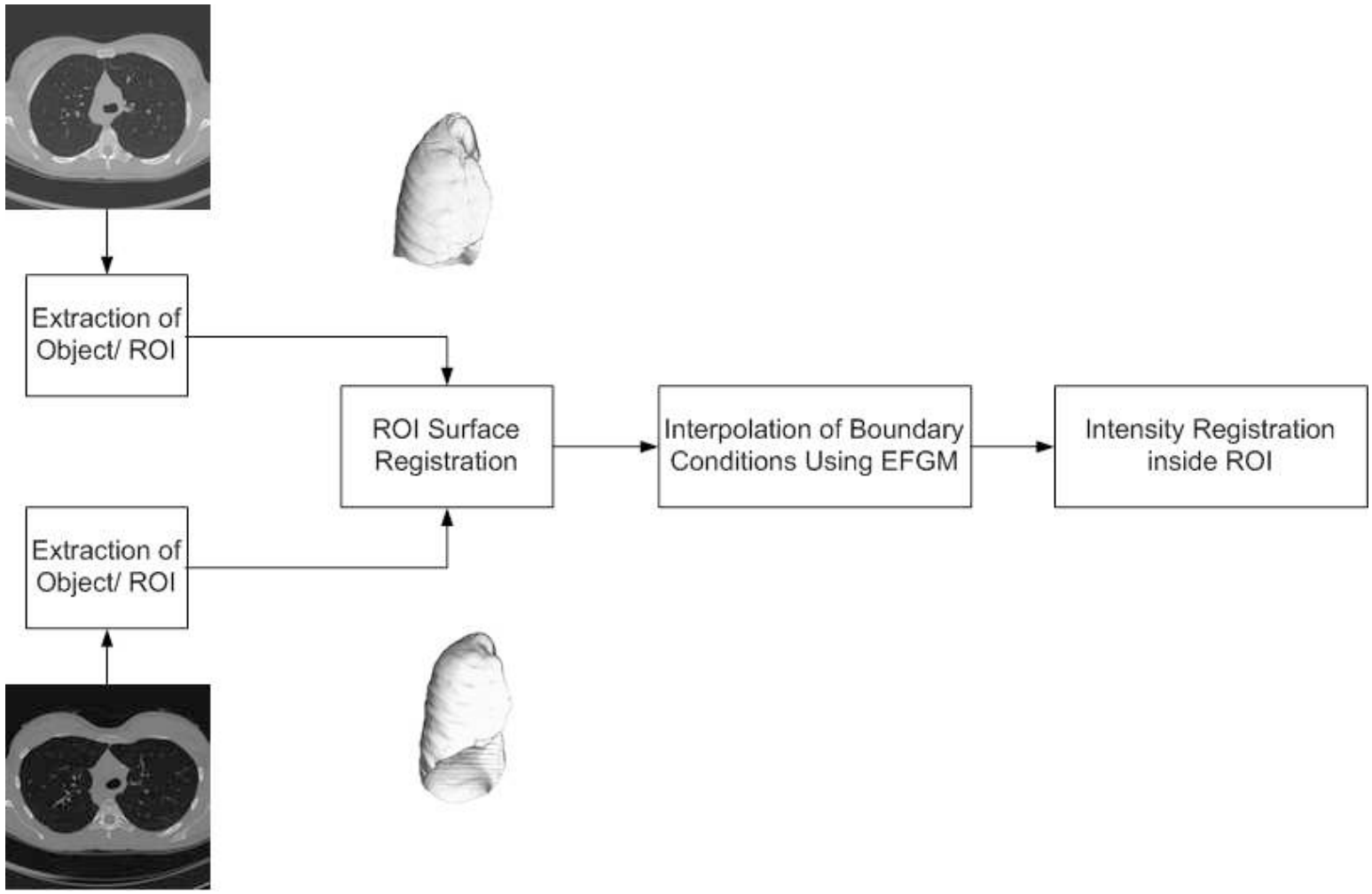

Figure 2.1: The boundaries of the objects to be registered are extracted and registered to compute the boundary correspondence. The element free Galerkin method is used to interpolate the boundary registration to the interior of the object. The correspondence inside the ROI is further fine-tuned using boundary-constrained intensity based image registration.

object domain.

4. Boundary-constrained Inverse Consistent Intensity Registration (section 2.1.5): The correspondence defined by solving the Galerkin system equation is fine-tuned using intensity information inside the object domain. The construction of WEB-splines ensures that the intensity based registration does not compete with boundary matching, as the boundaries are always matched exactly, and only correspondences in the interior of the object are estimated. The deformation coefficients are updated iteratively using gradient descent optimization until a preset stopping criterion is reached.

2.1.2 Extraction of the Object Surface

Boundary extraction involves segmenting the object from the gray-scale image data. In our work, the object was segmented using intensity thresholding. Holes were filled using morphological closing operation followed by manual editing, if necessary. Object pixels (Voxels in 3-D) having background pixels (voxels in 3-D) in 4-neighborhood (6-neighborhood in 3-D) were classified as the boundary pixels that represent the surface of the object. The surface is assumed to pass through the center of the boundary pixels.

2.1.3 Consistent Boundary Matching

After extraction of the boundaries of the object in the two images, the correspondence at the boundaries is computed using Geng et al.'s transitive inverse consistent manifold registration (TICMR) method [13]. This method uses a closest

distance based similarity measure and a curvature based energy regularization with inverse-consistency and transitivity constraints. TICMR algorithm is implemented by minimizing the following cost function:

$$C = C_{SIM} + C_{REG} + C_{ICC} + C_{TRANS} \tag{2.1}$$

The various cost components are described below.

2.1.3.1 Similarity Cost

In this method, for two surfaces, S_1 and S_2, a closest distance similarity cost function is defined over the surfaces, i.e.,

$$C_{SIM} = \sum_{i=1}^{3} \sum_{\substack{j=1 \\ j \neq i}}^{3} \int_{S_j} ||D_{S_i}(h_{ij}(x))||^2 dx \tag{2.2}$$

where D_{S_i} corresponds to the distance map of S_i, i.e., $D_{S_i}(x)$ gives the closest distance from point x to S_i. The manifold S_i represents a contour for contour-to-contour matching or a surface for surface-to-surface matching. The distance maps were computed using Voronoi Feature Transform (VFT) presented in Maurer et. al [37].

2.1.3.2 Regularization Cost

The similarity measure alone does not take the neighborhood structure of the surface S_i into account. Curvature based regularization is used to constrain the registration to produce spatially smooth correspondence. Equation 2.3 represents the regularization cost term used by Geng et al. for contour-to-contour registration in

2D.

$$C_{REG} = \sum_{i=1}^{3} \sum_{\substack{j=1 \\ j \neq i}}^{3} \int_{S_j} || \frac{dh_{ij}(x(s))}{ds} - \frac{dx(s)}{ds} ||^2 ds \tag{2.3}$$

where, s represents the arc length of the curve and $h_{i,j} = x + u_{i,j}(x)$ represents the transformation from contour i to contour j. The cost term represented by Eq. 2.3 penalizes the change of tangent vector along the deforming curve. A Eulerian frame of reference is used for registration.

The regularization used for surface matching is different from contour matching, since the points in a surface are not ordered. The deformation energy function for the surface deformation is represented by the equation 2.4 [20, 13].

$$C_{REG} = \sum_{i=1}^{3} \sum_{\substack{j=1 \\ j \neq i}}^{3} \int_{S_j} (H(h_{ij}(x)) - H_{S_j}(x))^2 a(h_{ij}(x)) dx \tag{2.4}$$

where, $a(x)$ represents the area around point x, $\sum_x a_x$ represents the total surface area and H represents the mean curvature of the surface.

2.1.3.3 Inverse Consistency Cost and Projection Error

Eq. 2.5 represents the inverse consistency cost used to regularize the transformation such that the inverse consistency in correspondence is minimized as part of the registration cost.

$$C_{ICC} = \sum_{i=1}^{3} \sum_{\substack{j=1 \\ j \neq i}}^{3} \int_{S_j} ||h_{ij}(x) - f_{ij}(x)||^2 dx \tag{2.5}$$

where $f_{ij}(x) = \arg\min_{y \in S_i} ||h_{ji}(y) - x||^2$. Note that there are two types of errors that contribute to the above cost function; the inverse consistency and the projection error. In the TICMR method, the correspondence between points is defined through minimum distance between the points. Using f_{ij} instead of h_{ji} in equation 2.5 removes contribution of projection error to the inverse consistency cost such that based on closest neighbor definition of correspondence, only inverse consistency error contributes to the above cost.

2.1.3.4 Transitivity Cost

Transitivity of transformations is another important property. It implies that in a group of images, the correspondence between a pair of images will not change for the set of all composition of transformations in the group that operate on the two images. For example, in a group of three images, I_1, I_2 and I_3, let $h_{i,j}$ represent the transformation from image I_i to I_j, where $i, j \in \{1, 2, 3\}$, then transitivity implies that $h_{i,k} = h_{j,k} \circ h_{i,j}$ for $k \in \{1, 2, 3\}$ and $k \neq i, j$.

In TICMR, the transitivity cost is minimized as part of the registration cost and represented by equation 2.6.

$$C_{TRANS} = \sum_{i=1}^{3} \sum_{\substack{j=1 \\ j \neq i}}^{3} \sum_{\substack{k=1 \\ k \neq i \neq j}}^{3} \int_{S_j} ||h_{ik}(h_{kj}(x)) - h_{ij}(x)||^2 dx. \tag{2.6}$$

2.1.4 Interpolation Using Element Free Galerkin Method

The surface registration method described in section 2.1.3 provides correspondence only at the boundaries of the ROI. The boundary correspondence is interpo-

lated over the interior of the object using a finite element technique called element free Galerkin method (EFGM) [39]. The primary advantage of the element free Galerkin method over traditional finite element methods is that meshing of the object, which is a computationally expensive process, is not required. In addition, we use a shape-based basis function called weighted-extended B-splines (WEB-splines), which can be constructed over an arbitrary shape such that they are non-zero only over the region of interest and zero every where else.

2.1.4.1 Problem Overview

The problem of matching boundaries of objects from two different images can be represented by the boundary value problem represented by Eq. 2.7.

$$\begin{aligned} f(u_{i,j}(x)) &= 0,\ x \in \Omega_j \\ u_{i,j}(x)|_{\partial\Omega_j} &= u_{\Delta i,j}(x),\ x \in \partial\Omega_j \end{aligned} \tag{2.7}$$

where, f is a differential operator representing energy constraints. The equation is solved in both directions, i.e., for $[i, j] = [1, 2]$ and $[i, j] = [2, 1]$, respectively.

The boundary value problem is described as the combination of a differential equation governing the displacement over the object domain and the boundary conditions obtained as a result of surface registration. Let Ω_1 and Ω_2 represent the two regions of interest to be registered, and $\partial\Omega_i$ represent the boundary of the object Ω_i. The previous step of surface registration provides displacement field $u_{\Delta i,j}(x),\ x \in \partial\Omega_j$ that maps $\partial\Omega_i$ onto $\partial\Omega_j$. In our boundary-constrained registration method, the boundaries of the objects remain fixed after initial matching. The boundary corre-

spondences from the surface registration method provides the value of displacements $u_{\Delta i,j}(x)$ as the essential boundary conditions. The boundary value problem represented by Eq. 2.7 is solved for displacement field $u_{i,j}(x),\ x \in \Omega_j$ over the entire region of interest Ω_j.

B-Splines provide good approximation, computationally efficient techniques as well as good localization for smooth functions. However, a B-spline basis can only be used for a rectangular domain and can not be used to represent arbitrarily shaped domains. The element free Galerkin method does not require a meshing of the object, which is usually a computationally expensive step. Instead, a regular grid is used and the boundary conditions are enforced using weight functions. Although B-splines are local in the sense that at a point only a limited number of b-splines are non-zero, they do not fall off to zero at the boundaries. If the b-splines are defined over a regularly spaced grid, there may be b-spline functions supporting only a small portion of the object. B-splines that support a small portion of the ROI cause the system to have a high condition number and may also cause loss of accuracy in approximation. Hollig et al. [17] addressed this problem by defining a new basis function called Weighted Extended B-Splines, or simply WEB-splines. The splines having very little support inside the object boundaries, which Hollig et al. [17] defined as outer splines cause highly sensitive and unstable Galerkin framework. The WEB-splines are defined only on knot points excluding the indices for the outer splines. The outer splines are taken into account using Marsden's identity. The new function is defined on the object domain and presents itself as a good basis to represent the deformations inside the

object domain, once the boundaries are matched. The following subsections will cover the b-splines and construction of WEB-splines from b-splines.

2.1.4.2 B-Splines

Splines are piecewise polynomial functions used to represent a smooth function over a domain, and provide a local approximation. A spline of degree m over a grid with distance between knot points h is $(m-1)$ times continuously differentiable and has its support limited to total length of $(m+1)h$. Over a uniform grid, the B-spline β^m of degree m is defined by the following recursion property:

$$\beta^m(x) = \int_{\frac{x}{h}-1}^{\frac{x}{h}} \beta^{m-1}(x)dx \tag{2.8}$$

with

$$\beta^0(x) = \begin{cases} 1, & 0 \leq \frac{x}{h} < 1 \\ 0, & otherwise \end{cases} \tag{2.9}$$

In general, cubic b-splines, which have order of 3 and have a support of 4 have been found to provide a good approximation without being computationally expensive [25], [48]. Based on the above definition, cubic b-spline starting at a grid knot point, or index i, can be written as:

$$\beta_i^3(x) = \begin{cases} 2/3 - (1 - |\frac{x}{h} - i - 2|/2)(\frac{x}{h} - i - 2)^2 & if\ 0 < |\frac{x}{h} - i - 2| \leq 1 \\ (2 - |\frac{x}{h} - i - 2|)^3/6 & if\ 1 < |\frac{x}{h} - i - 2| \leq 2 \\ 0 & otherwise \end{cases} \tag{2.10}$$

where, h is the knot spacing. Any one-dimensional smooth function $f(x)$ over a domain Ω having n equally spaced knot-points x_i's can be approximated using the cubic b-splines as follows:

$$f(x) = \sum_{k=0}^{3} \mu_{i+k} \beta^3_{i+k}(x) \ \forall x \in (ih, (i+3)h) \tag{2.11}$$

where the parameters μ_i's define the relative weights of the contributing b-splines over the interval and $x_{i+1} = x_i + h$.

For a multidimensional case, we define splines as

$$b^3_i(x) = \prod_{d=1}^{n} \beta^3_{i_d}(x_d) \tag{2.12}$$

where $i = \{i_1, i_2, \ldots, i_n\} \in \mathcal{Z}^n$ and $x = \{x_1, x_2, \ldots x_n\} \in \Omega \subset \mathcal{R}^n$ for an n-dimensional space. In such a space, a function can be parameterized using multi-dimensional splines as follows:

$$f(x) = \sum_{k_n=0}^{3} \ldots \sum_{k_1=0}^{3} \mu_{i_1+k_1, \ldots i_n+k_n} \beta^3_{i_1+k_1}(x_1) \ldots \beta^3_{i_n+k_n}(x_n) \tag{2.13}$$

where $\mu_{i,j}$ represent the control point, or coefficient for parameterization on for knot located at index i, j.

2.1.4.3 Weighted Extended B-Splines

B-spline functions are not particularly well suited for use in element free Galerkin method, since it causes a very high conditioning number due to splines

supporting only part of a boundary cell. The term "cell" in this text will refer to an element described by knot points as its end points in all directions, i.e., for a 1-dimensional case, a cell will consist of the part of the real line between two consecutive knot points. Likewise, for a 2-dimensional case, for knot points defined on rectangular grid, it will be defined as a rectangle (or square, if x- and y- knot spacings are same) with knot points at its four corners as shown in Fig. 2.2 and so on for higher dimensions. Based on this definition of a cell, an image can be divided into a number of cells.

Given an object of interest contained in the image $I(x)$, the cells can be partitioned into three basic categories:

1. *Interior Cells*: These are the cells that are contained inside the object domains, and do not contain any point that lies on the boundary of the object or outside it.

2. *Boundary Cells*: The cells that contain at least one point from the boundary of the object are called boundary cells.

3. *Exterior Cells*: This category consists of the cells that are neither interior nor boundary cells, i.e., cells that do not contain any point that lies inside or on boundary of the object of interest.

Fig. 2.2 shows the three different type of the cells for an object defined on a 2-D domain using an equal horizontal and vertical knot spacing.

Based on these definitions, we define inner, outer and exterior splines as shown

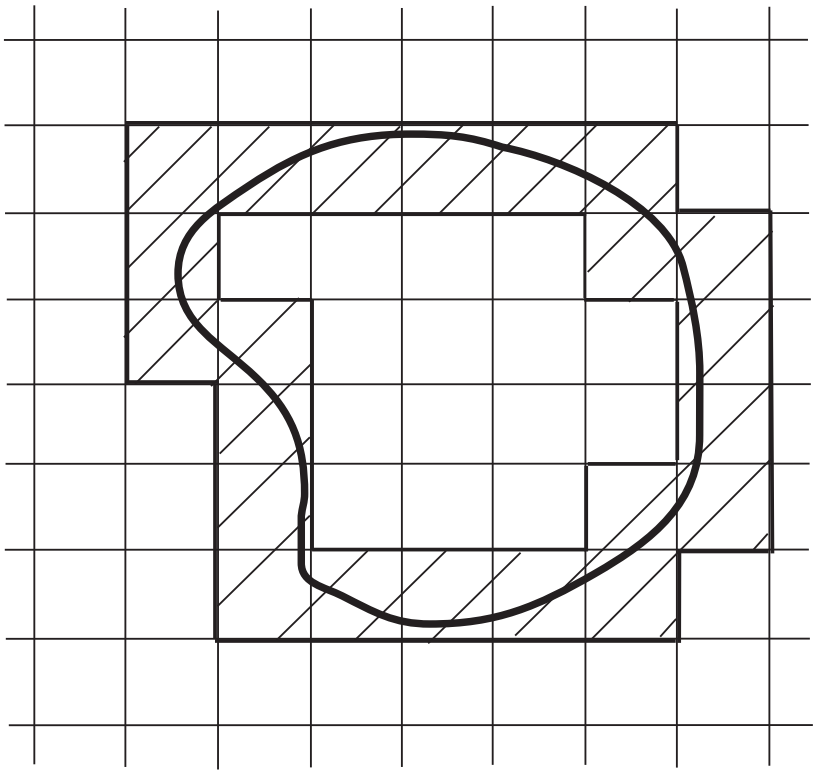

Figure 2.2: Partitioning of grid into inner, outer and interior cells. The thick black closed curve represents the region of interest and the exterior, interior and boundary cells are represented by the white cells, cells marked with crosses and hatched cells, respectively.

in Fig. 2.3. The *inner splines* are defined as the splines that have support of at least one interior cell. The *outer splines* are defined as the splines that have only boundary cells or exterior cells in their support. The exterior splines are the splines that do not have any support over the object of interest. It is easy to see that any method for directly updating the coefficients of outer splines will cause a very sensitive response due to very limited support. In element free Galerkin method, this presents a problem since it causes Galerkin matrix to become very ill-conditioned and renders it unusable

for this usage. Hollig [18], [17], [19] addressed this problem by defining a new basis function called Weighted Extended B (WEB) -splines. The outer splines are taken into account using Marsden's identity [17]: and the WEB spline coefficients are evaluated only on the knot locations of the inner splines.

WEB Splines are defined such that they are non-zero only over the object domain and are zero everywhere else. Let $B_i(x)$ be the basis function representing the WEB-Splines. It can be computed using the inner and outer b-splines over the object domain. Let, the set of inner indices, i.e., indices of knot point locations where inner splines start be denoted by I and the set of outer indices be denoted by J, respectively. The web splines are then constructed using Marsden identity for approximating polynomials using b-splines. By construction, WEB splines combine the support of outer splines with the inner splines and are computed at the inner spline indices. This is done using Eq. 2.14.

$$B_i(x) = \frac{w(x)}{w(x_i)}[b_i(x) + \sum_{j \in J(i)} e_{i,j} b_j], i \in I \tag{2.14}$$

where, b_i and b_j's are the ordinary b-spline function values at location x starting at inner spline index i and outer spline indices j's, respectively and $w(x_i)$ represents the value of weight function at the center of interior cell in the support of inner spline starting at index i. The set $J(i)$ represents the set of all outer spline indices, which are closest to inner index i using the following rule:

$$J(i) = \{j \in J | i \in I(j)\} \tag{2.15}$$

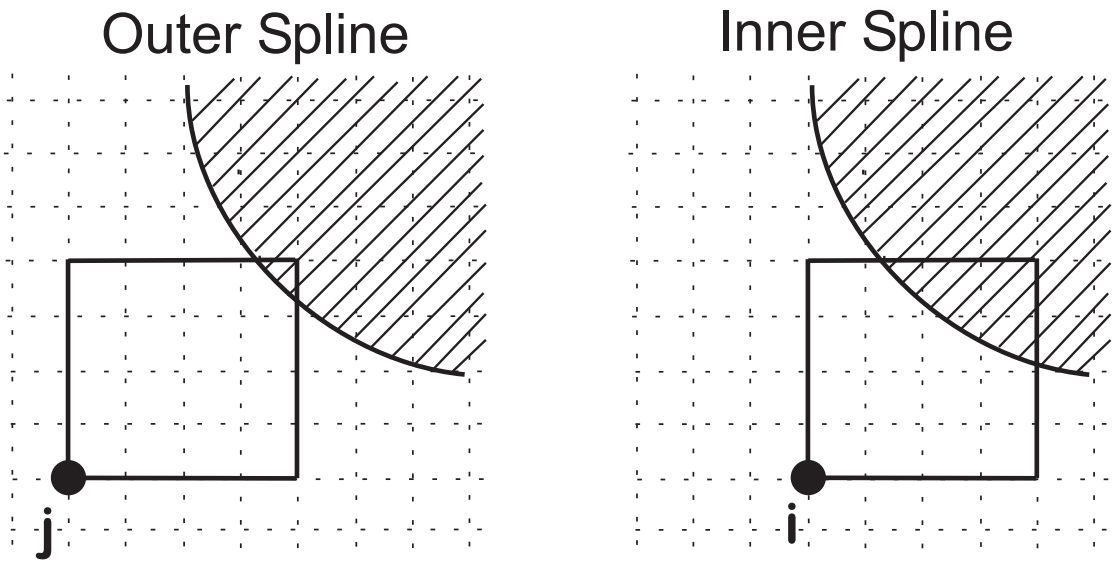

Figure 2.3: The first panel shows the support of an inner spline, starting at index i which contains (at least) one interior cell, marked by x. The second panel shows the support of an outer spline, starting at index j which does not contain any interior cells, but contain one (or more) boundary cells. The starting knot location of splines are marked by circles. The support is shown for splines of the order 3, i.e., of cubic order, hence the support is over $[0, 4]^2$ cells.

where $I(j)$ is the array of inner spline indices closest to the outer index j according to Hausdorff metric. Such an array always exists provided that the grid spacing is small enough and may be given by following equation:

$$I(j) = l + \{0, 1, \ldots, m\}^n \subset I \tag{2.16}$$

Hollig et al. proposed a closed form for the co-efficients $e_{i,j}$ based on Marsden identity as given by the following equation.

$$e_{i,j} = \prod_{\nu=1}^{n} \prod_{\mu=1, \mu \neq (i_\nu - l_\nu)}^{m} \frac{j_\nu - l_\nu - \mu}{i_\nu - l_\nu - \mu} \tag{2.17}$$

In order to limit the support of WEB-splines to the object domain, the weighting function $w(x)$ in Eq. 2.14 is defined such that it is non-zero only over the object domain and is a function of distance from the object boundaries. The weight function $w(x)$ is similar to a distance function from the boundaries, and can be defined in a number of ways. The necessary properties of weight function include smoothness and non-zero support over the region of interest and a zero value at boundaries of object and everywhere outside it. There are a number of ways to construct it automatically [17], [50], [49]. In the absence of a parametric representation of object shape, the construction of weight function will be done using a distance function, e.g., function represented by Eq. 2.18 is valid weight functions.

$$w(x) = 1 - max(0, 1 - dist(x, \partial D)/\delta)^\gamma, \tag{2.18}$$

where, the parameter δ controls the width of the strip $D - D_\delta$ and γ controls the smoothness of the function. Caution is required in choice of width of the strip, as too narrow width can cause large derivatives of weight function.

2.1.4.4 Parameterization of Displacement Field

The boundary value problem described in Eq. 2.7 is solved for displacement field $u_{i,j}(x),\ x \in \Omega_j$. The solution is decomposed into two components: $u^*_{i,j}(x)$ and $u_{\partial i,j}(x)$. The component $u^*_{i,j}(x)$ is parameterized using WEB-splines constructed

using the shape of Ω_j. Due to properties of WEB-splines, $u^*_{i,j}(x)$ is zero at the boundaries and hence, $u_{\partial i,j}(x)$ is used to explicitly approximate the boundary correspondence provided by the surface registration. $u_{\partial i,j}(x)$ is a smooth function that approximates the boundary conditions, and gradually decreases to zero away from boundaries. The main purpose of the extension function $u_{\partial i,j}(x)$ is to approximate and extend the boundary conditions to a region with non-zero measure. The solution $u_{i,j}(x)$ is represented as the sum of two functions $u^*_{i,j}(x)$ and $u_{\partial i,j}(x)$, i.e., $u_{i,j}(x) = u^*_{i,j}(x) + u_{\partial i,j}(x)$

The boundary extension function $u_{\partial i,j}(x)$ can be an arbitrary smooth function and any deviations from following the constraints inside the object are taken into account through $u^*_{i,j}(x)$. In other words, only the solution $u_{i,j}(x) = u^*_{i,j}(x) + u_{\partial i,j}(x)$ needs to satisfy the governing differential equation, while individual components $u^*_{i,j}(x)$ and $u_{\partial i,j}(x)$ may be arbitrary smooth functions.

In the presented work, $u_{\partial i,j}(x)$ is initialized as a delta function with $u_{\partial i,j}(x) = u_{\Delta i,j}(x)$ for $x \in \partial\Omega_j$ and $u_{\partial i,j}(x) = 0$ for $x \notin \partial\Omega_j$, and a Laplacian convolution filter is applied to the image a number of times till a smooth function is obtained. The function $u^*_{i,j}(x)$ is parameterized as a sum of WEB-spline basis functions, i.e.,

$$u^*_{i,j}(x) = \sum_n \mu_{i,j_n} B_n(x) \tag{2.19}$$

where, B_n represents the WEB-spline basis as described in the section 2.1.4.3.

2.1.4.5 Weak Form Formulation

The system in equation 2.7 has the following weak form for $f = \nabla^2 = \frac{\partial^2}{\partial x_1^2} + \frac{\partial^2}{\partial x_2^2} + \frac{\partial^2}{\partial x_3^2}$:

$$\int\int\int \phi(x) \left[\frac{\partial^2 u_{i,j}}{\partial x_1^2} + \frac{\partial^2 u_{i,j}}{\partial x_2^2} + \frac{\partial^2 u_{i,j}}{\partial x_3^2} \right] dx_1 dx_2 dx_3 = 0 \tag{2.20}$$

where, $\phi(x)$ is any smooth weighting function, which is non-zero inside the region of integration. In the Galerkin procedure, it is chosen to be same as the shape function, i.e., WEB splines in our case. $\phi(x) = B_n(x)$, where $B_n(x)$ is the web spline at index element $n = n_1, n_2, n_3{}^t$ and is defined in equation 2.14.

2.1.4.6 Derivation of the Governing Differential Equation

We consider the linear elasticity operator for the transformation $u(x)$, i.e., we seek to minimize the following cost function:

$$C_{LE}(ux)) = \int_\Omega ||\mathcal{L}u(x)||^2 dx \tag{2.21}$$

where $h(x) = x + u(x)$ is the transformation that defines a correspondence mapping. The linear elasticity operator $\mathcal{L}$ has the form

$\mathcal{L}u(x) = \nabla u(x)$ and $\nabla = \left[\frac{\partial}{\partial x_1}, \frac{\partial}{\partial x_2}, \frac{\partial}{\partial x_3} \right]$ for the 3-dimensional case. This leads to the following governing differential equation derived using variational methods:

$$\frac{\partial^2 u}{\partial x_1^2} + \frac{\partial^2 u}{\partial x_2^2} + \frac{\partial^2 u}{\partial x_3} = 0 \tag{2.22}$$

where, the solution $u(x) = [u_1(x), u_2(x), u_3(x)]$ and $x = [x_1, x_2, x_3]$.

2.1.4.7 Weak Form

The weak form for the equation 2.20 can be written as:

$$\begin{aligned}\int\int \left(\frac{\partial B}{\partial x_1}, \frac{\partial B}{\partial x_2}, \frac{\partial B}{\partial x_3}\right) \left(\frac{\partial u}{\partial x_1}, \frac{\partial u}{\partial x_2}, \frac{\partial u}{\partial x_3}\right) dx_1 dx_2 dx_3 = \\ -\int\int \left(\frac{\partial B}{\partial x_1}, \frac{\partial B}{\partial x_2}, \frac{\partial B}{\partial x_3}\right) \left(\frac{\partial u_\partial}{\partial x_1}, \frac{\partial u_\partial}{\partial x_2}, \frac{\partial u_\partial}{\partial x_3}\right) dx_1 dx_2 dx_3\end{aligned} \tag{2.23}$$

where, u_∂ is the function representing extended boundary conditions. The boundary extension function may be computed in a number of ways. We shall investigate two techniques: approximation using b-spline basis and iteratively smoothing the boundary matching delta functions using Laplacian filter. The two techniques shall be compared in Chapter 3. For approximation using b-splines, the b-spline coefficients $c_{i,j,k}$ are computed such that the boundary extension function satisfies the boundary conditions in a least square sense.

$$u_\partial = (u_{\partial,1}, u_{\partial,2}, u_{\partial,3}) = \sum_{k=n}^{n+3} \sum_{j=m}^{m+3} \sum_{i=l}^{l+3} c_{i,j,k} b_{i,j,k}(x). \tag{2.24}$$

Using the basis function representation for $u^*(x)$ and $u_\partial(x)$ from equations 2.19 and 2.24, the weak form in equation 2.23 for an element can be written as the following matrix equation:

$$A_e \ \mu_e = -B_e \ c_e \tag{2.25}$$

Matrices for all the grid points can then be assembled together to form a global matrix equation:

$$A \ \mu = -B \ c \tag{2.26}$$

The construction of global matrices A, B and c can be done using the following method:

$$a_{i,j} = a_{i,j} + a_{e_{k,l}} \tag{2.27}$$

where k and l are the local indexes of the local stiffness matrix A_e and i, j are the corresponding global indexes of the global system matrix A. $a_{i,j}$ represents (i, j)-th element of the strain matrix A. The same can be done for computing global B matrix and a global c matrix. With A and b available as a result of evaluation of weak form integrals over each rectangular element on the grid, and C also known in advance as a result of boundary matching using b-splines, the equation 2.26 can be solved for μ.

2.1.5 Boundary Constrained Inverse Consistent Intensity Registration

The intensity based image registration between two images can be stated as the problem of finding a transformation between the images such that the intensity difference between the images is minimized as a result of the transformation. It is assumed that a good correspondence is achieved when difference between image intensities of the two images is minimized. For physical as well as mathematical reasons, we seek such a transformation , denoted as $h(x)$ in the space of smooth and inverse-consistent transformations. Inverse consistency means that the transformation obtained in one direction is inverse of the transformation obtained in the opposite direction. For example, if we are matching one image $T_i(x)$ with another image $T_j(x)$ and let us denote by $h_{i,j}(x)$, the transformation from image $T_i(x)$ to image $T_j(x)$ in Eulerian co-ordinate system and denote by $h_{j,i}(x)$ the transformation from image $T_j(x)$ to $T_i(x)$, then the

transformation is said to be inverse-consistent if $h_{i,j}(x) = h_{j,i}^{-1}(x)$. In their work, Christensen and Johnson [4] minimize the inverse consistency constraint by adding a cost term for deviation from inverse consistency. Smoothness of transformation is achieved by adding an inverse consistent cost term. Let $u(x)$ denote the displacement at the voxel location x giving the transformation $h(x) = x + u(x)$. The total cost function to be minimized is shown in equation 2.32.

2.1.6 Registration as Optimization Problem

The intensity based image registration problem can be stated as a minimization problem of finding optimal transformations $\hat{h}_{i,j}$ and $\hat{h}_{j,i}$ that minimize the following cost function:

$$C = \sigma C_{Sim} + \rho C_{Reg} + \chi C_{ICC} \tag{2.28}$$

where the three components of cost represent the similarity cost, regularization cost and inverse consistency cost, respectively. These components are discussed in details as follows:

2.1.6.1 Similarity Cost

Similarity cost, denoted by C_{Sim} in Eq. 2.28 represents the driving function of the registration and is minimized when the image intensities match each other. The similarity cost may be computed as the difference between the intensities of deformed reference image and the target image. This similarity cost function assumes that the intensity profiles of the images to be registered are same and therefore, a matching will result from minimization of intensity differences. Such an assumption

is not always valid due to different protocols, different scanning machines, different individuals having different tissue characteristics, etc. Even if these things remain constant, the intensities for images acquired from same individual might be different, for example, due to different air contents in chest scans. Alternatively, mutual information can also be used as the similarity metric. Mutual information does not assume the constant tissue intensities, but it comes with an overhead of computation of histogram and histogram smoothing to allow usage of a robust optimization technique such as gradient descent method.

In this work, we choose the intensity difference as the similarity cost function as has generally been the case for elastic registrations as shown in Eq. 2.29.

$$C_{SIM} = \int_{\Omega_j \cap \Omega_i{}'} |T_i(h_{i,j}(x)) - T_j(x)|^2 dx + \int_{\Omega_i \cap \Omega_j{}'} |T_j(h_{j,i}(x)) - T_i(x)|^2 dx) \quad (2.29)$$

Where, Ω_i and Ω_j represent the ROI's corresponding to the subjects i and j. $h_{i,j}(x) = x + u_{i,j}(x)$ represents the transformation from subject i to subject j in Eulerian frame of reference such that $h_{i,j} : x \in \Omega_j \leftarrow y \in \Omega_i$, $\Omega_i{}' = h_{j,i}(\Omega_i)$ and $\Omega_j{}' = h_{i,j}(Omega_j)$. $T(x)$ represents the intensity at voxel location x. Then, as shown in figure 2.1.6.2, since, $y = T_i(h_{i,j}(x))$ is defined in Ω_i, the inverse image x is defined for $x \in \Omega_i{}'$. Likewise, $T_j(x)$ is defined inside the ROI Ω_j. So, the first term in eq. 2.29 $|T_i(h_{i,j}(x)) - T_j(x)|^2$ is defined over $\Omega_j \cap \Omega_i{}'$. Likewise, the second term under integral $|T_j(h_{j,i}(x)) - T_i(x)|^2$ is defined over $\Omega_i \cap \Omega_j{}'$.

A symmetric similarity cost is chosen so that the value of the cost term remains

same regardless of the direction chosen for the registration.

2.1.6.2 Energy Regularization

While matching real world objects, it makes sense to use a registration model that mimics deformation of the objects in physical world. In general, the minimum total potential energy principle is used for modeling the deformation, e.g., Bookstein's thin plate splines minimize the bending energy of the deformation. In iterative schemes, it is common to use a differential operator that operates on the deformation and is used as an additive cost in the objective function [21, 25, 27, 13, 62, 3, 48, 52]. This work uses such a model and we compute the energy cost term as follows:

$$C_{Reg} = (\int_{\Omega_j \cap \Omega_i{}'} ||\mathcal{L}u_{i,j}(x)||^2 dx + \int_{\Omega_i \cap \Omega_j{}'} ||\mathcal{L}u_{j,i}(x)||^2 dx \tag{2.30}$$

where, $\mathcal{L}$ is a differential operator and operates on the displacement vector $u_{i,j}$. In general, $\mathcal{L}$ can be an arbitrary differential operator, and is chosen as $\mathcal{L} = -\alpha \bigtriangledown^2 - \beta \bigtriangledown (\bigtriangledown) + \gamma$ for small deformation linear elastic model. $\bigtriangledown$ denotes the gradient operator, i.e $\bigtriangledown = \partial/\partial x_1 + \partial/\partial x_2 + \ldots$. In this work, the value of α has been taken as 1.0 and values for β and γ have been taken as 0, i.e., $\mathcal{L} = \bigtriangledown^2$ and denotes a Laplacian operator. $u_{i,j}$ represents the displacement vector that defines the correspondence between image i and image j in the frame of reference of the image j. We use the Euclidean norm to define length of the vector, i.e., $||\hat{u}|| = \sqrt{{u_1}^2 + {u_2}^2 + \ldots}$ for a vector $\hat{u} = \{u_1, u_2, \ldots\}$.

The region over which the cost function is computed needs some attention if

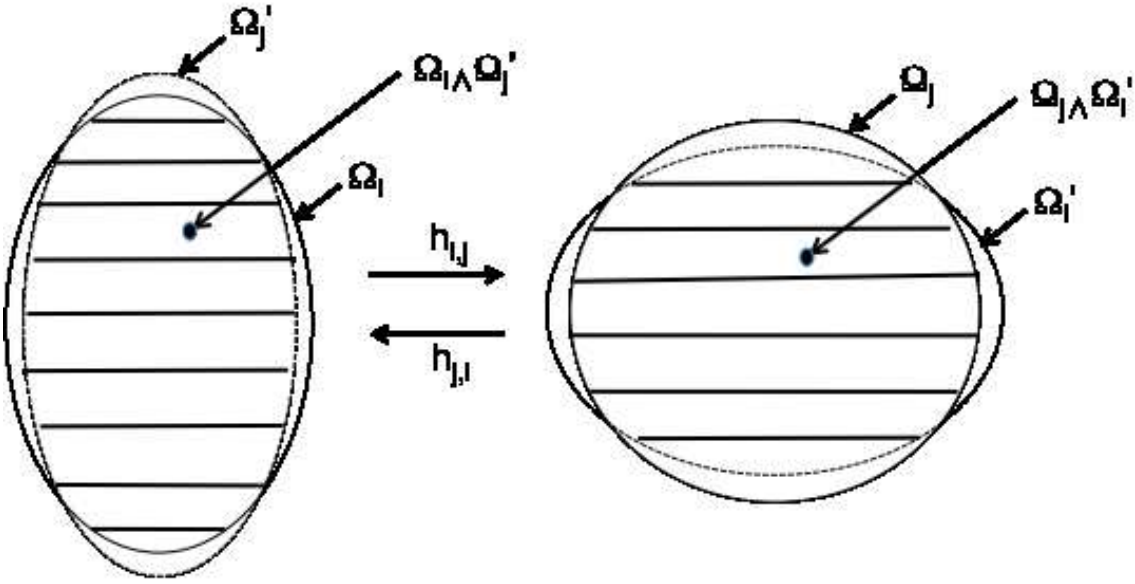

Figure 2.4: Region of Interest for Image Registration. The ROIs in forward and reverse directions are deformed based on boundary conditions and the registration is performed in a window defined by intersection of ROI in one direction and deformed ROI in opposite direction. Ω_i and Ω_j represent the ROIs in template and target images, respectively. The transformation $h_{i,j}$ and $h_{j,i}$ map the ROIs in forward and reverse directions from Ω_i to Ω_i' and from Ω_j to Ω_j', respectively.

the boundary registration does not provide exact correspondence, which is generally the case. In such cases, $u_{i,j}(x)$ is defined for $x \in \Omega_j$ as shown in figure 2.1.6.2. However, the mapping back to Ω_i might cause some region to lie outside Ω_i. Hence, $\Omega_j \cap \Omega_i{}'$ was used as the region of integration for the first integral term such that both, the forward and reverse mapping exist over this region. Likewise, $\Omega_i \cap \Omega_j{}'$ was chosen as the region of integration for the second integral.

2.1.6.3 Inverse Consistency Cost

The inverse consistency cost binds the forward and reverse transformations together and forces them to be close to inverses of each other. The inverse consistency cost function is represented by following equation:

$$C_{ICC} = (\int_{\Omega_j \cap \Omega_i{}'} ||h_{i,j}(x) - h_{j,i}^{-1}(x)||^2 dx + \int_{\Omega_i \cap \Omega_j{}'} ||h_{j,i}(x) - h_{i,j}^{-1}(x)||^2 dx \qquad (2.31)$$

As shown in figure 2.1.6.2, $h_{i,j}(x)$ exists only for $x \in \Omega_j$ and $h_{j,i}^{-1}(x)$ is defined only for $x \in \Omega_i{}'$, so the first integral is computed over $\Omega_j \cap \Omega_i{}'$. Likewise, the second integral is computed over the region $\Omega_i \cap \Omega_j{}'$.

It is to be noted that inverse consistency does not guarantee a better registration on its own. Theoretically, an infinite number of inverse consistent transformations exist between a pair of images. The goal of our optimization is to find a transformation that minimizes the driving objective criterion while being close to the set of all consistent transformations.

Thus, equation 2.28 may be written as:

$$
\begin{aligned}
C = \sigma(& \int_{\Omega_j \cap \Omega_i{}'} |T_i(h_{i,j}(x)) - T_j(x)|^2 dx + \\
& \int_{\Omega_i \cap \Omega_j{}'} |T_j(h_{j,i}(x)) - T_i(x)|^2 dx) \\
+\rho(& \int_{\Omega_j \cap \Omega_i{}'} ||\mathcal{L}u_{i,j}(x)||^2 dx + \int_{\Omega_i \cap \Omega_j{}'} ||\mathcal{L}u_{j,i}(x)||^2 dx) \\
+\chi(& \int_{\Omega_j \cap \Omega_i{}'} ||h_{i,j}(x) - h_{j,i}^{-1}(x)||^2 dx + \\
& \int_{\Omega_i \cap \Omega_j{}'} ||h_{j,i}(x) - h_{i,j}^{-1}(x)||^2 dx)
\end{aligned}
\tag{2.32}
$$

where, $\Omega_i{}'$ represents the domain of object Ω_i deformed into the shape of object Ω_j using the boundary matching function $h_{i,j}(x)$. Note that the integration is performed over the intersection of the two shapes $\Omega_i{}'$ and Ω_j instead of the whole image domain. The first integral represents the total squared difference in intensities of the deformed objects and target objects over entire object domain and therefore represents the similarity cost function. The second integral represents the regularization cost and penalizes the derivatives of the transformation providing a smooth transformation. The last integral represents the inverse consistency cost and binds the forward transformation with the reverse transformation by penalizing their deviation from being inverses of each other.

2.1.6.4 Parameterization Using WEB-Splines

To find a solution minimizing the above equation 2.28, we can use the same parameterization as the section 2.1.4, i.e., for a 3-dimensional case:

$$
\begin{aligned}
u(x_1) &= \sum_{n=0}^{3}\sum_{m=0}^{3}\sum_{l=0}^{3}\mu^1_{i+l,j+m,k+n}B_{i+l,j+m,k+n}(x) \\
u(x_2) &= \sum_{n=0}^{3}\sum_{m=0}^{3}\sum_{l=0}^{3}\mu^2_{i+l,j+m,k+n}B_{i+l,j+m,k+n}(x) \\
u(x_3) &= \sum_{n=0}^{3}\sum_{m=0}^{3}\sum_{l=0}^{3}\mu^3_{i+l,j+m,k+n}B_{i+l,j+m,k+n}(x)
\end{aligned}
\tag{2.33}
$$

where, $B_{i,j}(x)$ is the WEB-spline basis defined in section 2.1.4.3, $u(x) = [u(x_1), u(x_2), u(x_3)]$ and $x = [x_1, x_2, x_3]$. This parameterization allows the boundary conditions to remain unchanged throughout the transformation while matching the intensities inside the object domain.

2.1.6.5 Explicit Derivatives for Gradient Descent Optimization

Using the parameterization described above, we can find a solution to the problem of equation 2.32 by solving for the parameters $\mathcal{C}_{i,j,k}$'s such that the total cost is minimized. This can be done using the gradient descent approach with the update rule:

$$
\mathcal{C}^{(t+1)}_{i,j,k} = \mathcal{C}^{(t)}_{i,j,k} - \eta\frac{\partial C}{\partial \mathcal{C}^{t}_{i,j,k}} \tag{2.34}
$$

for the $(t+1)$-th iteration. Where, η is a weighting factor and may be a constant. From equation 2.28, we have

$$
\frac{\partial C}{\partial \mathcal{C}^{(t)}_{i,j,k}} = \sigma\frac{\partial C_{Sim}}{\partial \mathcal{C}^{(t)}_{i,j,k}} + \rho\frac{\partial C_{Reg}}{\partial \mathcal{C}^{(t)}_{i,j,k}} + \chi\frac{\partial C_{ICC}}{\partial \mathcal{C}^{(t)}_{i,j,k}} \tag{2.35}
$$

The framework defined by equations 2.32, 2.33 and 2.35 leads to the following:

$$\frac{\partial C_{Sim}}{\partial \mathcal{C}_{i,j,k}} = \int_{\Omega} \left(T_r(h_{r,s}(x)) - T_s(x)\right) \frac{\partial T_r(h_{r,s}(x))}{\partial h_{r,s}(x)} \frac{\partial h_{r,s}(x)}{\partial \mathcal{C}_{i,j,k}} dx \tag{2.36}$$

where, the component $(T_r(h_{r,s}(x)) - T_s(x))$ is the difference in intensity of deformed T_r and $T_s(x)$, $\frac{\partial T_r(h_{r,s}(x))}{\partial h_{r,s}(x)}$ represents the derivative of deformed $T_r(h_{r,s}(x))$ w.r.t. the deformed co-ordinate system $h_{r,s}(x)$ at location x. This can be approximated by computing discrete partial derivative in the discrete image at the voxel location x, e.g., for a 2-dimensional case and for the x_1 component of the transformation $T(x)$, we have:

$$\frac{\partial T(y)}{\partial y_1} = \frac{[T(y_1 + [1,0]) - T(y_1 - [1,0])]}{2} \tag{2.37}$$

$$\frac{\partial T(y)}{\partial y_2} = \frac{[T(y_1 + [0,1]) - T(y_1 - [0,1])]}{2} \tag{2.38}$$

where, $y = [y_1, y_2, y_3] = h_{r,s}(x)$ and the component $\frac{\partial h_{r,s}(x)}{\partial \mathcal{C}_{i,j,k}}$ can be computed as follows:

$$\frac{\partial h(x)}{\partial \mathcal{C}_{i,j,k}} = \frac{\partial}{\partial \mathcal{C}_{i,j,k}} \left(x + \sum_{n=0}^{3} \sum_{m=0}^{3} \sum_{l=0}^{3} \mathcal{C}_{i+l,j+m,k+n} B_{i+l,j+m,k+n}(x) \right) = B_{i,j,k}(x) \tag{2.39}$$

The component for the regularization cost can be computed as following for a differential operator $\mathcal{L}(u(x)) = \left[\frac{\partial u(x)}{\partial x_1}, \frac{\partial u(x)}{\partial x_2}, \frac{\partial u(x)}{\partial x_3}\right]$ for a 3-dimensional case:

$$\begin{aligned}\frac{\partial C_{Reg}}{\partial \mathcal{C}_{i,j,k}} &= \int_{\Omega} 2\left(\mathcal{L}u_{i,j,k}(x)\right) \frac{\partial}{\partial \mathcal{C}_{i,j,k}} \left(\frac{\partial}{\partial x_1} u_{i,j,k}(x) + \frac{\partial}{\partial x_2} u_{i,j,k}(x) + \frac{\partial}{\partial x_3} u_{i,j,k}(x)\right) dx \\ &= \int_{\Omega} 2\left(\mathcal{L}u_{i,j,k}(x)\right) \left(\frac{\partial B_{i,j,k}(x)}{\partial x_1} + \frac{\partial B_{i,j,k}(x)}{\partial x_2} + \frac{\partial B_{i,j,k}(x)}{\partial x_3}\right) dx\end{aligned} \tag{2.40}$$

Here, the term $\mathcal{L}u_{i,j}(x)$ can be computed using discrete derivatives and $\frac{\partial B_{i,j}(x)}{\partial x}$ can be pre-computed and used for computation of the cost function.

The component for the inverse consistency cost adds the following cost for the gradient estimation for each direction:

$$\frac{\partial C_{ICC}}{\partial \mathcal{C}_{r,s_{i,j,k}}} = \int_{\Omega} \left(h_{r,s}(x) - h_{r,s}^{-1}(x)\right) B_{i,j,k}(x) dx \tag{2.41}$$

The effect of each component of cost can be varied by variation in the weighting factors for each term, i.e., σ, ρ and χ. In general, one factor can be kept as 1 and other two weighting factors can be varied to adjust the relative importance of the different cost functions.

2.1.6.6 Algorithm

Algorithm 2.1 shows shows the various steps taken for matching intensities only inside the region of interest, i.e., boundary constrained image registration based on the above.

Compute Boundaries of Objects $\partial\Omega_1$ and $\partial\Omega_2$ in the two images using morphological operations
Compute inverse-consistent point wise correspondence at the object boundaries using transitive consistent manifold registration [13]. Set displacements at boundaries as boundary conditions, $u_{\partial\Omega_1}$ and $u_{\partial\Omega_2}$
Based on chosen knot spacing, divide the image into regular grids and set b-spline coefficients on all knots $c_i = 0$. Also compute WEB-splines based on the object boundaries and set coefficients $\mu_i = 0$
Using a least square technique, compute the b-spline coefficients c_i's that approximate the boundary conditions and defines a function $u_\partial(x) = \sum c_i \beta_i(x)$
Construct the Galerkin matrix using Eq. 2.23 and solve for WEB-spline coefficients μ_i's. Define $u^*(x) = \sum \mu_i B_i(x)$.
repeat
  Compute $\Delta {\mu_i}^t = -\frac{\partial \mathcal{C}}{\partial \mu_i}|_t$ for each WEB-spline coefficient.
  ${\mu_i}^{t+1} = {\mu_i}^t + \epsilon \Delta {\mu_i}^t$.
  $u^*(x) = \sum {\mu_i}^t B_i(x)$.
until convergence.
$h(x) = x + u^*(x) + u_\partial(x)$.

Algorithm 2.1: Algorithm for parameter estimation for boundary constrained image registration

2.2 Analysis, Comparison and Validation of BICIR Registration Algorithm

The methods for comparison with intensity based inverse-consistent linear elastic method will be presented in this section. The next section 2.2.1 provides an overview of the various metrics used for validating and comparing registration algorithms. Section 2.2.2 outlines the method used for characterizing the BICIR technique based on various weights and parameters used in the cost functions and construction of the basis elements. Section 2.2.3 provides the methods used for validation of BICIR method. Section 2.2.4 provides the details of comparison of BICIR algorithm with the small-deformation inverse consistent linear elastic (SICLE) image registration method. SICLE uses intensity information like BICIR, but does not have

boundary constraints.

2.2.1 Validation Metrics

Following list explains various metrics used for checking the quality of registration results.

1. **Landmark Error**

   The landmark error is a point based metric, in which a number of points of correspondence, called landmark points are identified from the two images to be registered together. Although it is not trivial to identify corresponding points in two 3-dimensional image volumes, automaticand manual landmark identification is possible for human lung as the object of interest. Once the points of correspondences are known, then landmark mismatch error after the registration is computed. Let $S_1(x)$ and $S_2(y)$ represent the two images registered together through the transformations $h_{12} : S_1 \rightarrow S_2$ and $h_{21} : S_2 \rightarrow S_1$ and $x_i, i = 1, 2, \ldots, n$ and $y_i, i = 1, 2, \ldots, n$ be n corresponding points in the images S_1 and S_2 respectively. The transformation h_{12} maps each point from the set $\{x_i\}, i = 1, \ldots, n$ into set of points $\{y'_i\}, i = 1, \ldots, n$ where, $y'_i = h_{12}(x_i)$. Likewise, the transformation h_{21} maps each point from the set $\{y_i\}, i = 1, \ldots, n$ into set of points $x'_i, i = 1, \ldots, n$, where $x'_i = h_{21}(y_i)$. Then, average landmark matching error ϵ_{lmk} in either direction is computed as:

$$\begin{aligned} \epsilon_{lmk12} &= \frac{1}{n} \sum_{i=1}^{n} |y_i - y'_i| \\ \epsilon_{lmk21} &= \frac{1}{n} \sum_{i=1}^{n} |x_i - x'_i| \end{aligned} \tag{2.42}$$

2. **Relative Overlap**

Relative overlap is another popular metric used for validation of a registration algorithm. For two sets A and B, the relative overlap is defined as

$$RO = \frac{A \cap B}{A \cup B} \tag{2.43}$$

Relative overlap is a measure for the accuracy of registration in matching overall volume of corresponding objects. For objects $A \in S_1$ and $B \in S_2$ representing the objects of interest in the images S_1 and S_2 respectively, the relative overlap is unity if and only if they fully overlap. It is desirable to get a value close to unity.

3. **Similarity Cost**

Similarity cost is the driving function for the BICIR algorithm and will be minimized as part of the objective function. It is an important metric when comparing two different methods that minimize the same objective function. The BICIR method is intensity based method with the objective of minimizing the intensity differences between two images. For the two images S_1 and S_2 with the transformations h_{12} and h_{21} that deform S_1 into S_2 and S_2 into S_1 respectively, let $S_i(x)$ represent the intensity of image S_i at co-ordinate location x. The similarity cost is then defined as

$$C_{simi,j} = \int_{\Omega_i{}' \cap \Omega_j} |S_j(x) - S_i(h_{i,j}(x))|^2 dx \tag{2.44}$$

where, the intersection of $\Omega_i' = h_{j,i}(\Omega_i)$ and Ω_j represents the region of interest, over which the registration is performed.

The above mentioned three metrics are used in validation of the BICIR algorithm as well as for comparison with existing technique (SICLE).

2.2.2 Characterization of BICIR w.r.t Algorithm Parameters

In the BICIR framework, the registration is posed as an optimization problem that minimizes a scalar cost term. The similarity cost i.e., intensity difference between the two images is used as the driving function for computing the correspondence. The constraints of energy regularization and inverse consistency are included as additional costs. The overall objective function of the BICIR algorithm consists of linear sums of these three costs. The scalar objective function C is described by Eq. 2.32 in section 2.1, and is minimized w.r.t. the transformations $h_{i,j}$ and $h_{j,i}$ defining the correspondences between images T_i and T_j.

The method of using a weighted sum objective function is one of the simplest and most popular method for optimization of multi-objective functions. When all the weights are positive, the cost function is always convex, which is a sufficient condition for minimizer of cost described in 2.32 to be Pareto optimal [51]. Pareto optimality implies that no improvement from the Pareto optimal can be achieved that minimizes one cost term without affecting the other costs [35], [40]. However, sufficiency of weighted sum objective function to have Pareto optimal for all values of weights implies that instead of one solution, we have a large set of Pareto optimals. This set is called Pareto set and minimizers for all positive values of various weights

always lie in this set. Hence, the choice of weights remains a problem as there is no standard way of choosing weights. The choice of weight is largely determined by the preference of the decision maker and although there are some proposed methods such as Saaty's eigenvalue method [51], all these techniques require the decision-maker to rank the various cost functions in order of importance. In other words, setting of weights depends upon the preferences of the decision-maker and is generally performed heuristically.

In view of the above, the strategy of Johnson [21] for choosing weights for a similar cost function is followed here and is briefly described as follows:

1. Similarity Cost Parameter σ is always chosen as 1.0. This does not have any effect on the registration, since relative weight of other cost terms can still be changed using other parameters.

2. Inverse Consistency Cost Parameter χ and Linear Elasticity Cost Parameter ρ are varied over a range of values, respectively by keeping one parameter constant for all range of values for the other parameter and repeating this for next constant value of the first parameter. The BICIR registrations are performed using these set of values one at a time, and the total cost is calculated. Parameters corresponding to the minimum total cost are chosen as the recommended parameters for that type of image data.

3. The step size and number of iterations are similarly chosen for the recommended parameter values by changing step size and observing the number of iterations

required to get convergence within a specified range.

2.2.3 Analysis of BICIR Registration Method

The BICIR method was analyzed over a range of 2D and 3D images and impact of change in various parameters was studied. The images ranged from parametric shapes to shapes of anatomical objects. The 2D phantom objects included ellipses containing smaller ellipses such that there are intensity differences at the boundaries as well as in the interior of the object. The 3D objects included parametric shapes of hollow ellipsoids with different thicknesses and shapes, and brain images.

The correspondence between shapes was computed analytically. For The boundary correspondences for the phantom images were computed analytically using parameters for the outer shape description. Let X and Y represent the set of all pixels lying on the boundaries of ellipses E_X and E_Y. The ellipses were constructed such that their major and minor axis lay along the X- or Y-directions. Let d_{1j} and d_{2j} represent the diameters of ellipse j, $j \in X, Y$ in X- and Y-direction, and c_{1j} and c_{2j} represent the centers of the ellipses using same terminology. Let (x_{1i}, x_{2i}) represent $i-th$ element of set X with corresponding element $({x_{1i}}', {x_{2i}}')$ and (y_{1j}, y_{2j}) represent $j-th$ element of set Y with corresponding element $({y_{1j}}', {y_{2j}}')$ the sets X, X' and Y, Y' represent the forward and reverse boundary conditions where X' and Y' can be computed using equations 2.45 and 2.46.

$$\begin{aligned} {x_{1i}}' &= \frac{d_{1y}}{d_{1x}}(x_{1i} - c_{1x}) + c_{1y} \\ {x_{2i}}' &= \frac{d_{2y}}{d_{2x}}(x_{2i} - c_{2x}) + c_{2y} \end{aligned} \tag{2.45}$$

$$
\begin{aligned}
{y_{1_j}}' &= \frac{d_{1_x}}{d_{1_y}}(y_{1_i} - c_{1_y}) + c_{1_x} \\
{y_{2_j}}' &= \frac{d_{2_x}}{d_{2_y}}(y_{2_i} - c_{2_y}) + c_{2_x}
\end{aligned}
\tag{2.46}
$$

Likewise, the boundary correspondence for 3D ellipsoids was analytically computed with the difference being that there are three diameters and center point has 3D coordinate location. In this case, (x_{1i}, x_{2i}, x_{3i}) represents $i-th$ element of set X with corresponding element $({x_{1_i}}', {x_{2_i}}', {x_{3_i}}')$ and $(y_{1_j}, y_{2_j}, y_{3_j})$ represent $j-th$ element of set Y with corresponding element $({y_{1_j}}', {y_{2_j}}', {y_{3_j}}')$ and the sets X, X' and Y, Y' represent the forward and reverse boundary conditions where X' and Y' can be computed using equations 2.47 and 2.48.

$$
\begin{aligned}
{x_{1_i}}' &= \frac{d_{1_y}}{d_{1_x}}(x_{1_i} - c_{1_x}) + c_{1_y} \\
{x_{2_i}}' &= \frac{d_{2_y}}{d_{2_x}}(x_{2_i} - c_{2_x}) + c_{2_y} \\
{x_{3_i}}' &= \frac{d_{3_y}}{d_{3_x}}(x_{3_i} - c_{3_x}) + c_{3_y}
\end{aligned}
\tag{2.47}
$$

$$
\begin{aligned}
{y_{1_j}}' &= \frac{d_{1_x}}{d_{1_y}}(y_{1_i} - c_{1_y}) + c_{1_x} \\
{y_{2_j}}' &= \frac{d_{2_x}}{d_{2_y}}(y_{2_i} - c_{2_y}) + c_{2_x} \\
{y_{3_j}}' &= \frac{d_{3_x}}{d_{3_y}}(y_{3_i} - c_{3_y}) + c_{3_x}
\end{aligned}
\tag{2.48}
$$

For brain images, three different approaches were used. In first approach, binary masks were obtained by dilating the brain segmentations by 5 voxels. This was done such that the ROI obtained after intersection of Ω_i and ${\Omega_j}'$ still contained the entire brain. The binary masks thus obtained were registered using SICLE registration method. The registration results were applied only to boundary voxels to get

the input boundary conditions for BICIR. Let $h_{0i,j}$ denote the transformation from ROI Ω_i to Ω_j and let $h_{0j,i}$ represent the transformation in the opposite direction. Let X represent the boundary voxels for the template image and let Y represent the boundary voxels for the target image such that the transformation $h_{0j,i}$ maps each point $x \in X$ to a point x'. Let X' be a collection of all such transformed points in forward direction and Y' represent a collection of all such transformed boundary points in reverse direction. This results in a collection of points X, X' and Y, Y' that describe initial boundary condition.

In second approach, a region of interest inside brain images was chosen. This ROI represented an expert-segmented anatomical region. BICIR method was updated to automatically compute a spherical envelope that enclosed the entire ROI in both, template and target images. The region inside this envelope was used to register the images together. The registrations were performed over 16 NIREP datasets using one image as a template. The results were compared against results from SICLE for the same ROI.

In third approach, ellipsoid envelope was computed for the same ROI and the process repeated for validation and comparison.

2.2.4 Comparison with Small Deformation Inverse Consistent Elastic Registration

BICIR follows similar constraints for its intensity phase and includes the additional step of boundary matching, which is necessary to provide the boundary constraints. The performance of BICIR method was evaluated using 2D phantom images and 2D images from sheep lungs. The phantom images contained simple shapes to

illustrate the various steps of BICIR. On the other hand, the sheep lung images were complex and were used to evaluate how well the new algorithm could register real data. The comparison with Small Deformation Inverse Consistent Elastic Registration (SICLE) was made over a total of 20 2D registrations of CT images of sheep lungs. The 2D slices were extracted from 3D CT images of sheep lungs at different phases of the breathing cycle across different subjects. The 2-D template image was extracted from a 3-D CT image collected from sheep. The images were selected to have as many correspnding features as possible. Note that some of the regions in these images do not have corresponding regions in the other image due to motion in and out of the image plane. This problem does not exist for 3-D registration. For the comparison of registrations in 2-D, it was assumed that the motion in and out of the plane was minimal.

In the SICLE method, the template and the target images were registered together using intensity differences while minimizing the inverse consistency and linear elastic energy regularization constraint. In BICIR method, the lung boundaries were extracted and matched using inverse consistent boundary matching. The registration was initialized using the boundary conditions through Element Free Galerkin Method (EFGM). The EFGM solution was then made consistent through inverse consistency minimization before initializing the intensity phase. The consistent EFGM solution was then used to initialize the intensity based registration, during which only region inside the ROI gets registered.

2.2.4.1 Preprocessing

The same preprocessing steps were applied to the input images for both the methods. The sheep lung was extracted from the 3-D sheep chest CT images using intensity threshold based segmentation followed by manual edit. After the segmentation, the corresponding 2-D slices were identified between different scans and a collection of 2-D slices was generated. This collection of 2-D slices was then used for the registrations comparison. In addition, the image intensities were normalized from $[-1000, 0]$ to $[0, 255]$ such that entire range of intensities of the sheep lungs is captured and stored in 8-bit data format.

The two algorithms were run and tested for a sample size of 20 2-D lung images extracted from the 3-D sheep lung images.

The following comparisons were made:

1. Average Landmark Correspondence Error
2. Maximum Landmark Correspondence Error
3. Relative Overlap
4. Average Intensity Difference (Similarity Cost)
5. Average Inverse Consistency Error
6. Maximum Inverse Consistency Error
7. Total Time Taken

CHAPTER 3
RESULTS

This chapter presents the results for characterization, analysis and validation of Boundary-Constrained Inverse Consistent Image Registration (BICIR) method and its comparison against the Small-deformation Inverse Consistent Linear Elastic (SICLE) Image Registration.

Section 3.1 provides the results for analysis and evaluation of the BICIR method using 2D images. The section demonstrates various stages of the BICIR registration method and effect of parameters such as knot spacings and relative weights of different cost functions. The section also provides results for comparison of BICIR method against SICLE method using a number of 2D sheep lung images. The 2D images corresponded to 2D slices from CT sheep lung images such that the slices being registered contained similar anatomical regions.

Section 3.2 presents registration results for 3D phantom images and comparison with Small-deformation Inverse Consistent Linear Elastic (SICLE) registration method using 3D brain MRI datasets. The 3D image registrations were performed on segmentations defined on MRI brain images from NIREP database using parametric as well as non-parametric region of interest. Results show that the BICIR method was significantly better than SICLE method.

3.1 Registration of 2D images using BICIR

This section provides results for 2D image registration using BICIR method. The section is divided as follows: Section 3.1.1 presents analysis of registration between pairs of simple 2D phantom images. Section 3.1.2 presents the comparison between SICLE and BICIR over a small population of 2D sheep lung images. Simple phantom shapes were considered first since the boundary correspondences can be computed analytically and the ground truths are easier to determine while the shapes can be altered to create different kind of tests for the registration method. For example, in ellipsoidal phantom shapes used in this section, all points at boundaries have corresponding unique displacement vectors to the point they map to in the target elliptical object. The interiors of these phantoms were designed such that there are intensity differences before the registration and the intensity differences remain even after boundary matching. As a result, even affine registration that matches boundaries in general, will not match the interiors for the examples used. After establishing results for 2D phantom images, the method was put to test using 2D medical images representing slices from CT scan on sheep lungs. The slices had to be carefully extracted so that they pertain to roughly the same anatomical plane and contained similar internal structures. BICIR method was compared to SICLE method, which is also a consistent registration method and the results are presented in section 3.1.2.

3.1.1 Registration of 2D Phantom Images

This section analyzes the performance of the BICIR algorithm using 2D phantom images. The phantom image data set consisted of simple shapes to illustrate the various steps of the BICIR. The collection of 2D phantom images consisted of an outer elliptical shape containing an interior elliptical shape as shown in Figure 3.1. The intensities of the outer ellipse shape were kept at 255 and the intensity of the inner ellipse were chosen to be 128, with the background having an intensity value of 0. A sample size of eight datasets was generated using different sizes of the two ellipses. The two elliptical objects combined together represent the object shape and the boundaries of the outer ellipse were treated as the object boundaries. This construction, although simple, allows for two different type of feature sets: the outer boundaries correspondence representing the boundary conditions for the EFGM based boundary matching and the interior ellipse, which represents the intensity differences between the two images.

Figures 3.2 and 3.3 show results for one sample 2-D phantom image registration. In Figure 3.2, the top row represents the results for the forward direction and the bottom row represents the results for the reverse direction. The first and second images in the top row represent the template and the target images to be registered. It may be noted that the role of template and target images gets switched during the registration in the reverse direction. The third image represents the deformed template following only EFGM based interpolation of the boundary conditions and the fourth image shows the deformed template after EFGM based interpolation fol-

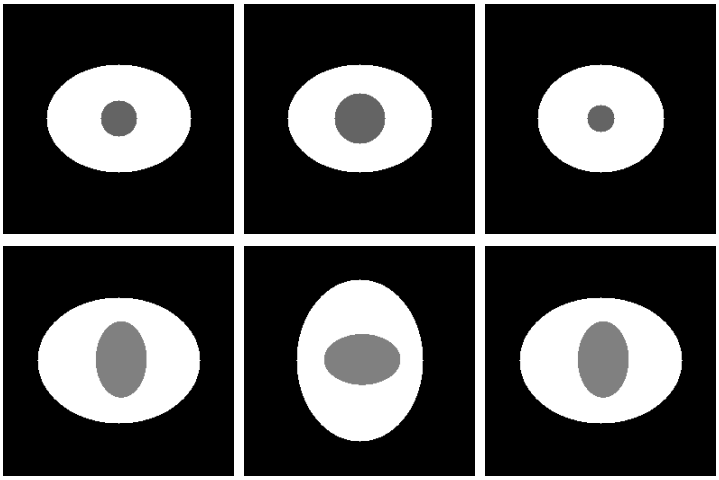

Figure 3.1: 2D Ellipsoid Phantom Image Dataset. The figure shows the 2D ellipsoid images registered for characterizing performance of BICIR. The phantoms consisted of background value of 0 and an outer ellipsoid image with intensity value of 255. The ellipsoidal foreground object contained an internal ellipsoidal object with intensity values of 128.

lowed by the boundary constrained intensity registration. The fifth, sixth and seventh images show the intensity difference between the deformed template and the target before the registration, after EFGM based interpolation and after EFGM based interpolation followed by the boundary constrained intensity registration, respectively. The second row shows the similar images for the reverse direction. The figure shows that initially, there are large differences between the boundaries as well as the interiors of the two objects being registered together. The boundary condition interpolation using EFGM matches the boundaries exactly, but differences still remain in the interior of the objects. These differences are minimized during the intensity phase and finally, the images are matched together, both at the boundaries as well as in the interior of the object. The same can be seen in the bottom row for the registration

in the reverse direction.

Figure 3.3 shows deformed grid and the displacement fields at various stages of the registration for the purpose of illustration of behavior of the registration method. The figure contains three rows, corresponding to the boundary extension function, which represents an arbitrary extension of boundary correspondences to the interior of the object, the results after the interpolation of these boundary conditions using EFGM and the results of boundary constrained intensity registration after boundary conditions are interpolated using EFGM. The first three columns represent the results in forward direction and the last three columns represent the results in reverse direction, where the forward and reverse directions are same as in Figure 3.2.

The figure shows the deformed grid and x- and y- displacements at each of these three stages for both directions. The results are presented in Eulerian frame of reference. It can be seen from the deformed grid that the deformation is limited only to the domain of the object and also that the boundary extension function, although smooth, has very limited and localized deformation. The images corresponding to x- and y- displacements provide the same information. The second row of the images show the results after the boundary displacements are interpolated over entire object domain using the Element Free Galerkin Method. The deformed grid and x- and y- displacements are much smoother and less localized than the first row, as the deformation is evenly distributed according to the governing partial differential equation. Finally. the third row shows the displacements after intensity based registration. The figure shows that the boundaries of the object remain unchanged, but the differences

in intensity cause the deformation inside the object. The same observations can be made in the images representing the registration in the reverse direction.

Figures 3.2 and 3.3 provide simplistic but strong illustration of the BICIR registration method. Table 3.1 shows the performance metrics for the 2-D phantom registrations.

		Ave. Int. Diff.	Ave. ICE	Max. ICE	Total Relative Overlap (%)
Initial	Average	59.81	-	-	81.96
	Std. Dev.	23.19	-	-	6.35
Registration w/o	Average	2.86	0.381	2.025	99.994
Inv. Consistency	Std. Dev.	3.505	0.1706	1.123	0.0149
Registration with	Average	3.08	0.063	0.512	99.994
Inv. Cons.	Std. Dev.	3.054	0.0165	0.0995	0.0149

Table 3.1: Summary Performance Statistics for Eight 2D Phantom Experiments.

The table shows various performance parameters for evaluation of the BICIR registration method over a total of 8 2D phantom images. The first row in table show the value of intensity differences and relative overlap before the registration. The second and third row represent the values of different metrics for different constraints of no inverse consistency and with inverse consistency, respectively. The results show that the intensity differences were minimized while also minimizing the inverse consistency cost from an average of 0.381 to 0.063. The total relative overlap was almost 100% since the boundaries were matched explicitly and remained unchanged during the intensity registration.

3.1.2 Registration of 2D Sheep Lung Images

This section provides comparison of the BICIR method with SICLE image registration [4] method. SICLE registration method was chosen since BICIR follows constraints similar to SICLE with the added constraint of boundary matching. SICLE method registers entire images with entire images regardless of object boundaries, but uses similar regularization constraints as the BICIR method follows in intensity phase. BICIR includes additional step of boundary matching, which is necessary to provide the boundary constrained image registration. The comparison was done over a total of 20 2-D registrations of CT images of sheep lungs at different phases of breathing cycle across different subjects. The 2-D images were extracted from 3D CT images collected from sheep. The image pairs to be registered were selected such that they include as many corresponding features as possible. It may be noted that some of the regions in these images do not have corresponding regions in the other images due to motions in and out of the image plane. This problem does not exist for 3D registration. For the current study, it is assumed that the motion in and out of the plane is minimal and the images correspond in 2-D.

In the SICLE method, the template and the target images were registered together using intensity differences while minimizing the inverse consistency under linear energy regularization constraint. In BICIR method, the lung boundaries were extracted and matched using inverse consistent boundary matching. The registration was initialized using the boundary conditions through EFGM. The EFGM solution was then made consistent through inverse consistency minimization before initializing

the intensity phase. The consistent EFGM solution was then used to initialize the intensity based registration, during which, only region inside the ROI gets registered.

Figure 3.4 shows the registration results for a pair of 2-D sheep lung images for the BICIR registration method. The first two panels show the images of the two objects to be registered together. The boundaries of the ROIs for the two objects have been overlaid on the object. The arrows in the first two panels show the corresponding points given as input to the inverse-consistent boundary matching program to help it avoid the local minima. The correspondence defined by these points is kept fixed and correspondences along the boundaries are updated while minimizing the total boundary registration cost. The boundary correspondence was used as input to BICIR and the deformed images in both directions are shown in third and fourth panels, respectively.

Figure 3.4 also shows that the BICIR method matches boundaries exactly and minimizes the intensity differences interior to the ROIs. This can also be seen in Figure 3.5, which shows the absolute intensity differences between the deformed Image 1 and Image 2 before registration and after SICLE, after only boundary matching using EFGM and after BICIR.

The difference images in Figure 3.5 display the absolute value of difference between the gray scale values of the two images computed at each pixel of the image. The first panel shows the absolute intensity differences between the two images before the registration. The second panel shows the difference image between the deformed image 1 and image 2 after SICLE registration. The difference image shows that while

the SICLE method matches the airways denoted by small arrows, it performs poorly in matching outer boundaries of the lung as shown by the large arrows. The third and fourth panels show the absolute intensity differences between the deformed image 1 and image 2 after boundary matching using EFGM and after BICIR, respectively. The large arrows show that after EFGM, there is no matching error at the boundaries and the boundary matching remains unchanged during the intensity phase. The small arrows show that while there are mismatches at the airways after EFGM, the differences are minimized after the intensity phase. Comparing the SICLE and BICIR results, it can be seen that both do a good job of matching the main airways, however, the BICIR algorithm clearly outperforms the SICLE algorithm while matching the outer boundary of the lung.

Figure 3.6 shows the registration results for the SICLE method and for the BICIR method after various processing stages. The first row represents the results for SICLE method. The other rows represent results from BICIR method: the second row shows the results after the EFGM phase, the third row shows the inverse error minimization of EFGM solution and the last row shows the result after fine-tuning of the consistent EFGM solution using the intensity information inside the ROI. The first column shows the deformed grids using the deformation fields obtained from registration method corresponding to that row. The second column represents the inverse consistency cost. The third- and fourth- columns represent the x- and y-displacement vectors shown as the intensity images. The last column shows the log-Jacobian image of the transformation, which represents relative local contraction

and expansion of the template object, when deformed into the frame of reference of the target image.

The first row in Fig. 3.6 shows that for the SICLE registration method, the deformation is taking place over entire image and is not restricted to the ROI as a results of regularization across the objects. The second row shows the results after EFGM phase, during which the boundary correspondences are interpolated over the region of interest using an energy regularization constraints. The smooth transition in displacement and a very smooth Jacobian image shows that the transformation inside the ROI is a results of only boundary matching during this phase, as there is no local deformation taking place in the ROI. The second panel in second row shows the inverse consistency error image, which has an average of 0.27 over the region of interest. The third panel shows that after inverse consistency minimization, the inverse consistency error reduces to almost zero everywhere inside the ROI except near the boundaries. This results from WEB-splines vanishing at the boundaries, leaving the inverse consistency error at the boundaries remains unchanged. The last row shows the results after the intensity phase, where local intensity information is used to update the transformation and the local transformation can be seen in the deformed grid, log-Jacobian and the displacement images. The inverse consistency error increases slightly inside the ROI as a result of local deformation, but the average value over the ROI is still very low (0.08 pixels). As shown later in this section, BI-CIR provides overall improvement in relative overlap along with decrease in intensity differences and lower inverse consistency error.

The SICLE and BICIR methods were compared using the following metrics:

- *R*elative Overlap: For two sets A and B, the relative overlap is defined as the ratio of their intersection to their union, i.e.

$$R.O. = \frac{A \bigcap B}{A \bigcup B} \tag{3.1}$$

For comparison, we compared the R.O. for the registered regions of interest.

- *S*imilarity Cost: For the two images T_i and T_j to be registered, the absolute intensity difference between the two images is computed at each pixel. The average value of the differences was computed over the entire image, since a common region of interest could not be established in the space of deformed template when comparing the two different methods.

- *I*nverse Consistency Error: The inverse consistency error at each pixel is defined as the difference between the transformation in one direction and inverse of transformation in the opposite direction. Let $h_{i,j}$ and $h_{j,i}$ represent the transformation from image i to image j and transformation from image j to image i, respectively. Then, the inverse consistency error is computed at each pixel location x as $|h_{i,j}(x) - h_{j,i}^{-1}(x)|$ and $|h_{j,i}(x) - h_{i,j}^{-1}(x)|$ in forward and reverse direction, respectively. A perfectly inverse consistent image registration will have zero inverse consistency error and therefore contains no correspondence ambiguity. Although it should be noted that inverse consistency error can be very low for even very poor correspondences.

- *A*verage Boundary Error: The average boundary error is defined as the average distance between the boundaries of the deformed template object and the target object and vice versa in reverse direction, respectively. For each boundary pixel in the deformed image, the distance with closest target boundary pixel is computed as the boundary matching error.

Table 3.2 shows the metrics for the two registration methods for the 20 2D sheep lung registrations. The table shows that the average intensity differences were minimized from an initial average value of 15.4 to an average value of 8.52 by SICLE registration and to an average value of 7.99 by the BICIR method. SICLE reduced the average boundary error from 6.63 before registration to an average of 2.08 pixels, while BICIR method matched the boundaries exactly. Likewise, the average relative overlap for SICLE method is 89.9%, which is much lower than the BICIR method (100%). Maximum inverse consistency error was consistently higher in BICIR method owing to initial inverse consistency error at boundaries of the object and the inability of method to update the boundary conditions. However, the average inverse consistency error over the region of interest was lower for BICIR, when compared with SICLE.

The results in Table 3.2 show that BICIR method provided better registration of the 2D sheep lung images than SICLE by explicitly matching boundaries and performing intensity based registration over only region of interest. While the BICIR method provides perfect boundary matching and a 100% relative overlap, the improvement can be seen in other performance metrics such as the intensity differences and the inverse consistency error.

This section discussed the application of BICIR registration method for 2D phantom shapes where a consistent analytical boundary correspondence could be computed. The BICIR method was shown to retain boundary correspondence while matching the interior regions well and keeping the inverse consistency error to a very small value. The method was extended to anatomical images where 2D sheep lung images were registered using BICIR and SICLE and comparison was made. BICIR registration method was shown to provide much better results compared to SICLE method. The validation of 2D sheep lung images is limited by the fact that the 2D slices had to be assumed to correspond to same anatomical region without any out of plane deformation. In general, this assumption does not hold true and 3D registration is required to register 3D images together.

Section 3.2 extends the results for 3D images by analyzing the registration for 3D phantom images and MRI brain scans.

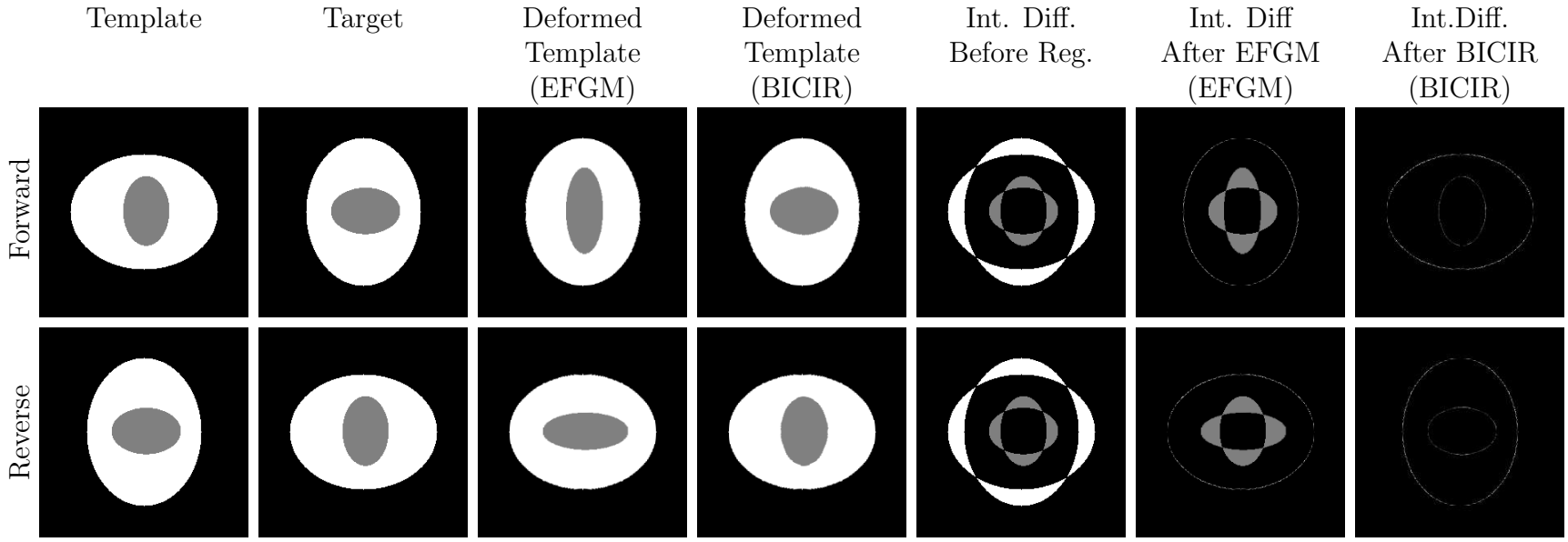

Figure 3.2: Top row (From Left to Right): Template, Target, Deformed Template After Boundary Matching using EFGM, Deformed Template after BICIR, Absolute Intensity Difference image before registration, Absolute Intensity Difference image after EFGM and Absolute Intensity Difference image after BICIR registration, respectively. Bottom row shows the same results for the reverse direction.

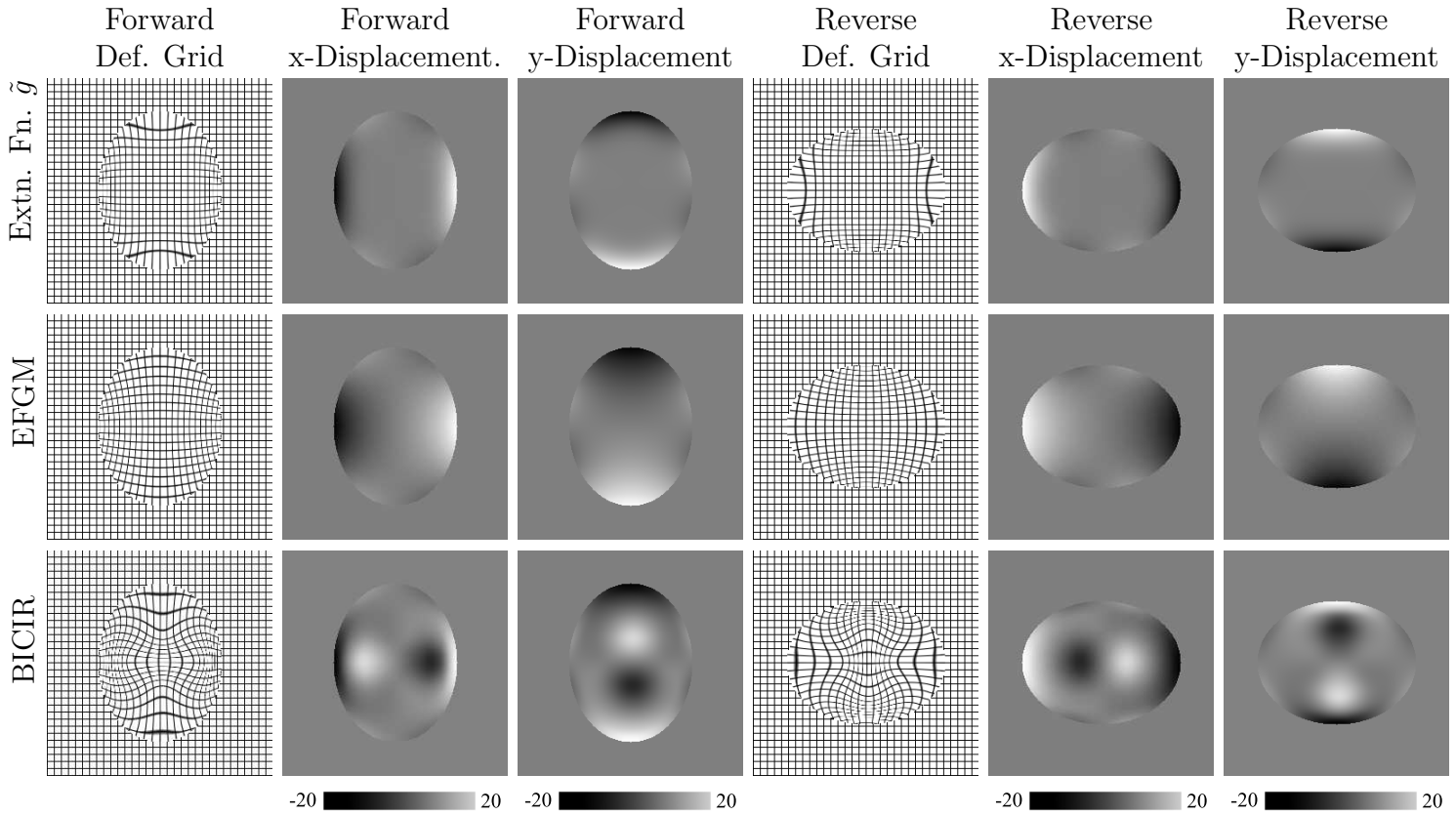

Figure 3.3: Top row (From Left to Right): Deformed grid in forward direction, x-component of transformation in forward direction, y-component of transformation in forward direction, Deformed grid in reverse direction, x-component of transformation in reverse direction and y-component of transformation in reverse direction, respectively. The top row corresponds to only the boundary extension function $\tilde{g}$, the middle row corresponds to the results obtained using boundary matching through EFGM using WEB splines, and the bottom row corresponds to results obtained after BICIR registration, where WEB spline based intensity registration algorithm is initialized using results from EFGM, respectively. It may be noted that the forward and reverse registrations are performed simultaneously, while minimizing inverse consistency in every iteration.

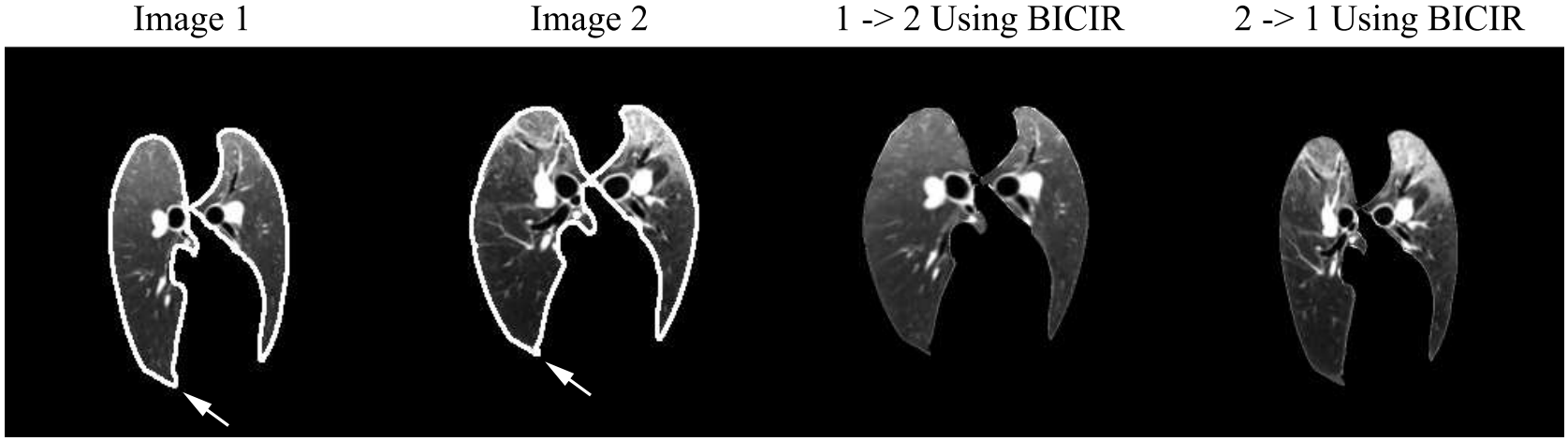

Figure 3.4: The first two panels show the two images that were registered. The contours used for boundary matching are shown superimposed on these images. The arrows show corresponding landmarks in the images that were forced to align during the boundary matching step. The last two panels show the registration results obtained using the BICIR algorithm. The third panel shows Image 1 deformed into the shape of Image 2 and the fourth panel shows Image 2 deformed into the shape of Image 1.

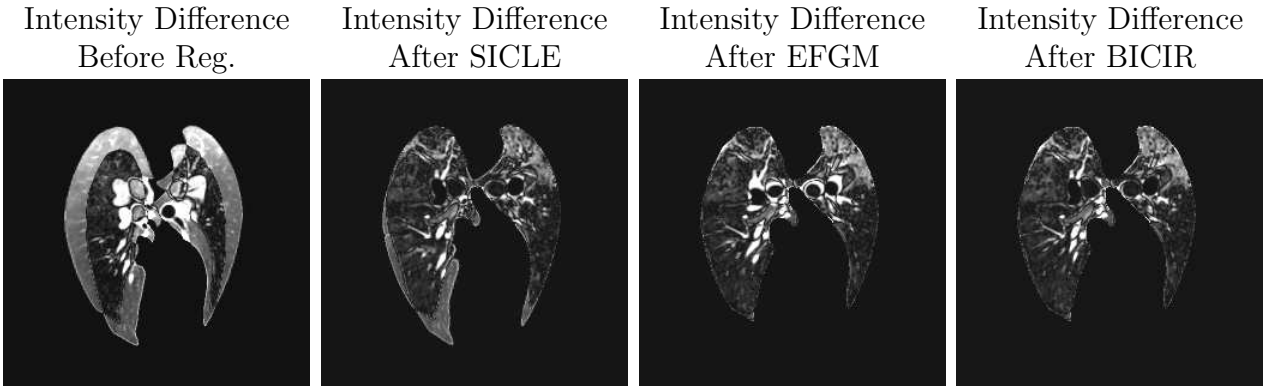

Figure 3.5: From left to right: Initial pixel-wise absolute difference between intensities of Image 1 and 2, absolute intensity difference between Image 1 and target images after SICLE, inverse consistent EFGM and BICIR. The results correspond to the forward direction of figure 3.4. The SICLE and BICIR methods did a similar job in matching the 4 large airways shown by the 4 small arrows in each panel. However, the SICLE algorithm did a poor job of matching the outer boundary of the lung as shown by the 2 large arrows in each panel. Note that the EFGM method matched the boundaries well, but not the airways which are matched well during the intensity matching phase of BICIR.

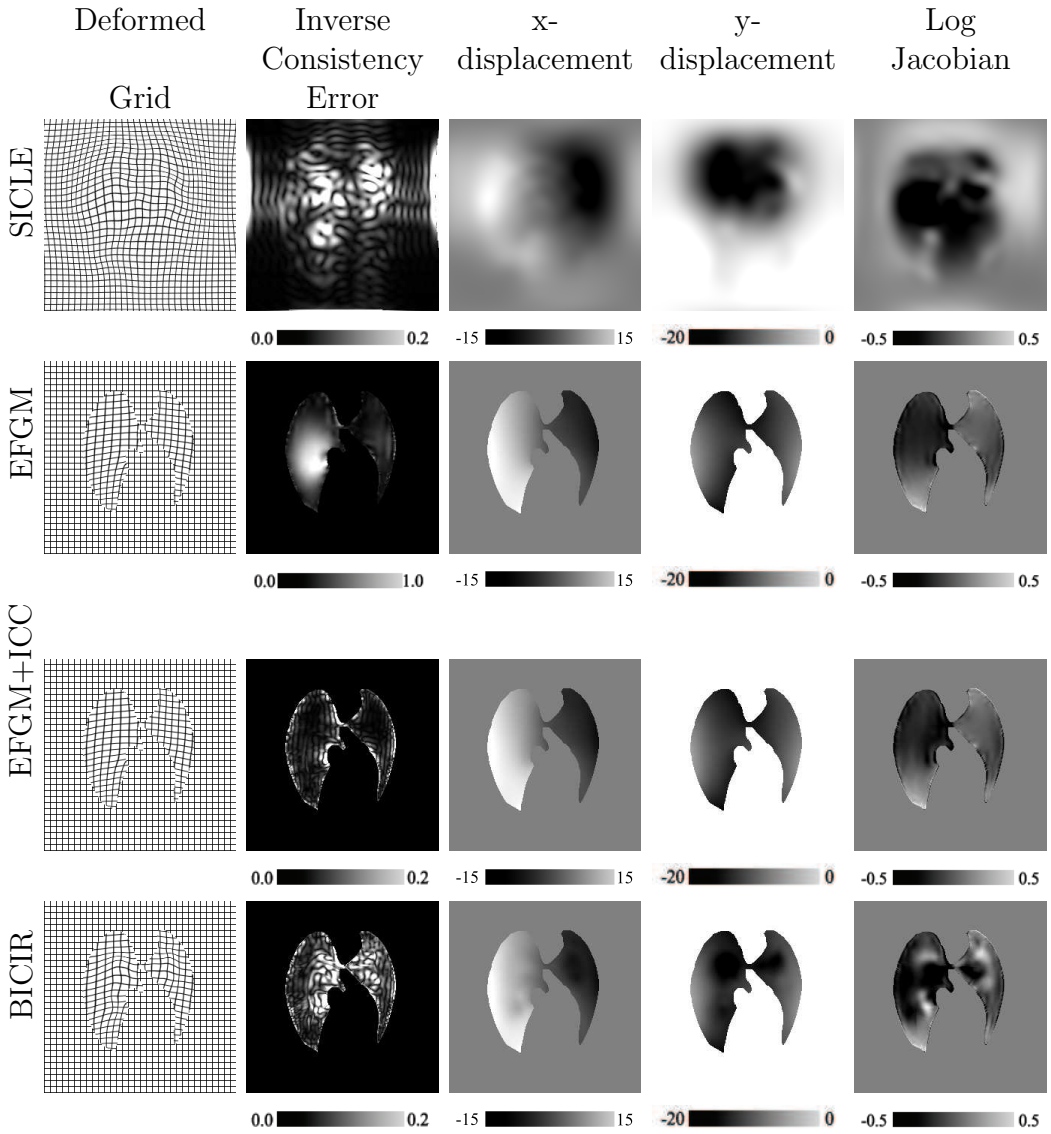

Figure 3.6: From left to right: Deformed grid using the registration deformation fields, Inverse consistency error image, x-displacement image, y-displacement image and the log-Jacobian image. The top row represents results for SICLE registration, the second row represents results after EFGM, the third row represents results after EFGM with inverse consistency and the last row represents the results after BICIR registration, respectively. The average ICE for SICLE, EFGM, EFGM+ICC and BICIR are 0.1, 0.27, 0.04 and 0.08 respectively for the example shown.

Performance Metric	Before Registration	SICLE	BICIR
	Ave. / Max / Std. Dev.	Ave. / Max / Std. Dev.	Ave. / Max / Std. Dev.
Average Intensity Difference (Gray Scale)	15.4/ 21.24/ 3.62	8.52/ 14.49/ 2.97	7.99/ 13.71/ 2.96
Average Boundary Error (Pixels)	6.63/ 10.44/ 1.95	2.08/ 3.05/ 0.58	0.0/ 0.0/ 0.0
Maximum Boundary Error (Pixels)	19.89/ 31.4/ 5.99	18.71/ 30.61/ 9.04	0.0/ 0.0/ 0.0
ROI Relative Overlap (%)	66.7/ 74.32/ 9.6	89.9/ 93.48/ 3.54	100.0/ 100.0/ 0.0
Average ICE (pixels)	-/ -/ -	0.14/ 0.26/ 0.06	0.08/ 0.11/ 0.01
Maximum ICE (pixels)	-/ -/ -	0.87/ 1.8/ 0.41	1.49/ 2.62/ 0.62

Table 3.2: Summary Performance Statistics for 20 2D sheep lung registrations.

3.2 3D Image Registration Results

This section provides image registration results for 3D images including phantom and 3D brain MRI datasets while using parametric as well as arbitrary shaped regions of interest (ROI).

First, simple phantom shapes were studied in Section 3.2.1. The results obtained were compared with SICLE registration method for the simple shapes of ellipsoids that have intensity differences at the boundaries as well as at the interior of the object. The phantom shapes provide easy analysis of the method as the boundary conditions can be analytically and accurately computed and thus inaccuracy in boundary estimation does not affect overall image registration.

The BICIR method was applied to 3D brain MR scans using a variety of inputs. The primary challenge in progressing from 2D image registration to 3D image registration for non-parametric surfaces was difficulty in finding boundary correspondences. Consistent contour based image registration methods in 2D are not as complex as consistent surface based methods in 3D. BICIR method requires a very dense boundary correspondence, which dictates a surface representation that has a very large number of polygons. This leads to a variety of overheads: finding surface correspondence using existing methods is very time consuming. BICIR method requires a distance map from the ROI and if ROI is defined in the real domain using a mesh representation, computation of distance map became using prohibitively expensive for large 3D image volumes. Projection of surfaces onto voxels and assigning boundary correspondence yielded large correspondence and consistency errors at the boundaries

which affect the overall image registration. As a result, this work used either parametric methods or only voxel based methods. Output from a good and consistent surface based registration method is expected to provide even better results.

Section 3.2.2 presents the case studies for registering entire brain images while using a known boundary correspondence for an arbitrarily shaped non-parametric region. The input boundary conditions were computed using binary image registration method performed using SICLE. This correspondence was provided as input to BICIR registration method. The comparison was made between BICIR method using this input with SICLE registration method performed over the image. The BICIR method may suffer from the input boundary conditions in this test. However, the evaluation of method for arbitrarily defined region of interest can be made.

Dependence of BICIR method on input boundary points was addressed using integrated boundary correspondence computation within BICIR registration framework. The regions of interest to be registered were provided as binary images along with the images to be registered. A new region of interest was computed around the original segmentation using spherical or elliptical envelope. These parametric shapes were used to compute boundary correspondences parametrically. Section 3.2.3.1 provides the results for using spherical envelope defining the object boundaries for a given region in brain images from the datasets. Section 3.2.3.2 provides the results for using elliptical envelope defining the object boundaries for a given region in brain images from the datasets. Finally, the results are compared between different initializations and with SICLE method.

3.2.1 3D Phantom Studies

The phantom dataset was constructed using simple shapes of ellipsoids. The phantoms were designed such that there were differences at the boundaries as well as in the interior of the phantom shapes. All the phantom image dimensions were kept at $128 \times 128 \times 128$ with only two intensity values of 0 and 255.

3.2.1.1 3D Ellipsoid Phantom Studies

The phantom images consisted of a number of ellipsoids containing interior ellipsoidal shapes as described in Table 3.3. The ellipsoids provide a more complex shape than cuboids and every point on boundaries may be treated as a special case since different points move by a different displacement and displacement vector at each boundary voxel is unique.

	External x-Size	External y-Size	External z-Size	Internal x-Size	Internal y-Size	Internal z-Size
01	40	32	28	15	10	10
02	40	32	28	15	15	10
03	40	32	28	15	20	10
04	40	40	30	10	10	10
05	40	40	30	15	10	10
06	32	40	28	15	15	15

Table 3.3: Construction of 3D Ellipsoid Phantoms

The background intensities were kept at 0, the intensity of the ellipsoids was kept at 255 and the intensity of the interior shape was kept at 0. A sample size of six

different shapes was generated using ellipsoids of different sizes as well as containing shapes of different sizes inside the ellipsoids. All the ellipsoids were registered together to provide a total of 15 registrations. As with 2-D phantoms, this construction allows exterior boundary matching as well as provides features inside the object of interest, which could be used to drive the intensity-based image registration. Pairwise image registrations were performed between two images from the sample set using BICIR method.

Figures 3.7 and 3.8 represent results from one of the registrations performed between a pair of ellipsoids. Figure 3.7 displays the template ellipsoid image, target ellipsoid image, deformed template ellipsoid image after EFGM phase, deformed template ellipsoid image after the intensity phase and the intensity difference between template and target images before registration, after EFGM phase and after intensity phase, respectively. The top row in Fig. 3.7 shows these results in forward direction and the bottom row shows the same results in reverse direction. The deformed template images at various stages show that after the EFGM phase, the boundaries are registered but the interior of the object looks very different. The interior object is matched after the intensity phase while the exterior boundary correspondence remains unchanged. The difference images show the same pattern as the intensity differences can be seen inside the object as well as at the boundaries. The intensity difference remains only at the interior of the object after EFGM phase and is minimized after the intensity phase. Note that the boundary differences exist only in y- and z-directions for this example. As a result, the initial boundary extension

function and EFGM output contains only zero values in their x-components. The x-displacement column in the last row represents the displacement in x-direction in order to minimize the intensity differences. In the example, sagittal slices are shown for z-displacement fields whereas transverse slices are shown for all other images.

Figure 3.8 shows the deformed grid and displacement fields at different stages of the registration. The first row in the image displays the deformed grid after computation and application of the boundary extension function $\tilde{g}$ and x-, y- and z-displacements in both, forward and reverse directions. The second row shows the corresponding images after the EFGM phase and the third row displays the same images after the intensity phase. The images show that the deformation is localized close to the boundaries of the object after application of only the boundary extension function $\tilde{g}$. The figure shows that the EFGM phase makes the deformation smoother and interpolates the boundary extension function over entire ROI uniformly as per the governing differential equation. This effect can be observed in all the images shown in second row. The third row shows the corresponding images after the EFGM+intensity phase and it can be seen that the deformation has been updated inside the region of interest as a result of intensity difference minimization. Table 3.4 shows the performance metrics for 15 registrations using 3D ellipsoidal phantom images.

3.2.2 Registration of 3D Brain Images

This section presents the results for BICIR method applied to brain images to evaluate the method for arbitrarily shaped regions of interest and comparison to SICLE image

		Ave.Int. Diff.	Ave. ICE	Max. ICE	Total Relative Overlap (%)
Initial	Average	65.155	-	-	75.47
	Std. Dev.	28.81	-	-	12.61
After	Average	17.91	-	-	100
EFGM	Std. Dev.	9.31	-	-	0
After	Average	4.11	0.068	0.8213	100
BICIR	Std. Dev.	1.7	0.034	0.41	0

Table 3.4: Summary Performance Statistics for 15 3D Phantom Experiments.

registration method. The following steps were followed to perform registration on 3D brain scans:

1. **Computing binary masks** The binary masks were computed by dilating the segmentation mask representing the brain segmentation. This was done to reduce the effect of inverse consistency error in matching boundaries. A dilation of 5 voxels was used for these studies. The WEB-spline basis functions were defined over the dilated binary masks.

2. **Computing boundary correspondence** The dilated binary mask images were registered using small-deformation inverse consistent linear-elastic (SICLE) image registration. It may be noted that any method may be used to compute boundary correspondence. The boundary correspondence defined by the chosen method shall remain unchanged during BICIR registration.

3. **Computing EFGM based interpolation** The boundary condition obtained from the SICLE registration was used as an input for EFGM based interpolation to interior of the object.

4. **Intensity-based image registration** The boundary-constrained intensity-based image registration was performed to refine the correspondence in the interior of the object as the final phase.

Figures 3.9 to 3.14 show various stages of an example of image registration between a pair of brain images using irregular shapes describing the region of interest (ROI). The brain images and brain segmentations from NIREP project were used for the brain registrations. BICIR registration utilizes boundary correspondence of input ROIs as the essential boundary condition. For the purpose of these studies, the input boundary correspondences were computed using Small-deformation Inverse Consistent Linear Elastic (SICLE) registration between the binary masks. SICLE method does not guarantee exact boundary match which can result in the brain images containing inside the segmentation to not match with the boundaries of each other, thus providing a relatively poor input. Note that any boundary registration method may be used to find correspondence at boundaries. However, the results will be limited by these boundary correspondences.

The problem associated with inaccurate boundary matching was addressed by using "dilated" segmentation masks thus reducing reliance on the precision of boundary matching. Figure 3.9 shows the dilated segmentation masks and the original brain images used for registration. For these experiments, a value of 5 voxels was used such that the value was larger than the maximum distance between registered pair of mask images in either direction. The figure shows the original brain images and the dilated mask overlaid on the negative of original brain images. As seen in the figure,

the mask extends the boundaries of the object in all directions. The mask images were registered together using SICLE registration and the boundary correspondence at the boundaries was used as an input for the EFGM method. The correspondence obtained using EFGM were further refined using boundary-constrained intensity registration. Figures 3.10 to 3.14 show the images generated at various stages of image registration.

Figure 3.10 shows the slices extracted from various registration stages in forward direction in Transverse, Sagittal and Coronal orientations from top panel to bottom panel, respectively. The first two columns represent the original template and the target images, respectively. Following registration, the deformed template will be expected to resemble the target image and the results from the figure show that the template image gets incrementally closer to the target image. The third column represents the deformed template image after EFGM registration. At this stage, the boundary matching is good while the matching inside interior of the object and the sulci folds improves further after the intensity registration phase as shown in the fourth column. This can be seen even more clearly in the color overlay images in the last three columns with intensity value from template image represented in red color and intensity values from the target image represented in green color. A mismatch will show as a predominantly green or red region while shades of yellow represent a good match. The fifth column shows that the images have large regions of mismatch before registration, which are reduced at the boundaries following the EFGM step as seen in sixth panel. The seventh panel shows the final results after intensity phase and further improves the internal correspondence considerably.

The results are similar for the registration in the opposite direction, as seen in Figure 3.11. The boundaries are matched well after EFGM phase and the intensity information further improves the correspondence during the intensity phase.

Figures 3.12 to 3.14 show the x-, y- and z-displacements for image registration of brain images shown in Figures 3.9 to 3.11. The figures show the displacements as images at various stages of registration, i.e., after extending boundary conditions, after EFGM and after BICIR. Transverse, Sagittal and Coronal slices of the displacement fields are also displayed. The figures show that while the boundary extension function is limited to a small band around boundary, the EFGM extends the boundary correspondence uniformly to interior of he object. Finally, intensity registration updates the dislacement fields. The figures clearly show that the boundary extension function and EFGM outputs do not contain any structural information about interior of object, but the displacement fields after intensity registration phase clearly show the various structures inside the object that the intensity registration phase matched.

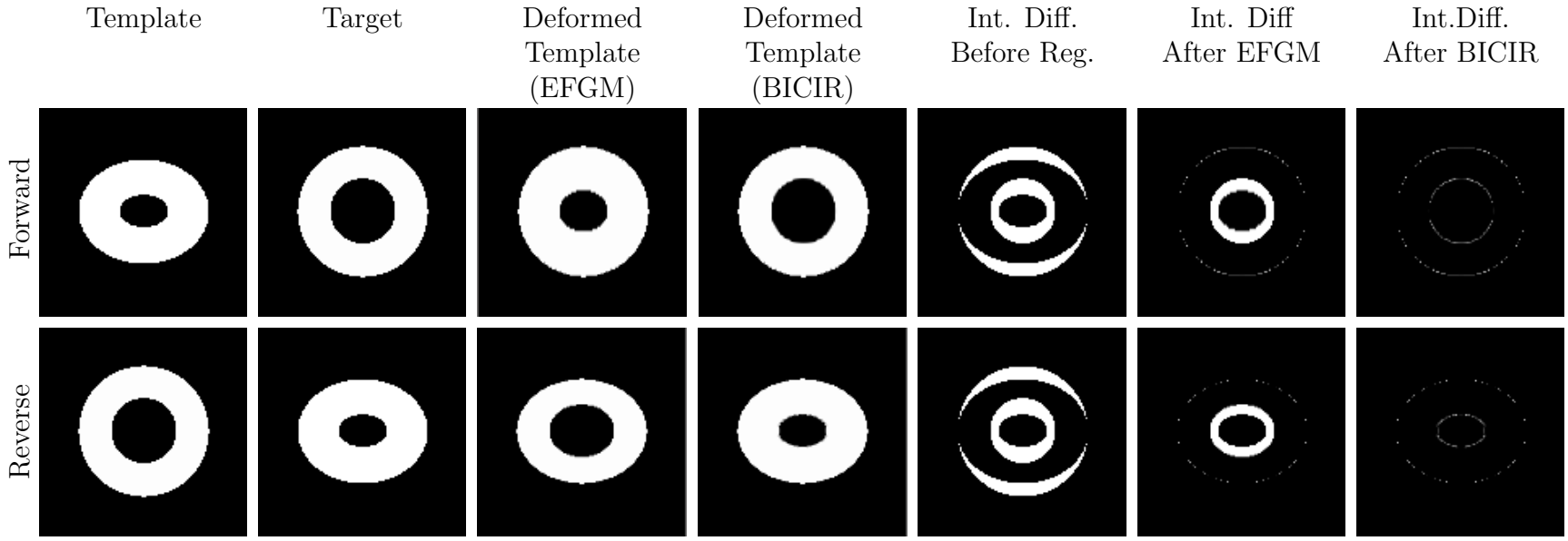

Figure 3.7: Top row (From Left to Right): Transverse slices of Template, Target, Deformed Template After Boundary Matching using EFGM, Deformed Template after BICIR, Absolute Intensity Difference image before registration, Absolute Intensity Difference image after EFGM and Absolute Intensity Difference image after BICIR registration, respectively. Bottom row shows the same results for the reverse direction.

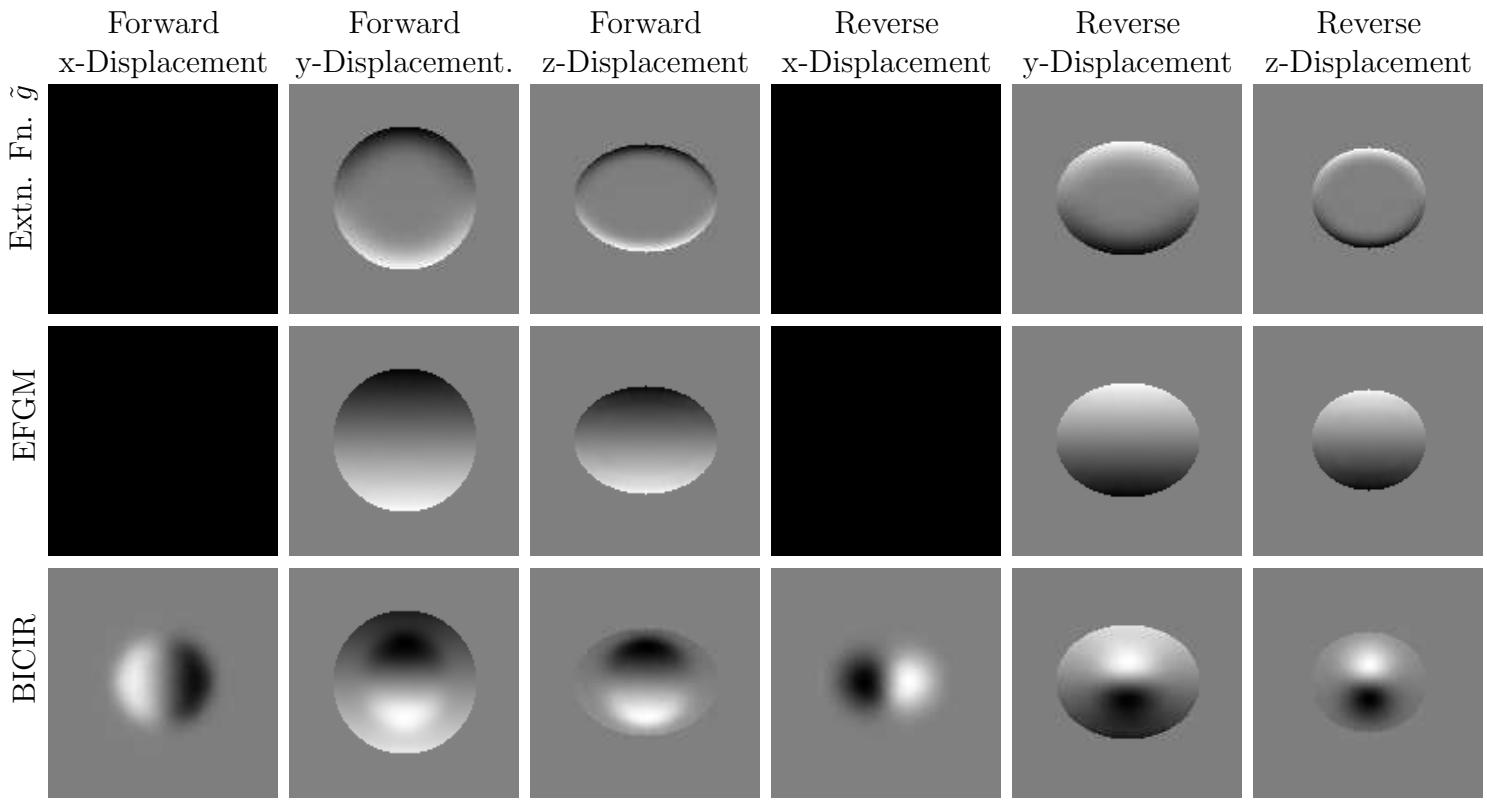

Figure 3.8: 3D Ellipsoid Shaped Phantom Registration Results. Top row (From Left to Right): x-component of transformation in forward direction, y-component of transformation in forward direction, z-component of transformation in forward direction, x-component of transformation in reverse direction, y-component of transformation in reverse direction, and z-component of transformation in reverse direction, respectively. The top row corresponds to only the boundary extension function $\tilde{g}$, the middle row corresponds to the results obtained using boundary matching through EFGM using WEB splines, and the bottom row corresponds to results obtained after BICIR registration, where WEB spline based intensity registration algorithm is initialized using results from EFGM, respectively. It may be noted that the forward and reverse registrations are performed simultaneously, while minimizing inverse consistency in every iteration.

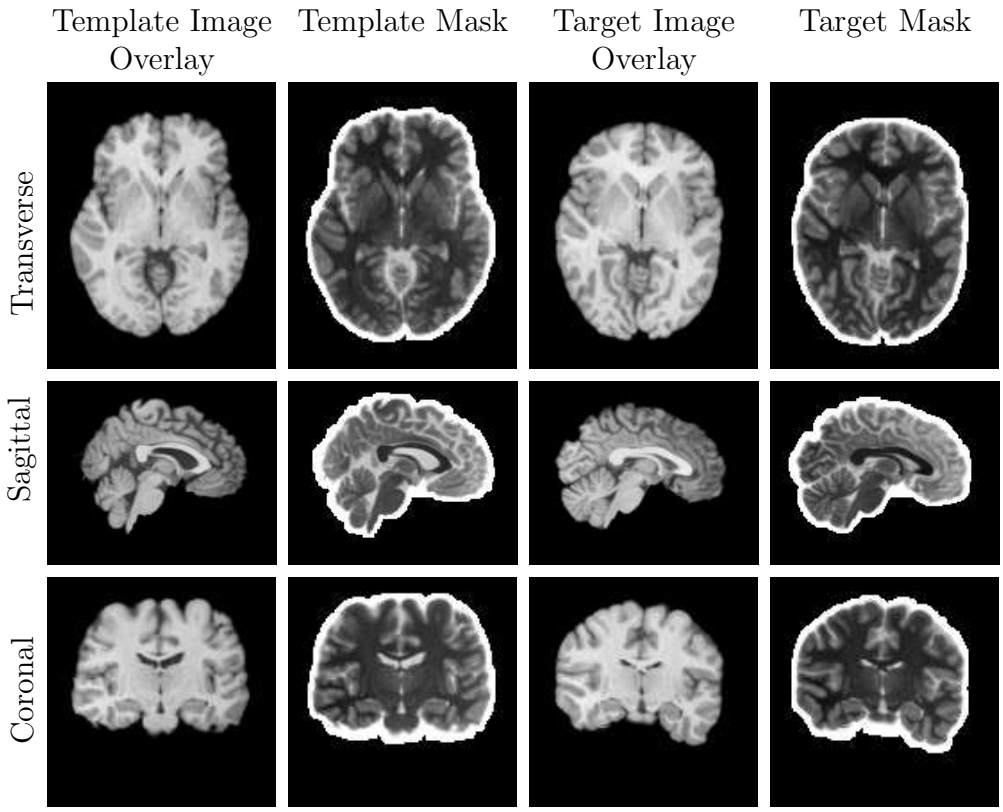

Figure 3.9: Input ROIs for Brain Image Registrations Top row (From Left to Right): Template, template ROI overlaid on template image, target, and target ROI overlaid on the target image, respectively. The top, middle and bottom rows represent center slices in transverse, sagittal and coronal directions, respectively.

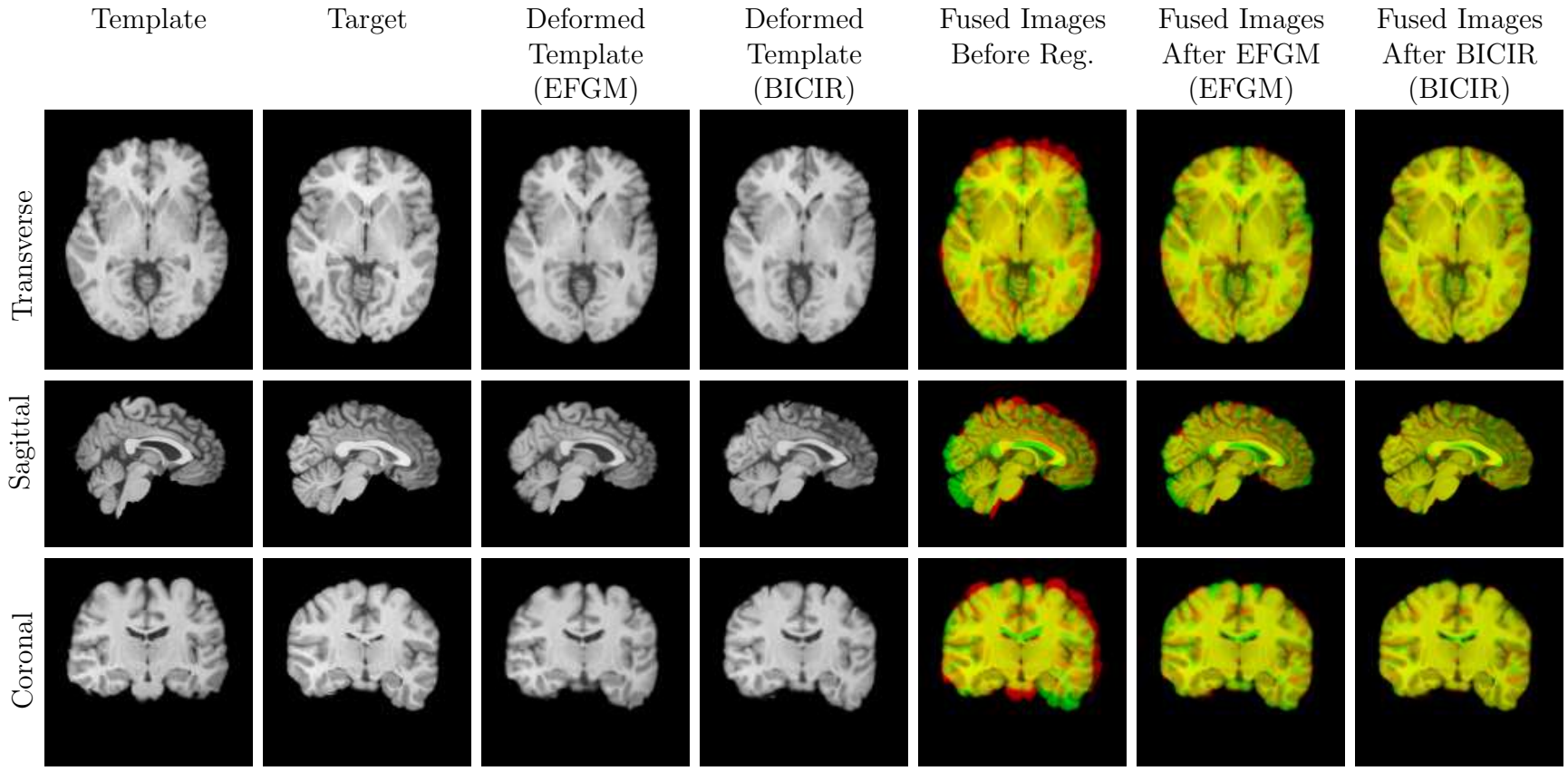

Figure 3.10: Registration results for 3-D Brain Images in Forward Direction. (From Left to Right): Template Image, Target Image, Deformed Template After Boundary Matching using EFGM, Deformed Template after BICIR, Fused Template and Target Images before Registration, Fused Deformed Template and Target Images after Boundary Matching using EFGM and Deformed Template using BICIR Fused with Target Image, respectively. The top, middle and bottom rows represent the slices in transverse, sagittal and coronal directions, respectively. The fused images use image intensity values from template as red and image intensity values from target image as green channel.

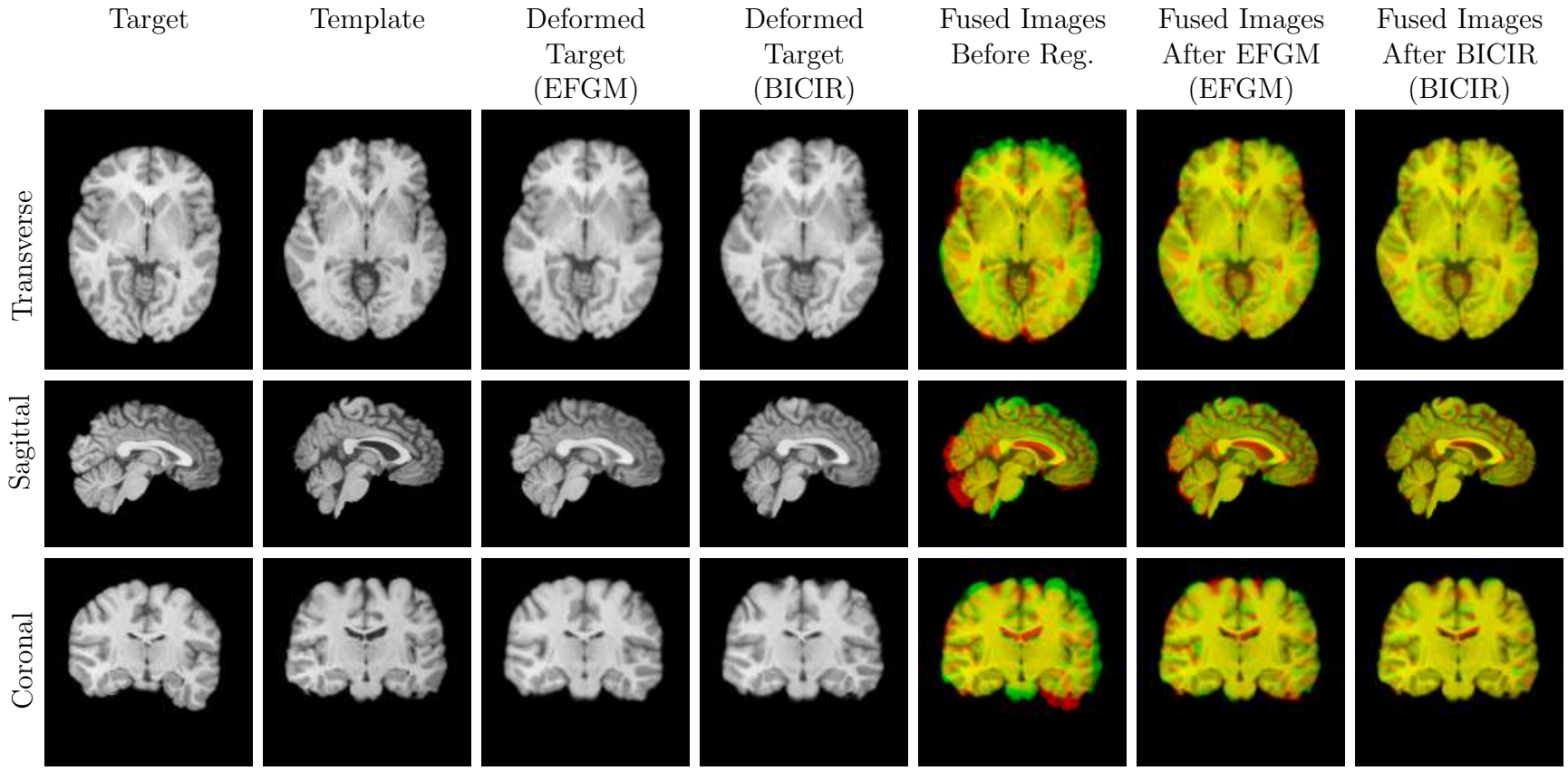

Figure 3.11: Registration results for 3-D Brain Images in Reverse Direction. (From Left to Right): Target Image, Template Image, Deformed Target After Boundary Matching using EFGM, Deformed Target after BICIR, Fused Target and Template Images before Registration, Fused Deformed Target and Template Images after Boundary Matching using EFGM and Deformed Target using BICIR Fused with Template Image, respectively. The top, middle and bottom rows represent the slices in transverse, sagittal and coronal directions, respectively. The fused images use image intensity values from target as red and image intensity values from template image as green channel.

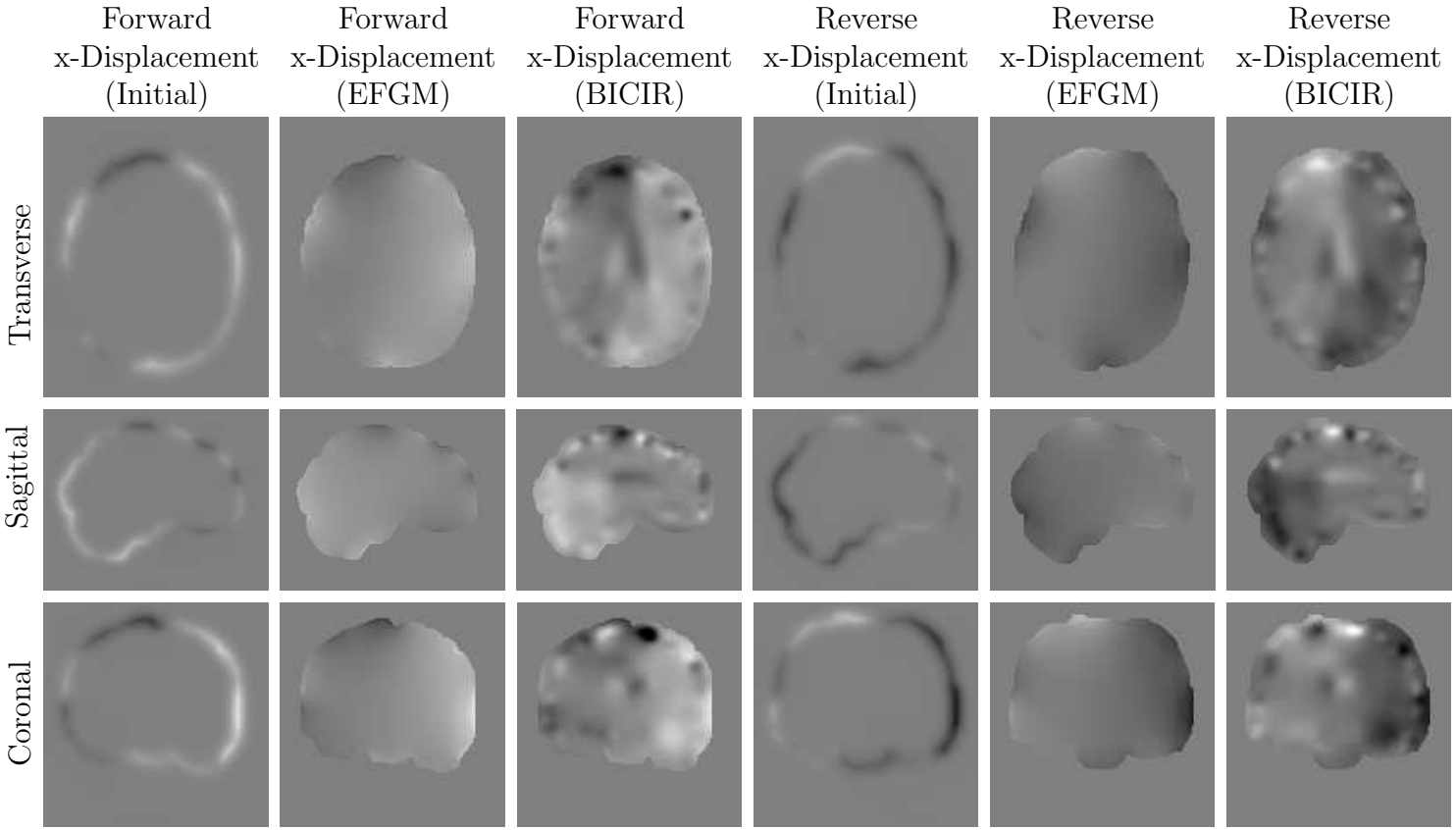

Figure 3.12: Displacement Fields for 3-D Brain Image Registration in x-Direction. (From Left to Right): x-Component of Boundary Extension Function in Forward Direction, x-Component of Displacement in Forward Direction after EFGM, x-Component of Displacement in Forward Direction after BICIR, x-Component of Boundary Extension Function in Reverse Direction, x-Component of Displacement in Reverse Direction after EFGM, x-Component of Displacement in Reverse Direction after BICIR, The top, middle and bottom rows represent the slices in transverse, sagittal and coronal directions, respectively.

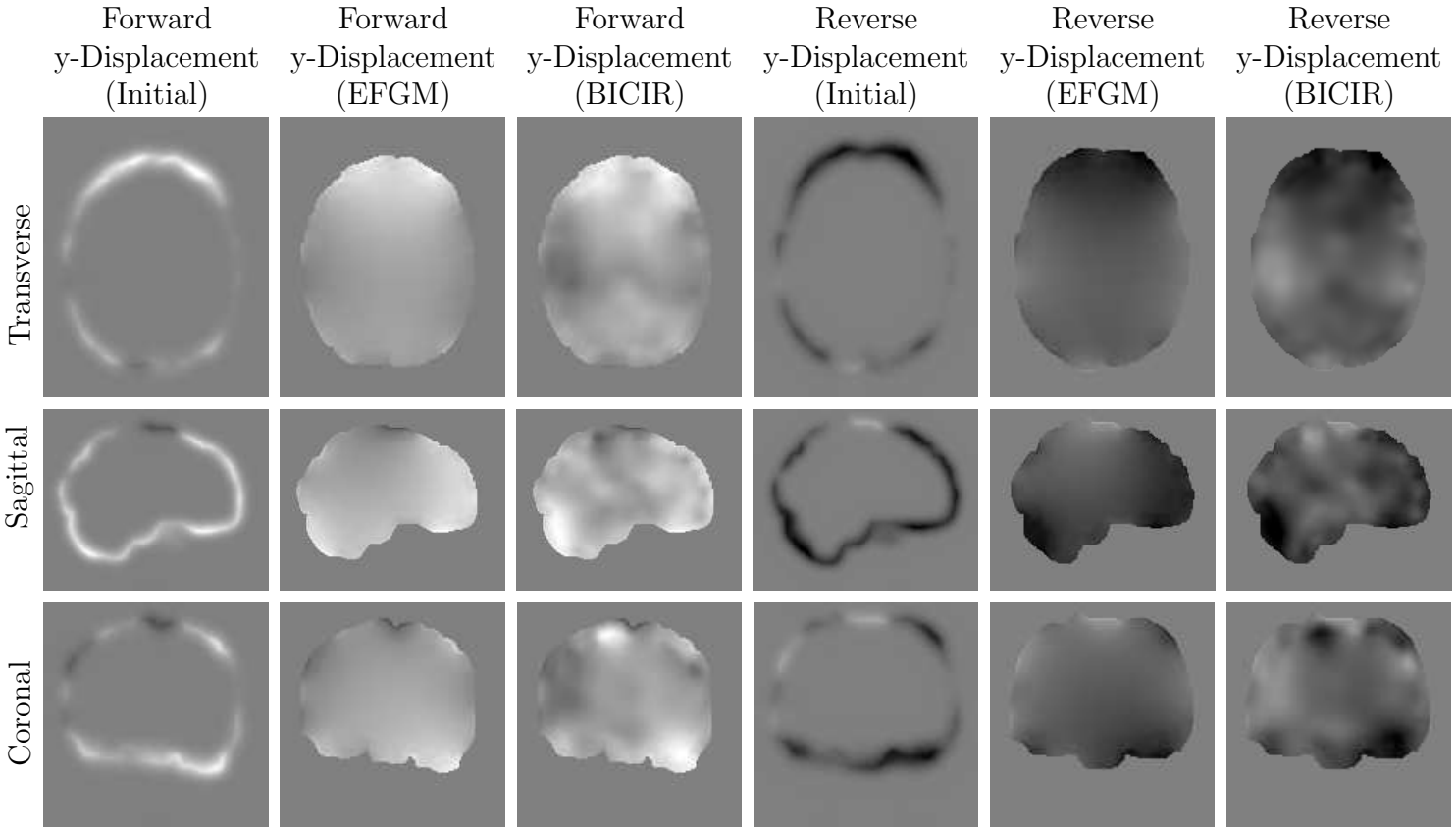

Figure 3.13: Displacement Fields for 3-D Brain Image Registration in y-Direction. (From Left to Right): y-Component of Boundary Extension Function in Forward Direction, y-Component of Displacement in Forward Direction after EFGM, y-Component of Displacement in Forward Direction after BICIR, y-Component of Boundary Extension Function in Reverse Direction, x-Component of Displacement in Reverse Direction after EFGM, y-Component of Displacement in Reverse Direction after BICIR, The top, middle and bottom rows represent the slices in transverse, sagittal and coronal directions, respectively.

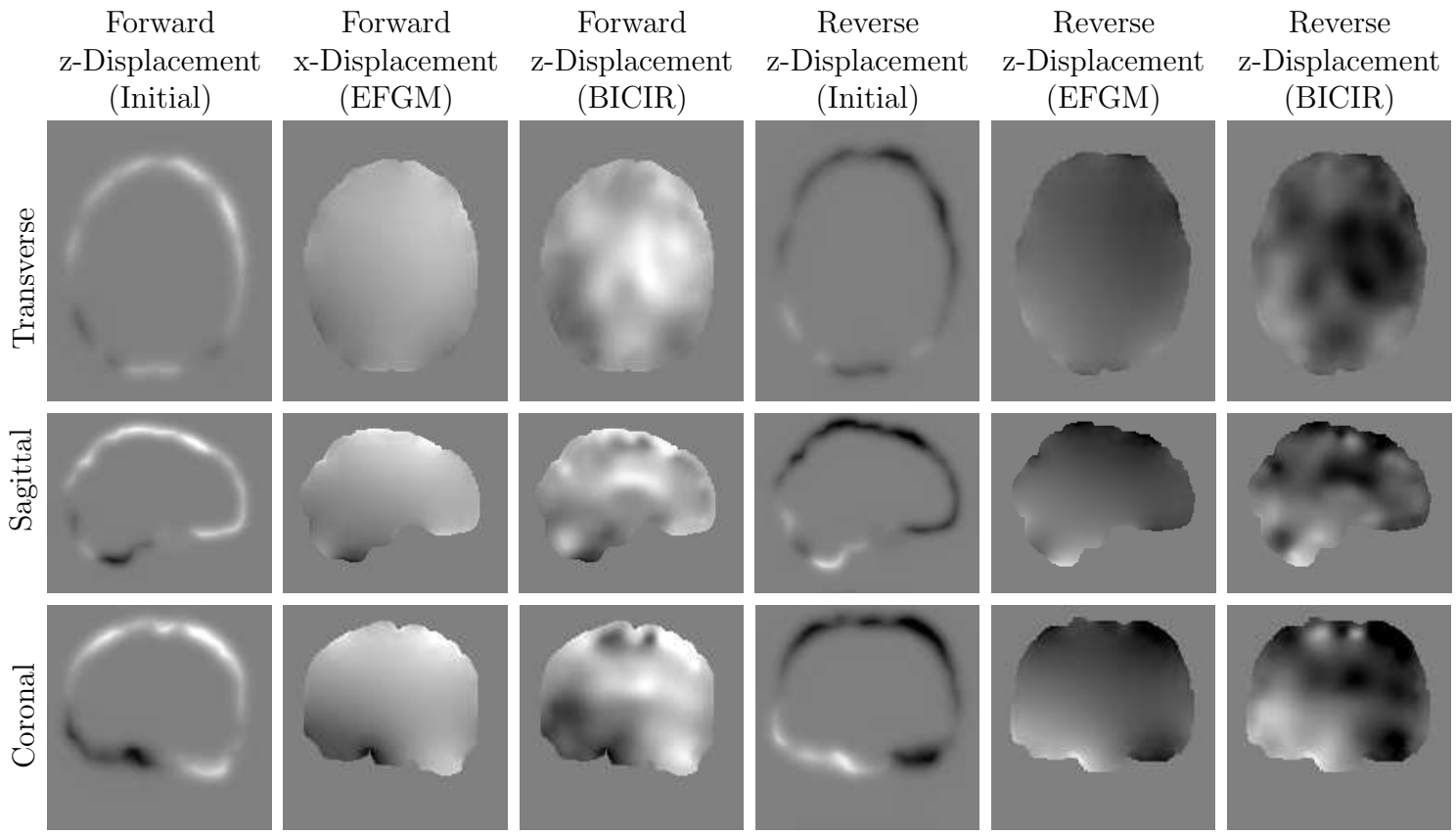

Figure 3.14: Displacement Fields for 3-D Brain Image Registration in z-Direction. (From Left to Right): z-Component of Boundary Extension Function in Forward Direction, z-Component of Displacement in Forward Direction after EFGM, z-Component of Displacement in Forward Direction after BICIR, z-Component of Boundary Extension Function in Reverse Direction, z-Component of Displacement in Reverse Direction after EFGM, z-Component of Displacement in Reverse Direction after BICIR, The top, middle and bottom rows represent the slices in transverse, sagittal and coronal directions, respectively.

Figures 3.15 to Figure 3.17 show the cost profiles with respect to the number of iterations during the intensity phase. At beginning of intensity phase, the forward and reverse registration is computed between outputs of EFGM phase and corresponding target image in that direction, respectively. As a result, the initial similarity cost is not equal between forward and reverse directions, as can be seen in Figure 3.15. The figure further shows that after the convergence of intensity cost at a larger knot spacing, the increase in resolution by changing knot spacing from 8 voxels to 4 voxels at iteration no. 200 results in a sharper slope and thus faster refinement of local correspondence.

Figure 3.16 shows the cost profile for the image registration. The inverse consistency cost initially decreases as the output of EFGM is not necessarily inverse consistent and initial intensity based refinement may improve inverse consistency. As the iterations progress, however, the deformation gets larger and inverse consistency error increases. Upon introduction of larger number of splines as a result of increased resolution, the increased degree of freedom at iteration no. 200 results in a sudden drop in inverse consistency. For the example shown, the average inverse consistency error was computed to be 0.019 and 0.015 inside the region of interest.

Figure 3.17 shows the cost profile for regularization energy cost and the figure shows that the total deformation energy increases with number of iterations.

The same datasets were registered using SICLE registration method and compared against results from BICIR method. Table 3.5 shows the comparison between SICLE and BICIR method for brain registrations over 15 registrations.

		Ave. Int. Diff.	Ave. ICE	Max. ICE	Overall Relative Overlap (%)
Initial	Average	-	-	-	83.59
	Std. Dev.	-	-	-	3.09
BICIR	Average	16.33	0.0078	1.211	96.65
	Std. Dev.	0.959	0.003	0.954	0.27
SICLE	Average	17.81	0.0324	0.42	96.07
	Std. Dev.	0.89	0.0039	0.11	0.26

Table 3.5: Comparison between BICIR and SICLE over 15 Brain Registrations.

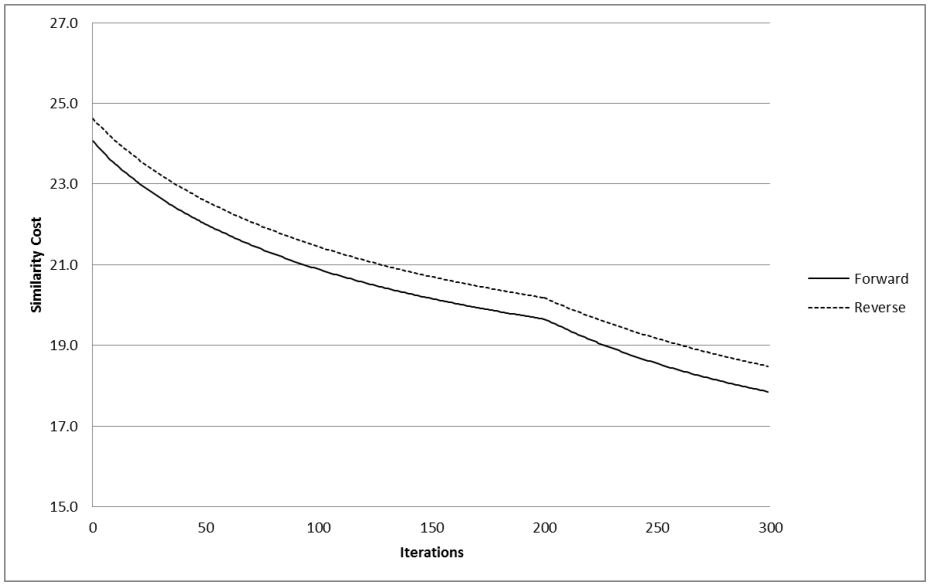

Figure 3.15: Similarity Cost Profile During Intensity Phase. The similarity costs in forward and reverse directions are shown in solid and dotted lines, respectively. The intensity phase consisted of 200 iterations with grid spacing of 8 voxels and 100 iterations with grid spacing of 4 voxels.

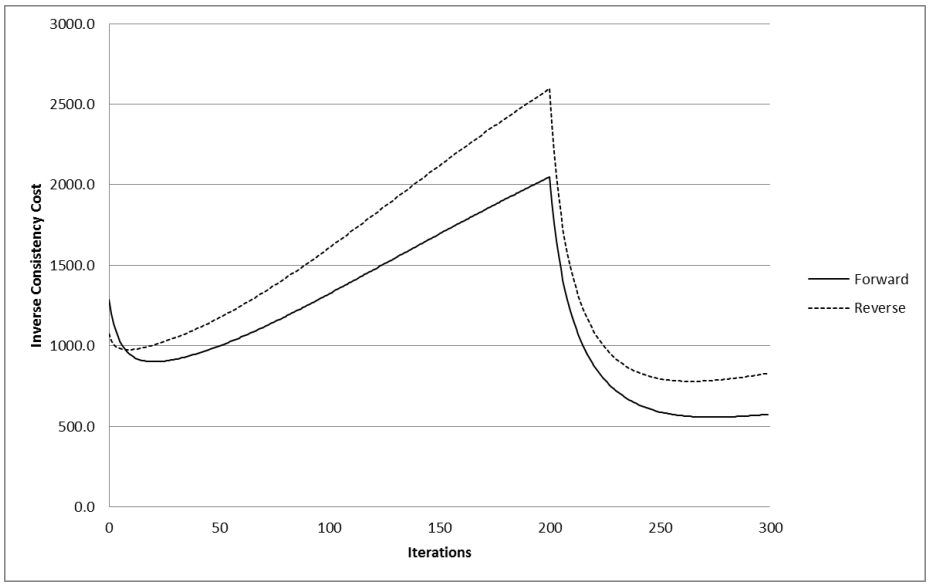

Figure 3.16: Inverse Consistency Cost Profile During Intensity Phase. The inverse consistency costs in forward and reverse directions are shown in solid and dotted lines, respectively. The intensity phase consisted of 200 iterations with grid spacing of 8 voxels and 100 iterations with grid spacing of 4 voxels.

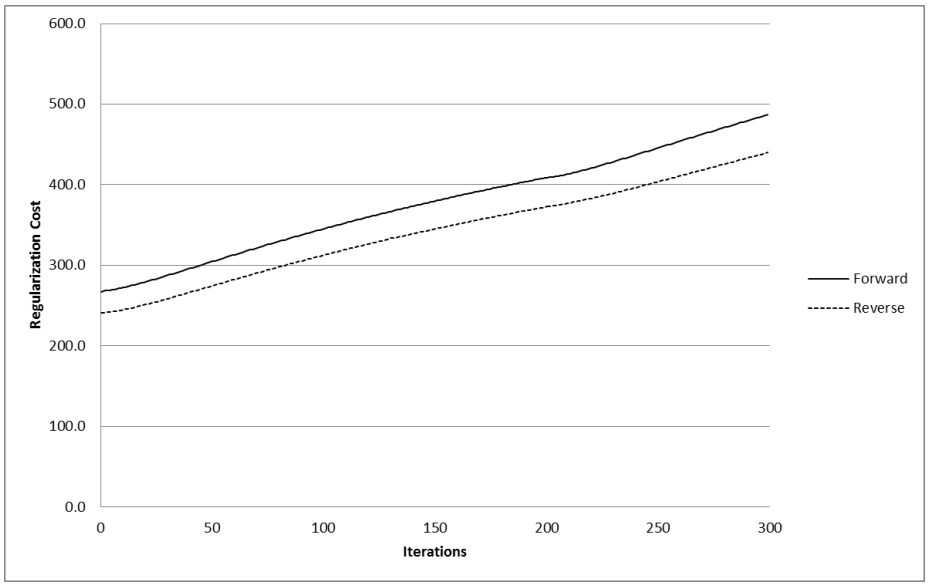

Figure 3.17: Regularization Cost Profile During Intensity Phase. The similarity costs in forward and reverse directions are shown in solid and dotted lines, respectively. The intensity phase consisted of 200 iterations with grid spacing of 8 voxels and 100 iterations with grid spacing of 4 voxels.

The results show that overall, the BICIR method performed better than SICLE registration method using square of intensity difference, inverse consistency error and relative overlaps. The maximum inverse consistency error was found to be higher in the BICIR method. This is primarily due to the BICIR method's inability to update boundary conditions and any consistency error or boundary mismatch remains unchanged through intensity registration. However, the method performs better than SICLE registration method using the metrics discussed above. We believe that the results will be even more in favor of BICIR method if a better method for boundary registration is employed. The next section studies the registration results for spherical envelope describing the ROI.

3.2.3 Registration of objects inside 3D Brain Images

This section discusses evaluation of BICIR registration method using integrated boundary correspondence computation methods and comparison of various boundary correspondence computation methods with each other and with SICLE. The registrations were carried out on brain MR scans. The brain MR scans and the segmentations were taken from the NIREP database. For this validation, only one of the segmentations was used. A total of 16 datasets were used for registering image data. The raw images corresponded to image size of $256 \times 300 \times 256$ in sagittal, coronal and transverse directions, respectively. Due to implementation constraints specific to the way algorithm has been implemented, a padding of 10 slices was used on either side in coronal direction. This yields an image volume of $256 \times 320 \times 256$, which meets the requirement of image dimensions being integer multiples of knot

spacing. It may be noted that this constraint comes from the specific implementation and is not a limitation of BICIR registration method.

NIREP database includes 33 different segmentations per brain scan such that each segmentation corresponds to an anatomical region as identified by experts. For the purpose of validation of BICIR method, only one of the segmentations was used. The input to BICIR method consisted of entire brain MR scan and a binary image defining the object. Figures 3.18 to Figure 3.20 show the images for all the brains and the segmentation defining the object of interest. The brighter region in the images corresponds to region in brain hand segmented by expert to create a validation database.

As seen in previous section, the boundary correspondence computation dictates overall performance of the method. Computing surfaces from the segmented objects and performing surface based image registration presents one option. However, this work assumes the surface registration as an input and only investigational but consistent boundary matching methods will be addressed. Two different methods were used for computing boundary correspondences: using a spherical envelope and ellipsoidal envelope. 3.2.3.1 presents the results where initial ROI was defined to be a spherical envelope fitting snugly over the segmented object. We analytically computed correspondence between two spherical ROIs in template and target images, respectively, and used it as the input to the BICIR registration. 3.2.3.2 presents the BICIR registration results where ellipsoidal envelopes defined the ROIs to be registered. Analytical solution to the ellipsoidal boundary matching provides the boundary

correspondence to BICIR method. Section 3.2.4 presents the comparison between the two methods and with SICLE.

3.2.3.1 Registration using Spherical Envelopes

This section discusses results for BICIR registration using an integrated spherical envelope based boundary computation method. One of the images was taken as a template and registered with all the other images. The inputs to the BICIR method comprised the two grayscale 3D Brain MR scans and corresponding anatomical object as shown in Figures 3.18 to 3.20. The following steps were followed to compute the spherical ROI and boundary correspondence:

- The boundary points are extracted from the input segmentations for template and target, respectively.

- Spherical envelope is computed for the set of boundary points in each direction. The following rule was used to compute centers and radii of the spheres:

  Let $X = \{x_1, x_2, ..., x_n\}$ represent the sets of boundary points in an image in voxel coordinates, and let $\{C, r\}$ represent the center and radius for the spherical envelope, then

$$C = \frac{1}{n}\sum_{i=1}^{n} x_i r = max(x_i - C) \tag{3.2}$$

- Binary mask is computed within the registration framework with dilated sphere computed above. The dilation is necessary to allow some "room" for deformation and was achieved by just increasing computed radius by a factor of 10%.

- Registration framework computes the boundary correspondence such that the spheres correspondence. Let $\{C_1, r_1\}$ and $\{C_2, r_2\}$ represent the two spheres 1 and 2 in template and target images, respectively, then a point x_1 on boundary of sphere 1 will be mapped to point $x_1{}'$ on the boundary of the sphere 2 as follows:

$$x_1{}' = (x_1 - C_1) * \frac{r_2}{r_1} + C_2 \tag{3.3}$$

Following these steps, BICIR framework computes the boundary extension function and performs EFGM and boundary constrained intensity registration. Figures 3.21 to 3.24 show results for registration between one NIREP dataset (na01) and the remaining 15 datasets. Figure 3.21 shows the deformed images in both directions fused with the target images. In the color images, the red and green colors correspond to deformed images and target images, respectively. The overlay will ideally be yellow where the images match perfectly and any hint of green or red color represents difference in intensities. The images show that the intensity matching is good in the interior of the object while there are more differences towards the boundaries. The images also show that using spherical envelopes, the EFGM method does not provide perfect boundary match. The boundaries match better after the intensity phase.

The spherical envelope shows the feasibility of this method to provide good results while being fast. However, the ROI will be quite large compared to more complicated envelopes. In addition, spherical correspondences are insensitive to orientation of the region contained. Next section attempts at solving these issues by using ellipsoidal envelope. Unlike irregular shapes, it is straightforward to compute

correspondence between two ellipsoids with known axes and radii.

3.2.3.2 Registration of objects inside 3D Brain Images using Ellipsoid Envelopes

Given a set of points, the ellipsoid containing these points in a 3D space needs to be computed by minimizing the distance from each point to the ellipsoid while updating ellipsoid parameters accordingly. The parameters for ellipsoids are: diameter of the three axes, location of center and the orientation. The orientation of ellipsoid was taken to align with the three coordinate axes. Let r_1, r_2, r_3 and $C = (C_1, C_2, C_3)$ represent the half length along the coordinate axes and center of the ellipsoid providing a tight envelope for the segmentation. Let $P = \{P_1, P_2, \ldots, P_n\}$ represent set of points representing the segmented object boundaries such that $P_i = [x_{1,i}, x_{2,i}, x_{3,i}]$. Then, for a point lying on the ellipsoid, the following will be true:

$$\frac{(x_{1,i} - C_1)^2}{{r_1}^2} + \frac{(x_{2,i} - C_2)^2}{{r_2}^2} + \frac{(x_{3,i} - C_3)^2}{{r_3}^2} = 1 \tag{3.4}$$

When this equation is applied to the point set P, the following set of linear equations is achieved:

$$Ay = b \tag{3.5}$$

Where, $A_{i,j} = (x_{j,i} - C_j)^2$, $b = [1,\ 1,\ 1]^t$ and $y = [1/{r_1}^2,\ 1/{r_2}^2,\ 1/{r_3}^2]^t$. C was computed as the centroid of the points. This equation is solved for y and the positive roots of the solution represent the least square fit of an ellipsoid at centroid of the point set and aligned with the coordinate axes. The radii of the ellipsoid were then iteratively and proportionately increased till all the points lie inside the ellipsoid.

This is done by iteratively increasing radii and checking for signed pseudo distance described in Eq. 3.6 to be less than zero for all points.

$$d(x, E) = \frac{(x_1 - C_1)^2}{{r_1}^2} + \frac{(x_2 - C_2)^2}{{r_2}^2} + \frac{(x_3 - C_3)^2}{{r_3}^2} - 1.0 \tag{3.6}$$

Only solutions for which all the signed distances are negative were considered since that guarantees the ellipsoid containing all the points. Let the solution for template and target boundary points be $E_S(C_S, r_S)$ and $E_T(C_T, r_T)$ respectively after appropriate buffer adjustment in the half lengths to allow cushion for deformation during registration. The BICIR framework projects these ellipsoids on the voxelized image to obtain two sets of boundary points, X and Y, respectively. Then, analytical correspondence between the boundary points is defined as follows:

$$x'_{i,j} = \frac{r_{j,T}}{r_{j,S}}(x_{i,j} - C_{j,S}) + C_{j,T} \tag{3.7}$$

The analytically computed points provide a consistent mapping at boundaries since the projected points from E_S on E_T always map back to same points on E_1 and vice versa. The integrated registration framework computes these points and uses as input to the EFGM phase. Following EFGM, an inverse consistency minimization is performed followed by a boundary constrained consistent intensity registration during the intensity registration phase.

Figures 3.25 to 3.28 show the registration results for the image registration between one image from NIREP database to the other images using ellipsoid envelopes.

Figure 3.25 shows the template and target images fused with the the corresponding objects of interest overlaid on them, respectively. The figure shows the deformed images in forward and reverse directions after EFGM and BICIR phase. The region of image used for registration is ellipsoidal and envelopes the original object of interest. The deformed images are fused with the target brain image. The registration using ellipsoidal uses only information inside ellipsoidal ROI to register the two images together. Images in different orientations show that the intensity matching is better towards interior of object whereas the boundaries are not that well matched due to initial boundary conditions.

Figures 3.25 to 3.28 show all the registered images in frame of reference of one image chosen as a reference image. If the images look similar inside the ROI, it represents a good and consistent registration across the entire set of images. The figure shows that the intensity match is good around the original region of interest while the regions closer to boundaries do not match very well.

3.2.4 Comparison of Various Methods

Table 3.6 provides the results for image registrations carried out using NIREP database. NIREP database image $na01$ was used as the template and registered with all other images in the database. The registrations were performed on a multiprocessor computer with 24 Intel Xeon X5670, 2.93 GHz CPUs. The programs were not written to utilize the parallel processing. This yielded a total of 15 bi-directional registrations. Region indexed as 22 was used as the input anatomical object to be registered. The determination on which region to choose was performed based on

the various parameters such as quality of segmentation, intensity profile inside the segmented object and the relative proximity of the ROIs. Relative proximity of ROIs does not affect the integrated BICIR registration method. However, it may affect other registration methods that register the entire images.

The table shows that using the relative overlap and similarity metrics, both BICIR based registration methods performed better than SICLE registration method. Within integrated registration methods, the ellipsoid performed slightly better than the spherical envelope. Using the time as a comparison metric, the BICIR based integrated methods were significantly faster than SICLE for complete image registration. Within the BICIR framework, the methods were close to each other. This may be explained as follows: the spherical and elliptical boundaries are easiest to compute but they also contain much larger volume inside ROI when compared to a convex hull, however, the volume contained is much smaller than the volume of entire image. Moreover, the difference in computational times between SICLE and BICIR methods is not linear with respect to the volume contained due to overheads in computation of basis function for BICIR. In addition, there is a scope for optimization of BICIR method which may reduce the computation time further.

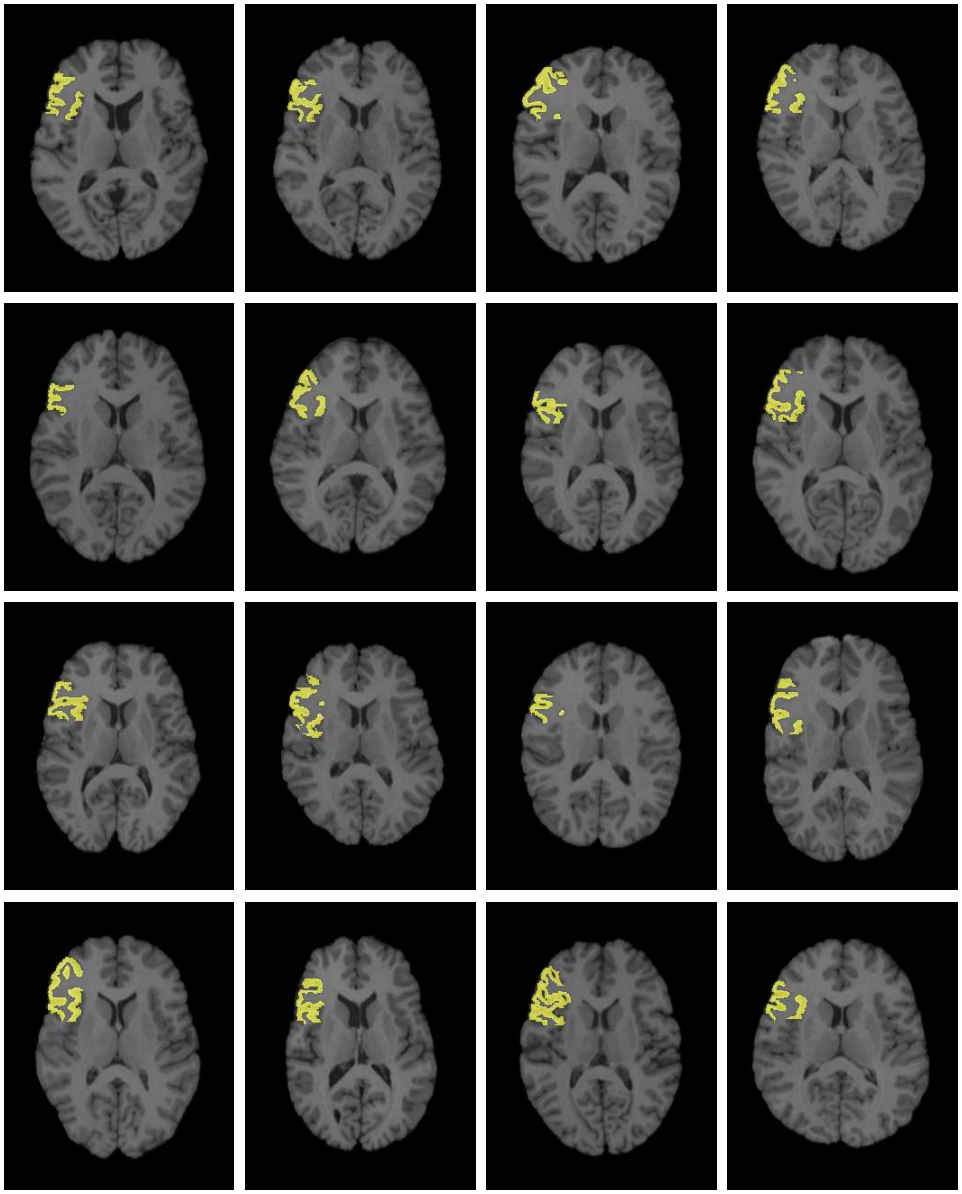

Figure 3.18: Transverse Slices of Brain Image Registration Datasets with ROIs Overlaid. The figure shows the transverse slices of 16 datasets from NIREP project with ROI highlighted.

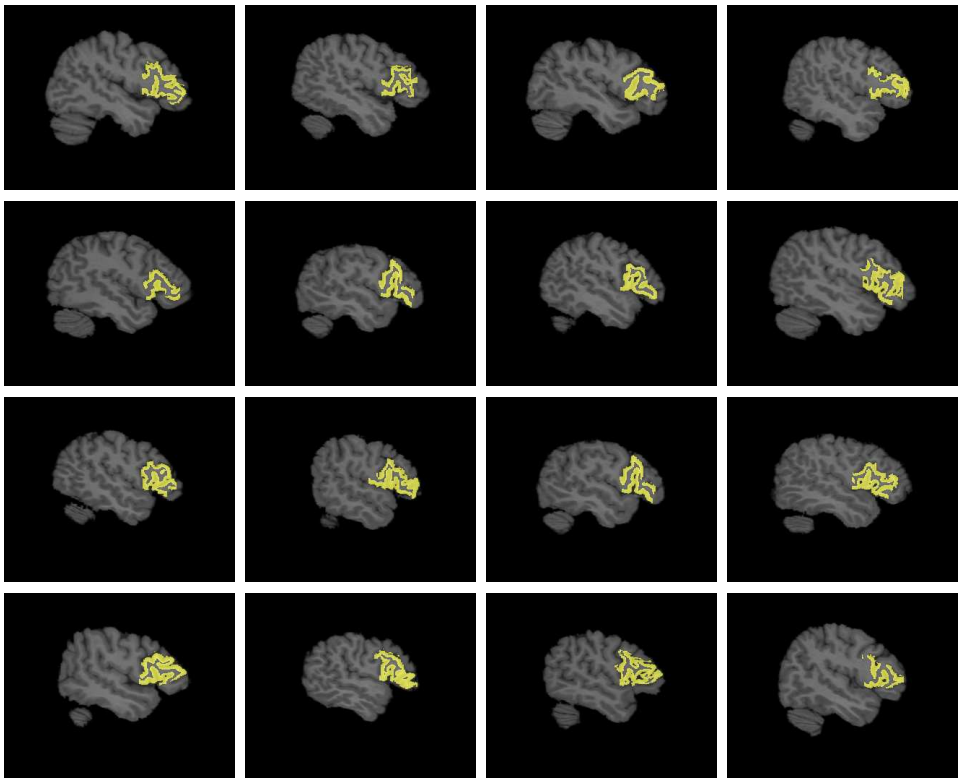

Figure 3.19: Sagittal Slices of Brain Image Registration Datasets with ROIs Overlaid. The figure shows the sagittal slices of 16 datasets from NIREP project with ROI highlighted.

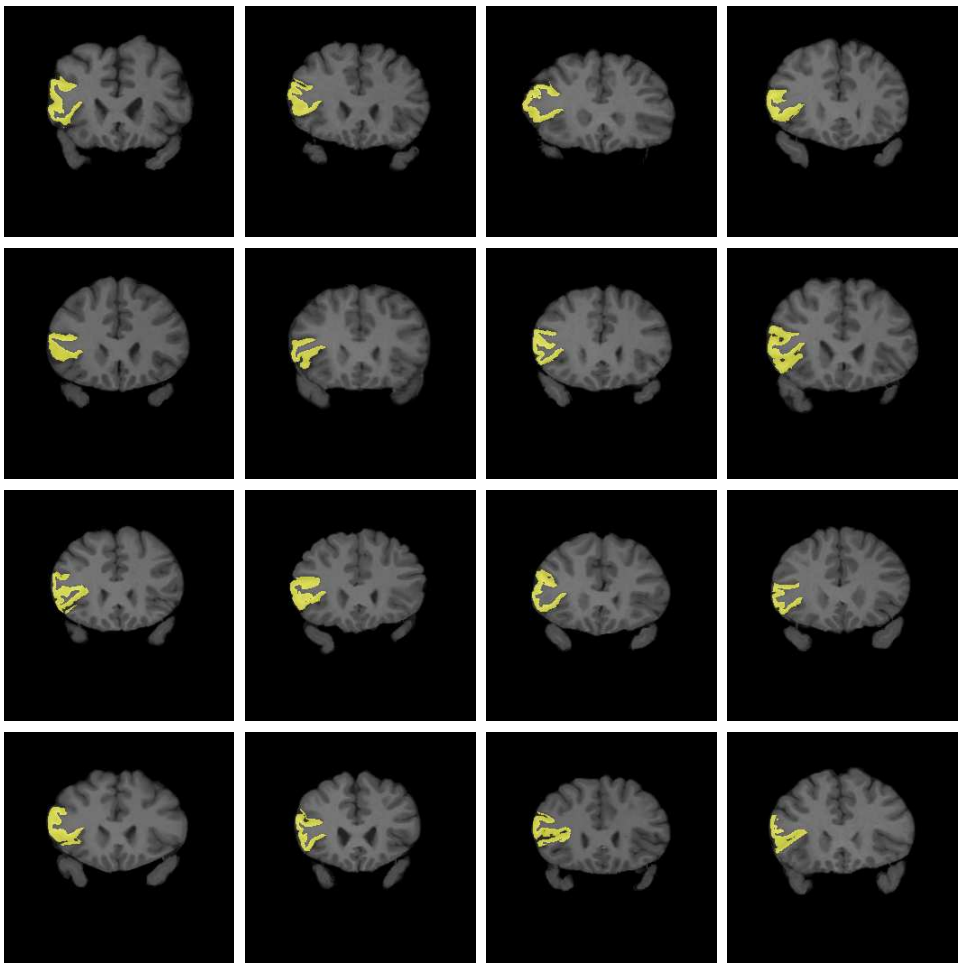

Figure 3.20: Coronal Slices of Brain Image Registration Datasets with ROIs Overlaid. The figure shows the coronal slices of 16 datasets from NIREP project with ROI highlighted.

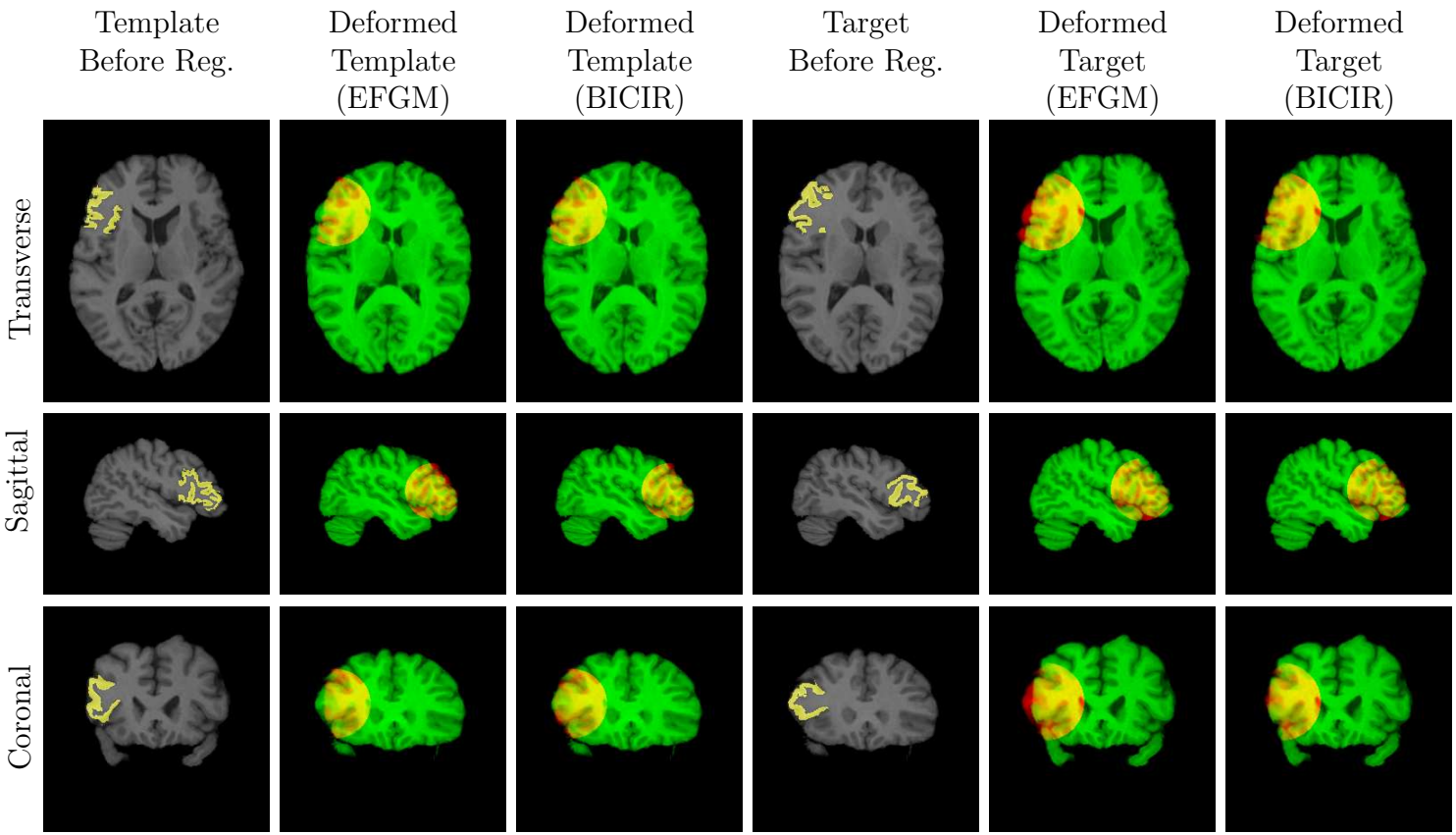

Figure 3.21: Results for a Pair of Image Registration between Two NIREP Brain Datasets. The figure shows the forward and reverse image registration results for a pair of NIREP datasets. The first three columns show the original template image, deformed image after EFGM and deformed image after BICIR registration, respectively. The next three columns show the same results in reverse direction. The rows show from top to bottom: transverse, sagittal and coronal images.

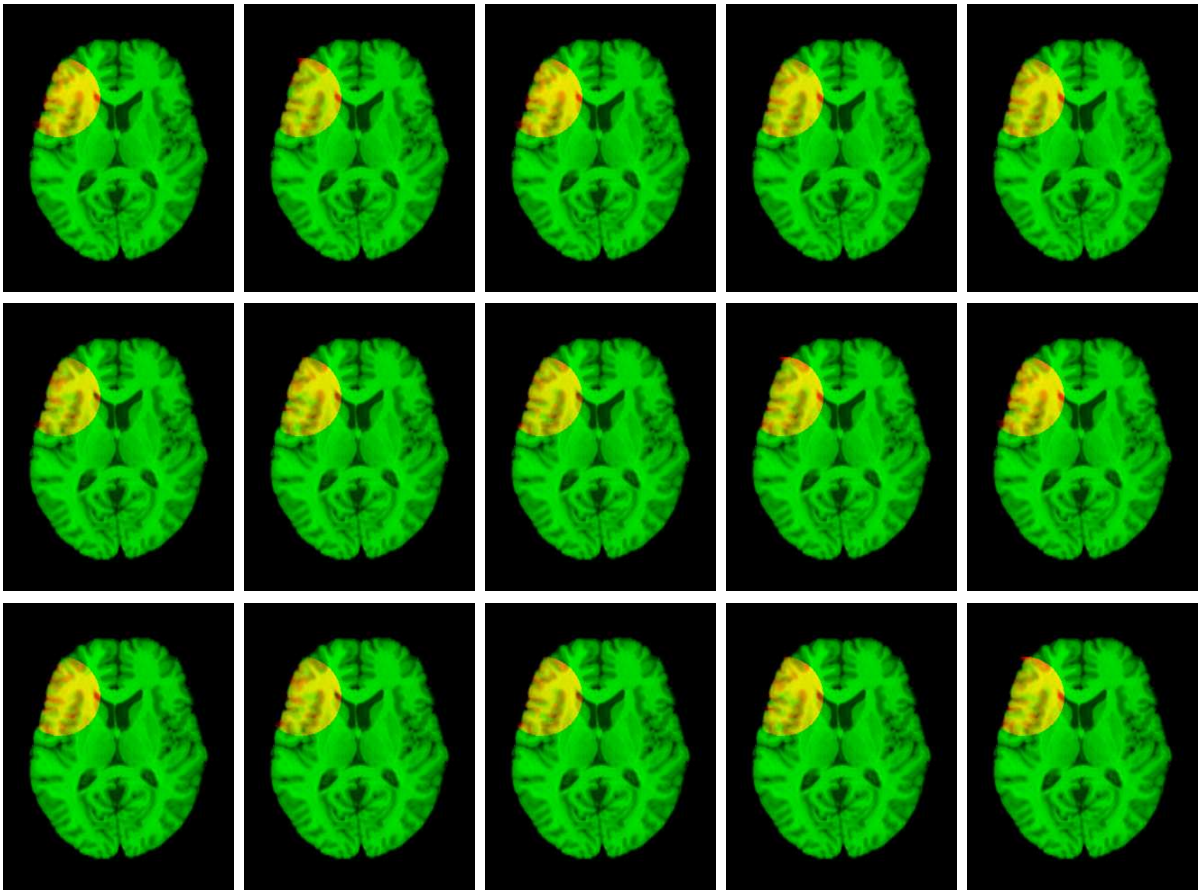

Figure 3.22: Transverse Slices of Registered Brain Image Registration Datasets using Spherical Envelope. The figure shows the same transverse slices (slice no. 147) for all datasets registered to dataset na01 using spherical envelope. The spherical envelope is computed dynamically using the segmentation boundary. The figure shows that while intensity matching is good towards interior of the sphere, the region closer to object boundaries does not match that well due to boundary conditions.

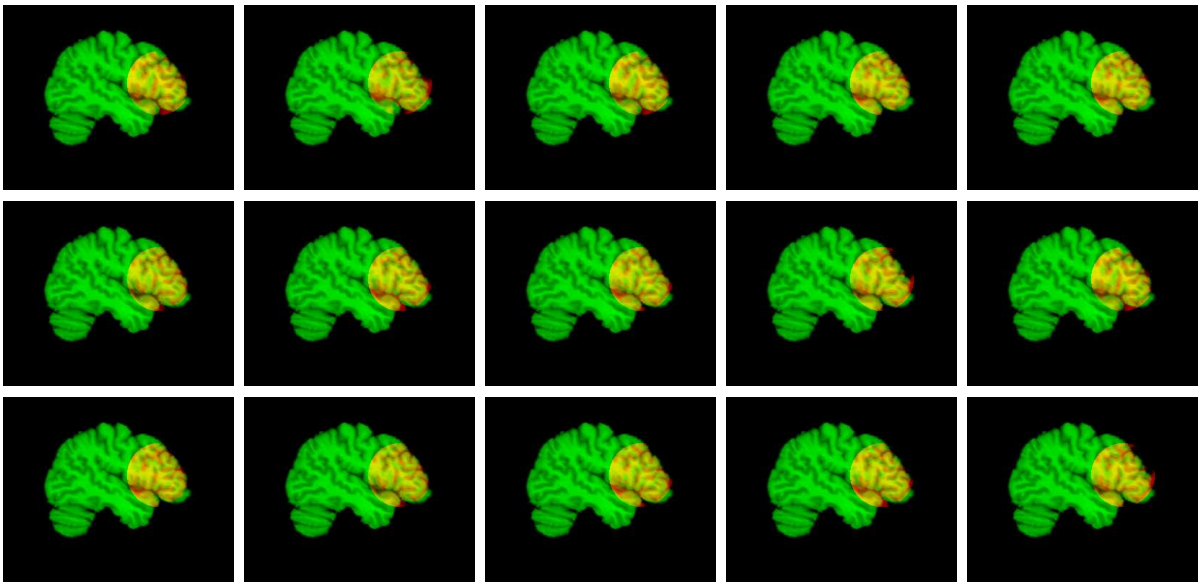

Figure 3.23: Sagittal Slices of Registered Brain Image Registration Datasets using Spherical Envelope. The figure shows the same sagittal slices (slice no. 63) for all datasets registered to dataset na01 using spherical envelope. The spherical envelope is computed dynamically using the segmentation boundary. The figure shows that while intensity matching is good towards interior of the sphere, the region closer to object boundaries does not match that well due to boundary conditions.

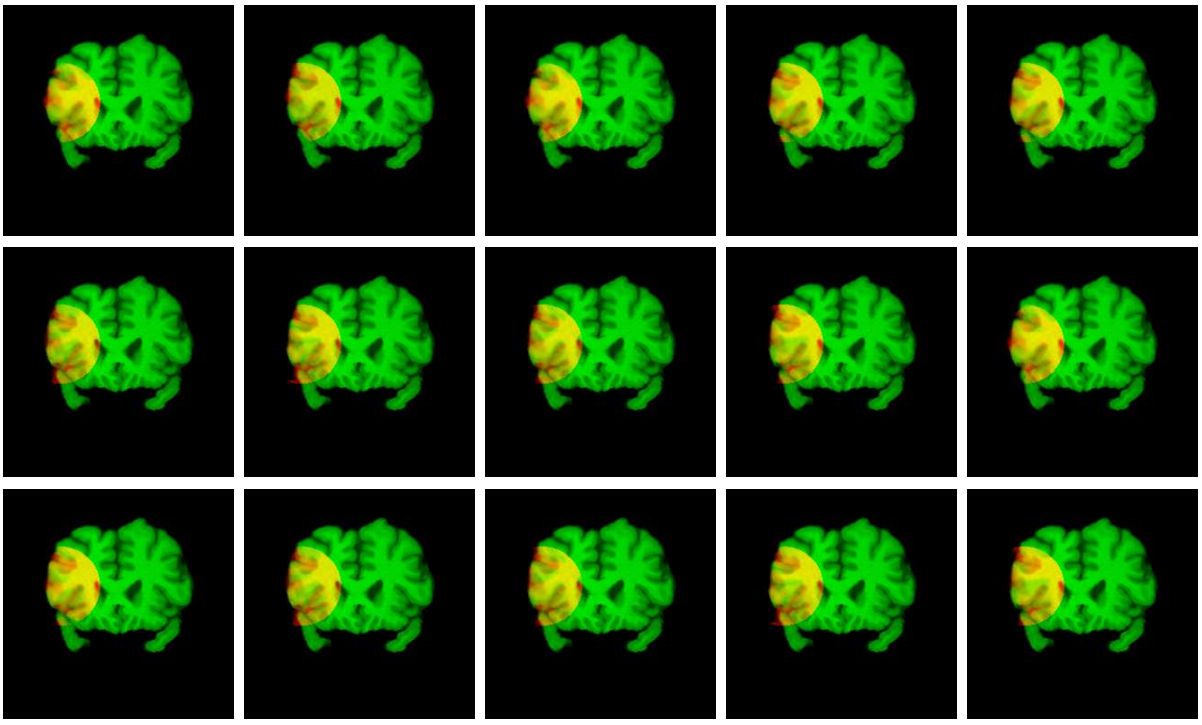

Figure 3.24: Coronal Slices of Registered Brain Image Registration Datasets using Spherical Envelope. The figure shows the same coronal slices (slice no. 214) for all datasets registered to dataset na01 using spherical envelope. The spherical envelope is computed dynamically using the segmentation boundary. The figure shows that while intensity matching is good towards interior of the sphere, the region closer to object boundaries does not match that well due to boundary conditions.

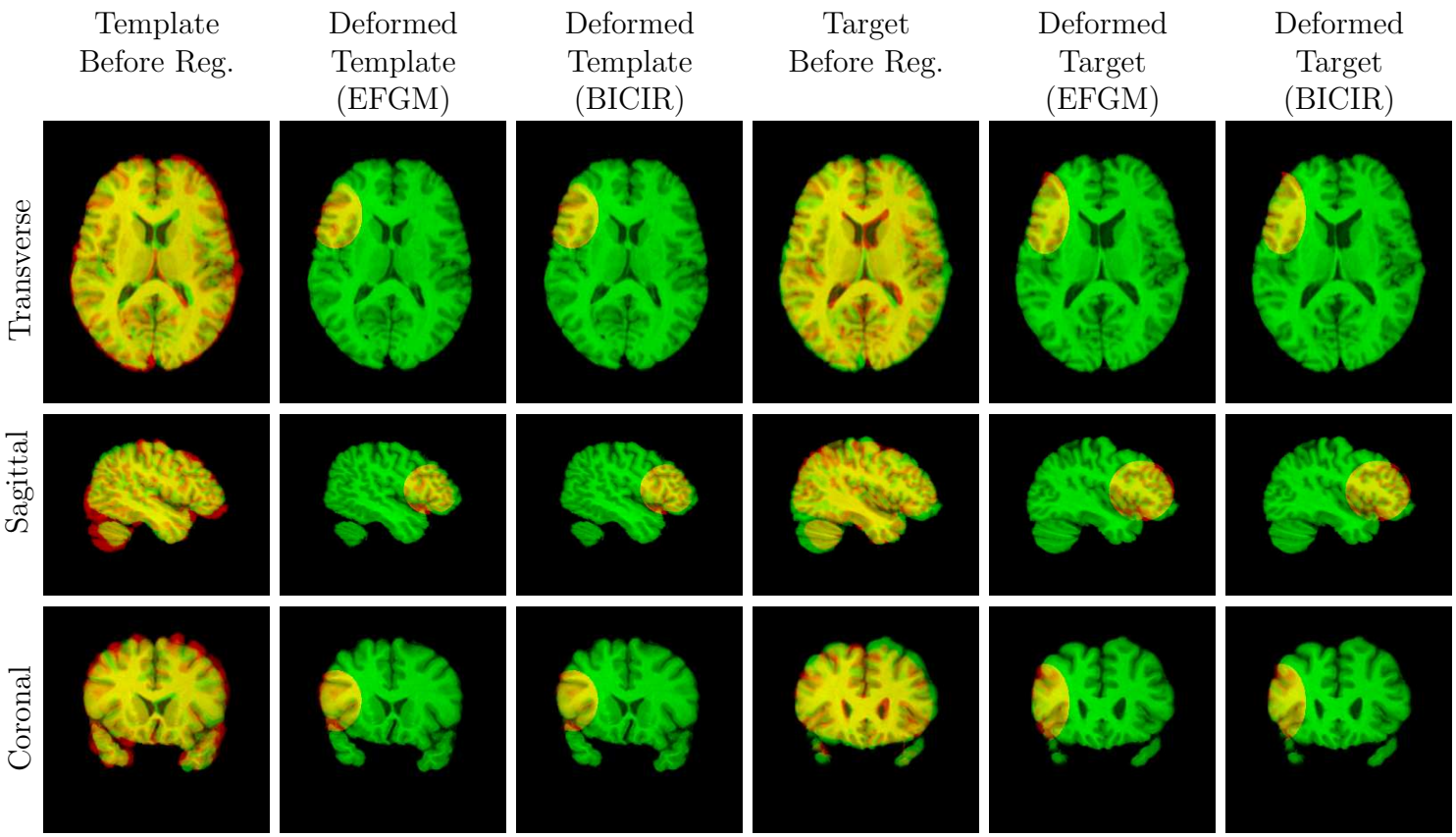

Figure 3.25: Results for a Pair of Image Registration between Two NIREP Brain Datasets using Ellipsoidal Envelope. The figure shows the forward and reverse image registration results for a pair of NIREP datasets. The first three columns show the original template image, deformed image after EFGM and deformed image after BICIR registration, respectively. The next three columns show the same results in reverse direction. The rows show from top to bottom: transverse, sagittal and coronal images.

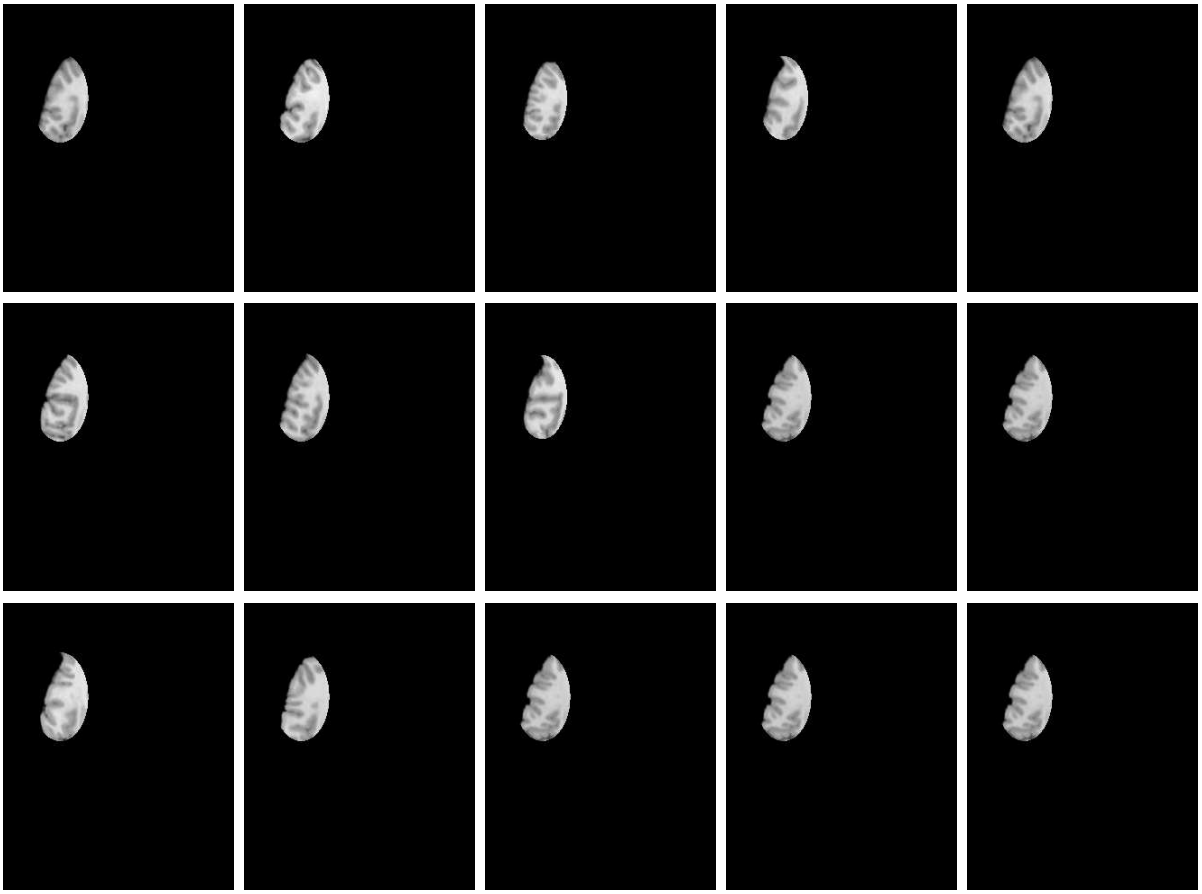

Figure 3.26: Transverse Slices of Registered Brain Image Registration Datasets using Ellipsoid Envelope. The figure shows the same transverse slices (slice no. 151) for all datasets registered to dataset na01 using spherical envelope. The spherical envelope is computed dynamically using the segmentation boundary. The figure shows that while intensity matching is good towards interior of the sphere, the region closer to object boundaries does not match that well due to boundary conditions.

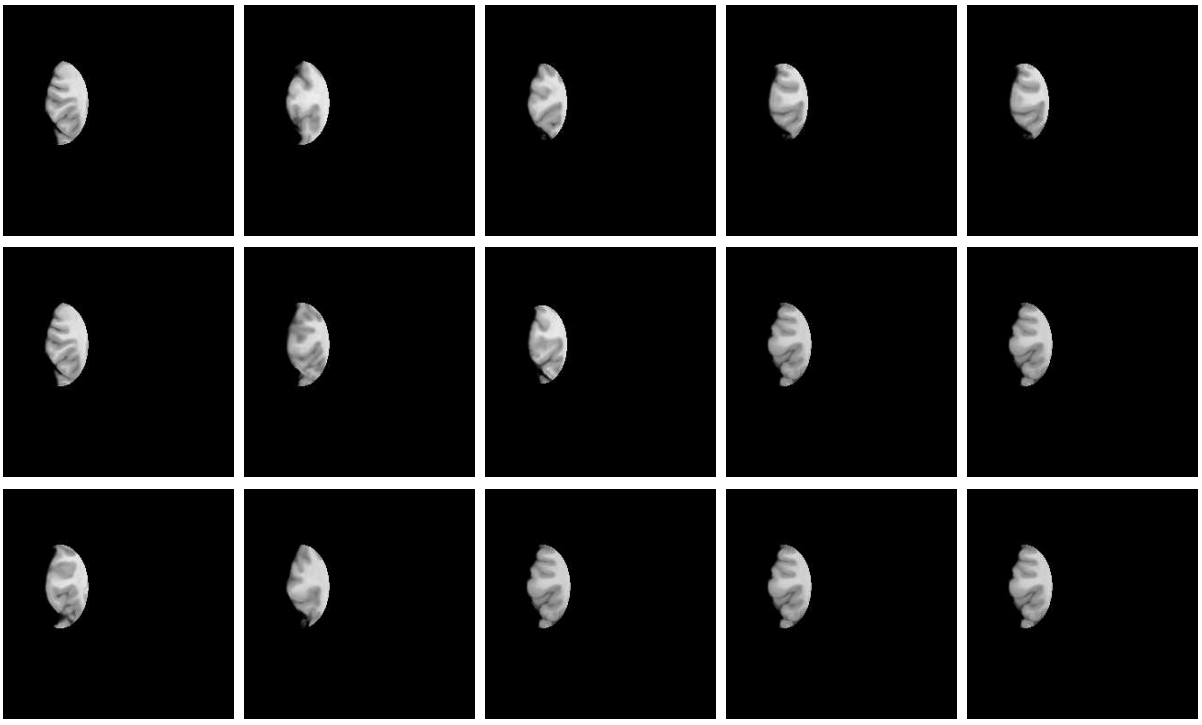

Figure 3.27: Coronal Slices of Registered Brain Image Registration Datasets using Ellipsoid Envelope. The figure shows the same coronal slices (slice no. 217) for all datasets registered to dataset na01 using spherical envelope. The ellipsoid envelope is computed dynamically using the segmentation boundary. The figure shows that while intensity matching is good towards interior of the ellipsoid, the region closer to object boundaries does not match that well due to boundary conditions.

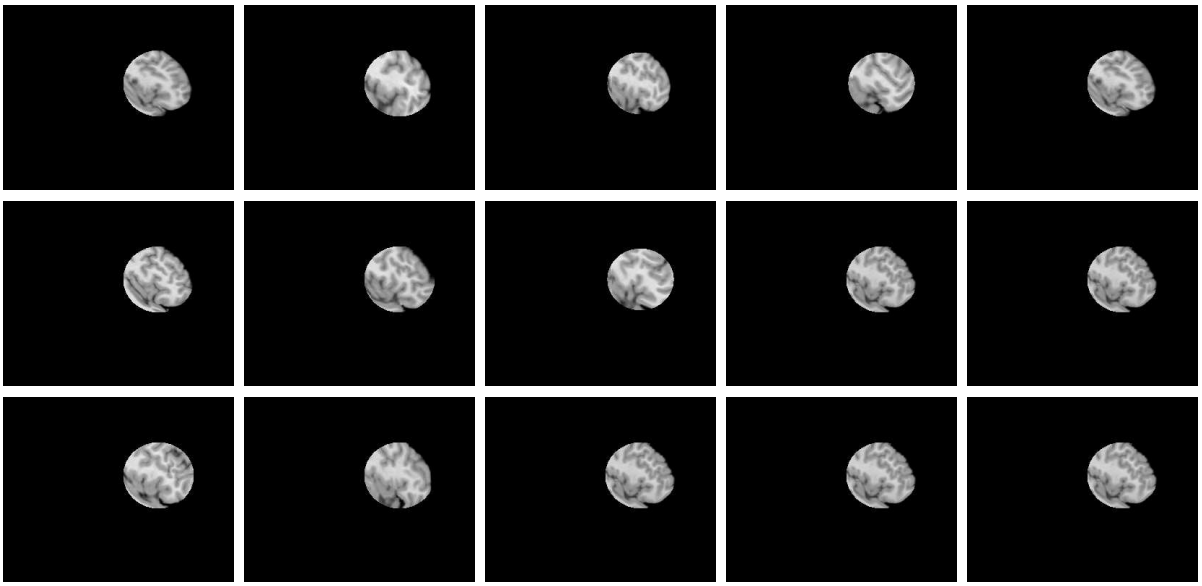

Figure 3.28: Sagittal Slices of Registered Brain Image Registration Datasets using Ellipsoid Envelope. The figure shows the same sagittal slices (slice no. 69) for all datasets registered to dataset na01 using spherical envelope. The ellipsoid envelope is computed dynamically using the segmentation boundary. The figure shows that while intensity matching is good towards interior of the sphere, the region closer to object boundaries does not match that well due to boundary conditions.

Performance Metric	Before Registration	SICLE	BICIR w/ Spherical Env	BICIR w/ Ellipsoid Env
	Ave. / Max / Std. Dev.	Ave. / Max / Std. Dev.	Ave. / Max / Std. Dev.	Ave. / Max / Std. Dev.
Ave. Int. Diff. (Gray Scale)	38.05/ 75.53/ 11.57	25.94/ 29.98/ 2.39	18.21/ 21.78/ 1.45	19.75/ 22.03/1.74
Ave. Relative Overlap (%)	24.63/ 31.0/ 4.9	32.91/ 37.8/ 2.24	35.139 / 38.74 / 2.3395	35.90/39.34/2.64
Average ICE (voxels)	-/ -/ -	0.039/0.048/0.005	0.049/ 0.086/ 0.01	0.06/0.084/0.009
Time Taken (seconds)	-/ -/ -	21.73/ 22.87/0.558	16.93/ 19.05/ 1.45	17.22/19.66/1.2

Table 3.6: Summary Performance Statistics for 15 3D brain ROI registrations.

3.2.5 Sensitivity Analysis

The quality of BICIR registration depends on the quality of the region of interest segmentation that the registration is performed over. The BICIR method is initialized by the correspondence of the boundary of the ROI. The boundary correspondence may be poor due to poor segmentation, poorly defined boundary conditions or a combination of these factors. The 3D anatomical data experiments attempted to address this problem by dilating the ROI segmentation. This section studies the sensitivity of the BICIR algorithm to segmentation error and poor boundary conditions. All experiments used a spherical ROI like the experiments presented in Section 3.2.3.1. The sensitivity of BICIR to segmentation error was measured by registering images repeatably using spherical ROIs with different radii. The sensitivity of BICIR to boundary correspondence error was measured by registering images in which the spherical ROI was translated in the x, y and z directions.

3.2.5.1 Sensitivity to ROI Size

To test the sensitivity of BICIR to the ROI size, we selected a corresponding region of brain cortex for a pair of brain images. The tightest fit sphere that contained the ROI was computed for both, template and target images, respectively. The radii value for the template and target images were 35.17 voxels and 44.15 voxels, respectively. The spheres defined the ROI in which the registration was performed. The radius of template image was varied from 0.5 to 1.5 times the radius of the tightest fit sphere in increments of 0.1 while the radius of target ROI was kept fixed. The experiment was repeated by keeping radius of template ROI fixed while radius

for the target ROI was varied from 0.5 to 1.5 times the radius of sphere of tightest fit in target image. This set up studies the sensitivity to ROI size and difference in scale between the template and target regions. Figure 3.29 shows the results of these experiments. The three charts show similarity cost, average inverse consistency error and relative overlap as a function of magnitude of the radius. The results for forward and reverse transformations are represented together for each radius value.

This figure shows that the minimum similarity cost and average ICE were centered about the scaling factor of 1.1. However the maximum relative overlap was achieved with the scale factor of 1.0 The results within 10% of this scaling factor, i.e., results from 0.9 to 1.1 provide comparable registration results within 5% of the cost. However, as we move away from these values, the errors become very high and registration results become poor.

The next experiment was designed to evaluate the sensitivity of BICIR to the dilation of ROI. Dilating the ROI provides the BICIR algorithm a larger volume for intensity registration and reduces the impact of correspondence errors at the boundary of the registration ROI. For this experiment, the spheres corresponding to template and target ROIs were scaled using the same factor simultaneously. The scaling factor was changed from 0.5 to 1.5 in intervals of 0.1, respectively. A total of 11 registrations were performed and forward and reverse results were combined together. Figure 3.30 shows the results for these registrations.

Figure 3.30 shows that if ROI is reduced from the tightest fit sphere, all the costs increase. As we dilate, the costs reduce and better registration is achieved. The

method provides very small inverse consistency errors for all values of dilation factors. We see a saturation in registration quality as we increase the radius of sphere. The registration continues to improve significantly with increase in dilation factor from 1.0 to 1.2 as the average intensity differences, average inverse consistency error and relative overlap continue to improve by more than 5%. After dilation factor of 1.2, the results improve only slightly and from 1.2 to 1.5, the average intensity difference and average relative overlap stay within 5% of the cost at dilation factor of 1.2. The inverse consistency error stays under 0.05 for these cases. While marginal improvement in registration quality may continue, the last chart in figure shows that this comes at the cost of increased time needed for registration owing to larger ROI for larger dilation factors.

3.2.5.2 Sensitivity to Boundary Correspondence Error

The BICIR method assumes that the boundary correspondences are defined perfectly and does not update the boundary correspondence. In this section, we analyze the impact of poor boundary conditions. The boundary correspondence error was simulated using translation of the sphere in x, y and z directions, respectively. Translation was applied as a fraction of the radius of the tights fit sphere in template and target images. The sensitivity was studied by applying translations to the template ROI, which had a radius of 35.75 voxels. The entire sphere was translated by 0.1, 0.2 and 0.5 times the radius of the tightest fit sphere. Registration was performed for translations in in all three directions in both, positive and negative directions, which resulted in a total of 18 registrations.

Figrure 3.31 shows the results for sensitivity of registration w.r.t. the magnitude of translational error in boundary correspondences. The figure shows that the costs are lower and relative overlap is higher for small translation errors with central value of zero translation providing smallest cost and largest relative overlap. The average intensity difference, relative overlap and average ICE stayed within 5% of the central value for translation of 0.1 in positive direction and within 10% for translation of 0.1 in negative direction, respectively. As we apply translation of 0.2 times the radius, the average intensity difference and average ICE increase by more than 15% while the relative overlap reduces by more than 15% in both, positive and negative directions, respectively. For larger translation of 0.5 times the radius, the average intensity difference and average ICE become very high and relative overlap drops to 50% of the highest value. The plot shows that for translations larger than 0.2 times the radius, the overall registration suffers and is unusable.

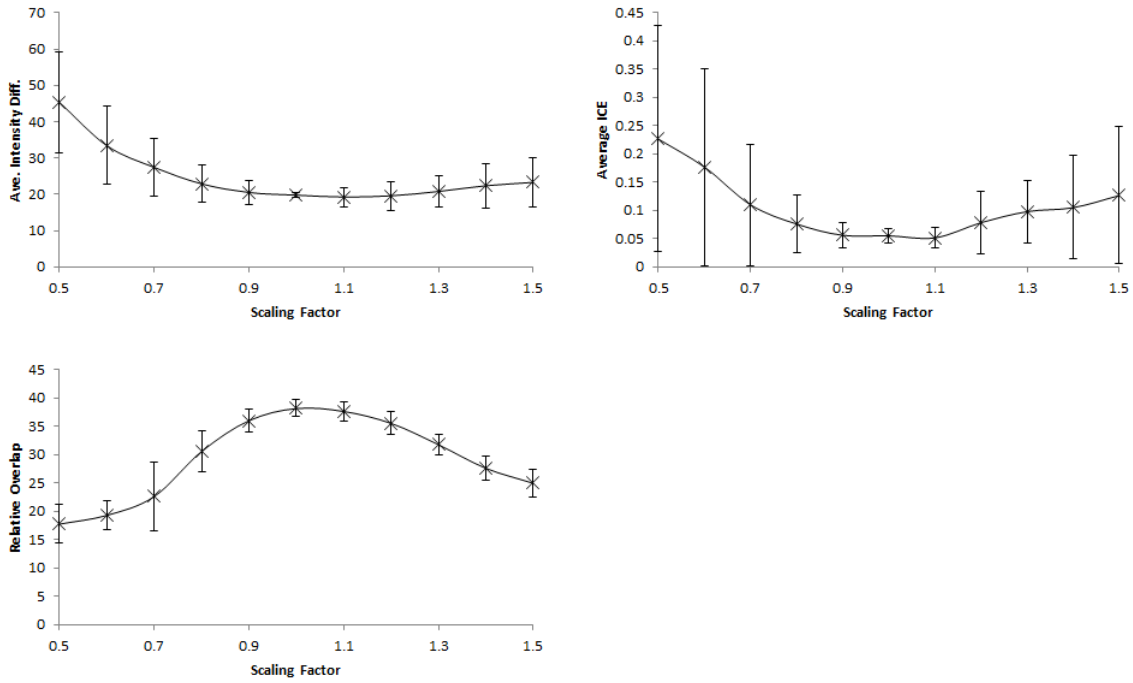

Figure 3.29: Sensitivity with respect to the size of ROI when the radius of ROI is changed in one image. Top row (from Left to Right): Plot showing sensitivity of similarity cost w.r.t. scaling factor used to scale either template or target image, respectively, plot showing sensitivity of average ICE w.r.t. scaling factor. Bottom row: Plot showing sensitivity of relative overlap of the segmentation w.r.t to the scaling factor in boundary correspondence. The scaling was applied only to one image at a time. This provided a total of 21 registrations. The forward and reverse registration results were combined together to provide the above plots. The cross at the center at each sample value represents the average and the upper and lower bars at each vertical line represent one standard deviation from the average.

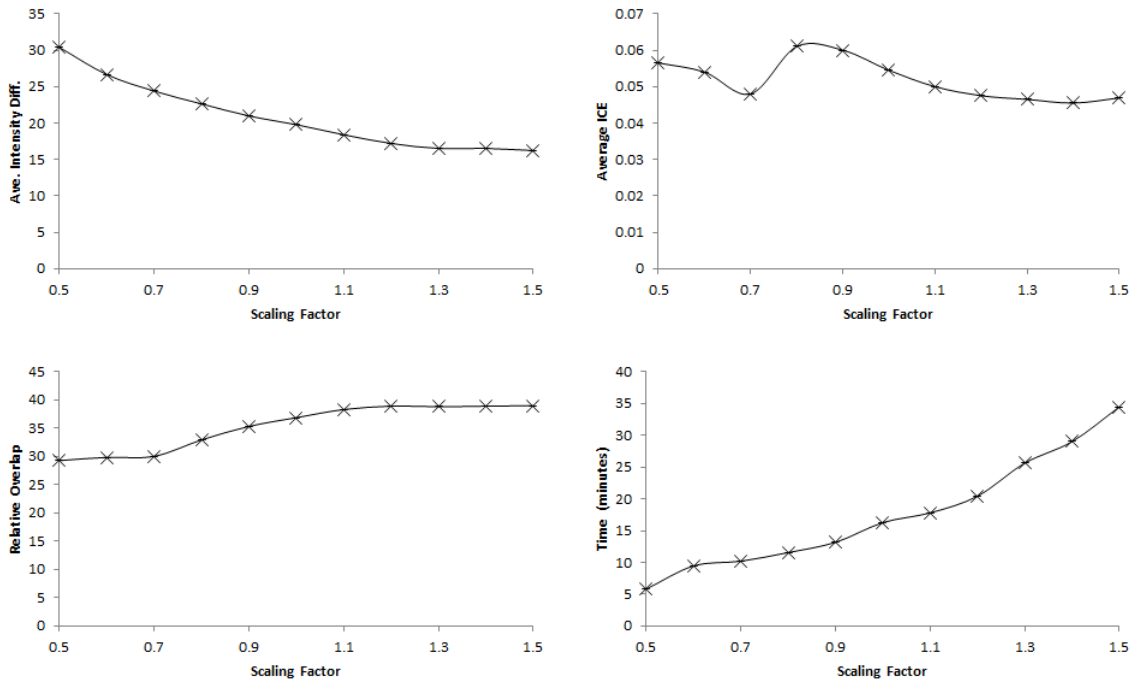

Figure 3.30: Sensitivity with respect to the size of ROI when the radius of ROI is changed in both image. Top row (from Left to Right): Plot showing sensitivity of similarity cost w.r.t. dilation factor used to scale both, template and target images, respectively, plot showing sensitivity of average ICE w.r.t. dilation factor. Bottom row (from left to right): Plot showing sensitivity of relative overlap of the segmentation w.r.t to dilation factor in boundary correspondence, plot showing time plotted against the dilation factor. The dilation factor is expressed as a fraction of the radius of the corresponding ROI. The results represent a total of 11 registrations. The forward and reverse registration results were averaged to get a single point at each dilation value. The cross at the center at each sample value represents the average and the upper and lower bars at each vertical line represent one standard deviation from the average.

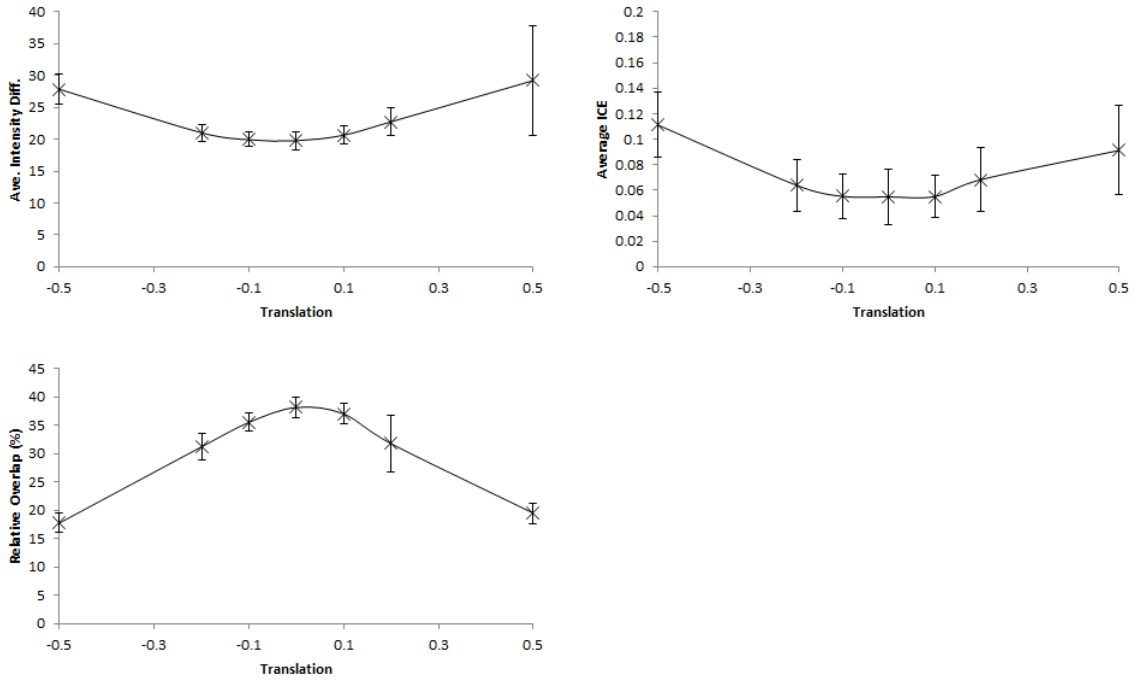

Figure 3.31: Sensitivity to Boundary Correspondence Error. Top row (from Left to Right): Plot showing sensitivity of similarity cost w.r.t. magnitude of translation error in boundary correspondences, plot showing sensitivity of average ICE w.r.t. magnitude of translation error in boundary correspondence. Bottom row: Plot showing sensitivity of relative overlap of the segmentation w.r.t to magnitude of translation error in boundary correspondence. The translation error is expressed as a fraction of the radius of the corresponding ROI. The results represent averages over a total of 18 registrations with various combinations of perturbations in x, y and z directions. The cross at the center at each sample value represents the average and the upper and lower bars at each vertical line represent one standard deviation from the average.

This chapter showed the analysis and application of BICIR registration method under various scenarios. First, phantom 2D images were used to analyze the method and then anatomical 2D images were registered and compared against SICLE registration method. The comparison showed that the BICIR registration method provided improved results. We proceeded with phantom 3D images to test extension of BICIR registration method to 3D. 3D anatomical images were subsequently used. First, an inverse consistent method was used to get a boundary correspondence as an input to BICIR method. This was done to test response of BICIR method to a consistent boundary input in absence of a suitable 3D surface or boundary registration method. Finally, the algorithm was demonstrated over arbitrarily shaped regions, which were kept parametric for ease in computing boundary correspondence for ROIs. This shows that the BICIR method is flexible and can be used to perform registration over a small object inside an image using boundary input, while it performs well under an integrated framework using parametric shapes as well.

CHAPTER 4
DISCUSSIONS AND CONCLUSIONS

4.1 Discussions

The dissertation presents a novel technique called Boundary-constrained Inverse Consistent Image Registration (BICIR) to register a pair of images while keeping correspondence at boundaries of a region of interest (ROI) containing an object of interest fixed. The method was studied and evaluated for 2-D phantom images, 3-D phantom images and 3-D brain images. The experimental setup included a variety of input shape types, from 2D parametric shapes to 3D parameteric shape and 3D non-parametric shapes with non-parametric irregular boundaries. Finally, an integrated framework with a parametric envelope was presented.

The BICIR method uses boundary correspondence as an input and thus the boundaries of the two ROIs need to be registered prior to using BICIR. For the examples studied in this work, different methods were used for computing the boundary correspondence. For paramteric 2D and 3D ROIs, the boundaries were computed analytically and a perfect boundary match that is also inverse consistent can thus be provided as an input. For irregular 2D (lungs) and 3D (brains) shapes, however, boundary correspondence were estimated using inverse consistent contour registration method for 2D lungs and using SICLE registration method for registering mask images for 3D brain shapes, respectively.

The results were presented for analysis and characterization of Boundary con-

strained inverse consistent image registration (BICIR). The method was shown to match object boundaries based on the input correspondence, which are kept fixed while registering the region inside the object using intensity information. The method performance was demonstrated over a range of input shapes such as parametric ellipsoids and cuboids as well as non-parametric shapes such as brain images.

Comparison was made against existing small deformation inverse consistent linear elastic image registration method and BICIR was shown to improve boundary correspondences and overall intensity based similarity, while maintaining a comparable inverse consistency error.

Although the BICIR method was shown to be superior to SICLE for the presented cases, BICIR suffers from sensitivity to poorly defined boundary correspondences as it does not evaluate or update the boundary correspondence provided as input. Once the boundary correspondence is established, BICIR keeps it fixed regardless of the intensity information inside the region of interest.

Figure 4.1 provides an example of limitation of BICIR when the boundary condition is not specified accurately at the input. The figure shows an example for registration between a pair of circles of same size and at same location. Each circle is divided into two semi-circles with corresponding intensities of 255 and 128, respectively. The template image contains the semicircles such that the dividing line is vertical while the target image has the dividing line at an angle of 15 degrees counterclockwise from vertical. As a result, the boundaries of the ROIs representing the two circles overlap exactly with each other but the boundary correspondence

should take the rotation into account. For this example, the boundary conditions were specified as identity such that while the ROIs bounded by boundary of the circle overlap exactly, the interior does not match and the correspondence is wrong at the boundaries. The results seen in third and fourth columns of the top row illustrate that even though BICIR minimizes intensity difference inside the object, the boundaries stay unchanged. As a result, the interior of the template deforms while following regularization constraints and the boundaries remain locked at the initial position. This results in an apparent swirl in the image as the correspondence improves as we move into the object and away from the boundaries. This leads to the conjecture that if the interior intensity values are allowed to alter the boundary correspondence along the boundaries, the overall registration can improve.

The second row presents similar results for the registration in opposite direction, i.e. from target to template image. The findings are consistent with the results in forward direction. The third and fourth row represent the x- and y-displacement fields, inverse consistency error and jocobian in forward and reverse directions, respectively. The images show that the deformation is limited to a small region inside the object and largest deformation occurs at the location of intensity difference between the two images away from boundaries. Figure also shows that the forward and reverse transformations appear to be inverses of each other with larger Jacobian values (brighter intensities) in one direction corresponding to smaller Jacobian values (darker intensities) in the opposite direction and vice versa. The same effect can be seen in the x-displacement and y-displacement images.

The example shows an important limitation of method and solution to this problem lies in using intensity information from the intensity registration phase to update boundary correspondence, thus using feedback from intensity inside ROI. As a result, BICIR's results can be expected to improve by incorporating intensity feedback for updating the boundary correpondences.

Another important addition that could improve results further is inclusion of internal landmark or region correspondences. Without this information, BICIR method equates to SICLE registration method with the advantage of regions already matched such that registration can be performed inside any arbitrarily defined "window". The correspondence at boundaries of this window stays unchanged while the interior deforms to match the image intensities following the regularization constraints inside this "window". To achieve further refinement at the interior, if some correspondences inside is known, it may be possible to improve BICIR method further.

The WEB-splines are defined in the image space. Therefore any landmark correspondence can directly be taken into account by adding a cost term corresponding to landmark matching error to the overall cost function. BICIR method can then simultaneously minimize the intensity differences as well as landmark matching error. The landmark correspondence may further be extended to matching of corresponding regions. This will require corresponding regions and their boundary correspondences to be identified between a pair of images such that these regions are contained inside an outer region representing the entire object to be registered. One of the approaches that may be taken could be that initial boundaries include all the correspondences,

i.e., outer object boundaries as well as boundaries or locations of all the matched regions or landmarks inside the ROI. This will result in a WEB-spline basis function such that the basis function values drop to zero at these locations. There is, however, limitation on how close these boundaries can be allowed to be. If the support of basis function is too narrow, it could result in over-sensitive and unstable behavior. Such a problem may be solved by adjusting the knot spacing accordingly such that the basis function is always well defined on a fine grid for the updated ROI.

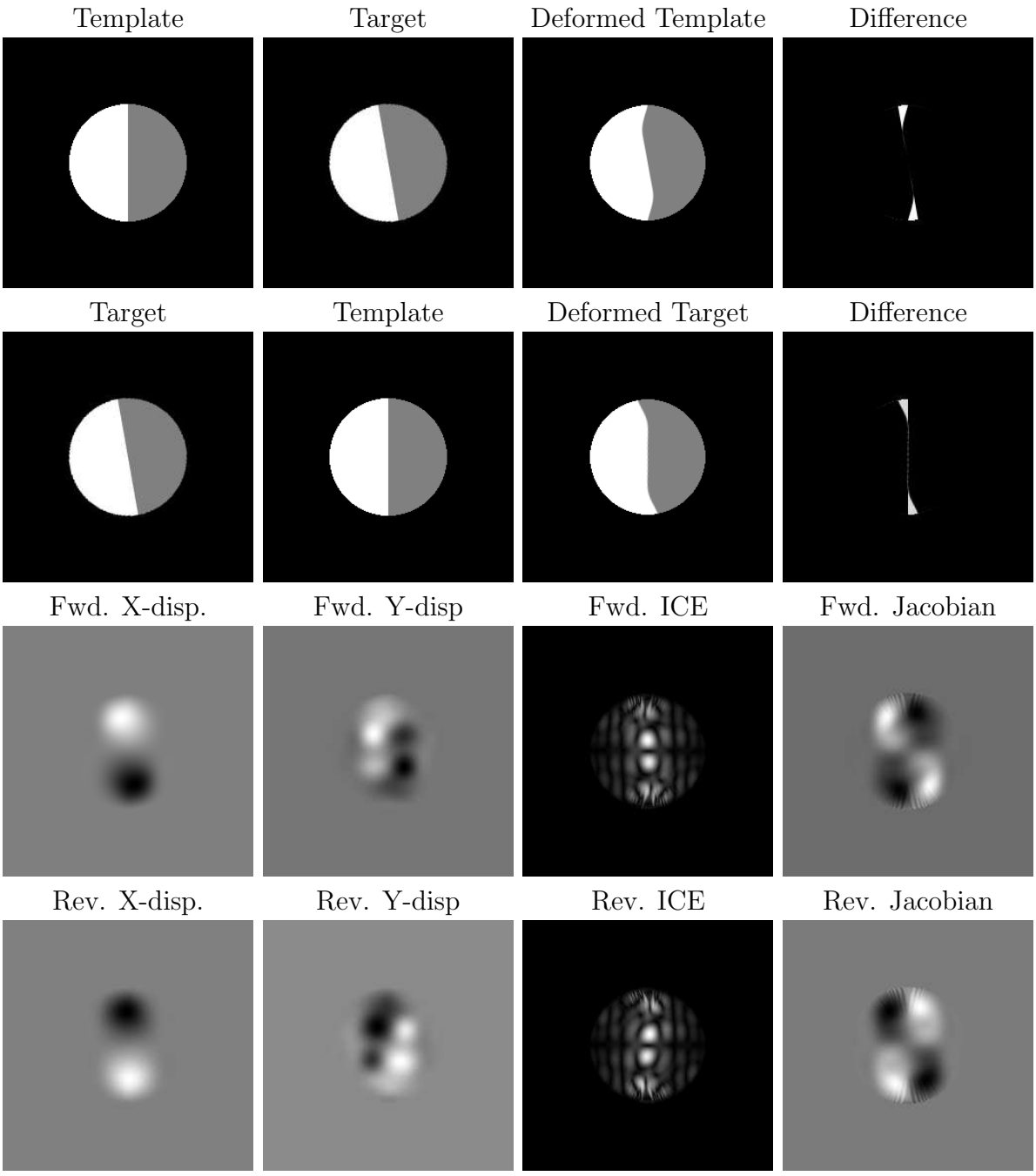

Figure 4.1: Example of Boundary Problem involving rotation. The first panel shows the template image and the second panel shows the target image. The target image has exactly same boundaries as the template image, but the interior is different. The figure shows that the web-spline basis can not incorporate rotation as their support falls to zero on boundaries. The Maximum Inverse Consistency Error in the ICE image was 0.25 of the size of a pixel.

4.2 Conclusions

A new image registration method called Boundary-constrained Inverse Consistent Image Registration (BICIR) was presented. The method was shown to minimize residual intensity differences between two images being registered together after the shape differences have been minimized. The method uses boundary correspondences to first interpolate the correspondence inside the object/ region of interest (ROI). The correspondence inside the ROI is then updated using the intensity information. Linear elastic and inverse-consistent regularization constraints were applied to constrain the registration. The method was tested and evaluated over a variety of test images and ROI shapes. The test images included parametric and non-parametric 2D and 3D objects. The ROI shapes included parametric and non-parametric shapes. The parametric objects and ROIs included ellipses and lungs (2D) and ellipsoids, cuboids and brains (3D). The method was characterized with respect to weight of different components in multi-variate cost function and with respect to resolution of basis function. The method was shown to match boundaries exactly and match intensities well inside a given ROI well while maintaining very low inverse consistency errors within ROI (of the order of 0.01 to 0.1 voxels). The progressive refinement of the grid was shown to improve registration results as addition of more degrees of freedom resulted in decrease in inverse consistency error and improved registration locally.

The presented work in this thesis ends with an integrated framework where boundary correspondence was computed during the registration and was not required at the input. Three different methods for establishing boundary correspondence were

studied and compared against each other as well as against small-deformation inverse consistent linear elastic (SICLE) image registration method. The methods were shown to be superior to and faster than SICLE registration method using various error metrics for a small ROI defined inside the 3D MR image. We feel that the method can be further improved by incorporating the intensity feedback for updating or confirming the boundary correspondences. In addition, the method may be easily extended to include internal correspondences as boundary conditions.

REFERENCES

[1] P.J. Besl and N.D. McKay. A method for registration of 3-d shapes. *IEEE Trans. Pattern Anal. and Machine Intelligence*, 14(2):239–256, 1992.

[2] F.L. Bookstein. Principal warps: Thin-plate splines and the decomposition of deformations. *IEEE Transaction on Pattern Analysis and Machine Intelligence*, 11:567–585, 1989.

[3] G.E. Christensen. Inverse consistent registration with object boundary constraints. In *Proceedings of the 2004 IEEE International Symposium on Biomedical Imaging: From Nano to Macro*, Arlington, VA, USA, April 2004. IEEE.

[4] G.E. Christensen and H.J. Johnson. Consistent image registration. *IEEE Trans. Med. Imaging*, 20(7):568–582, July 2001.

[5] G.E. Christensen, J.H. Song, I.E. Naqa, W. Lu, and D.A. Low. Tracking lung motion: Correlating inverse consistent image registration and spirometry. In *Proceedings of the 14th International Conference on the Use of Computers in Radiation Therapy*, pages 493–496, Seoul, Korea, May 9-14, 2004.

[6] H. Chui and A. Rangarajan. A new point matching algorithm for non-rigid registration. *Computer Vision and Image Understanding*, 89:114–141, 2003.

[7] Haili Chui and Anand Rangarajan. A new algorithm for non-rigid point matching. In *CVPR 2000*, pages 44–51, 2000.

[8] T.F. Cootes, C.J. Taylor, D.H. Cooper, and J. Graham. Active shape models—their training and application. *Computer Vision and Image Understanding*, 61(1):38–59, 1995.

[9] Lawrence Dougherty, Drew A. Torigian, John D. Affuso, Jane C. Asmuth, and Warren B. Gefter. Use of an optical flow method for the analysis of serial ct lung images. *Academic Radiology*, 13(1):14–23, 2006.

[10] Li Fan, Chang Wen Chen, Joseph M. Reinhardt, and Eric A. Hoffman. Evaluation and application of 3d lung warping and registration model using hrct images. Proc. SPIE Conf. Medical Imaging, pages 17–22, Feb. 2001.

[11] J. Gee and D. Haynor. Numerical methods for high dimensional warps. In

A. Toga, editor, *Brain Warping*, pages 101–113. Academic Press, San Diego, 1999.

[12] James Gee, Tessa Sundaram, Ichiro Hasegawa, Hidemasa Uematsu, and Hiroto Hatabu. Characterization of regional pulmonary mechanics from serial magnetic resonance imaging data. *Academic Radiology*, 10(10):1147–1152, 2003.

[13] Xiujuan Geng, Dinesh Kumar, and Gary E. Christensen. Transitive inverse-consistent manifold registration. In Gary E. Christensen and Milan Sonka, editors, *Information Processing in Medical Imaging*, volume LNCS 3564, pages 468–479, Berlin, July 2005. Springer-Verlag.

[14] Steven Gold, Anand Rangarajan, Chien-Ping Lu, Suguna Pappu, and Eric Mjolsness. New algorithms for 2d and 3d point matching: Pose estimation and correspondence. *Pattern Recognition*, 31:1019–1031, 1998.

[15] H. Haneishi, N. Takita, D. Tsuchida, Y. Mori, H. Toyama, and T. Miyamoto. Image registration between ct, spect and dose map images of lung and its application to image analysis in radiation therapy. 4:2946–2950, December 2003.

[16] Jianchun He. *Large Deformation Consistent Elastic Image Registration*. PhD thesis, Department of Electrical and Computer Engineering, The University of Iowa, Iowa City, IA 52242, May 2003.

[17] Klaus Höllig. Finite Element Methods with B-Splines . *Society for Industrial and Applied Mathematics*, 2003.

[18] Klaus Höllig and Ulrich Reif. Nonuniform Web-Splines . *Computer Aided Geometric Design*, 20:277–294, 2003.

[19] Klaus Höllig, Ulrich Reif, and Joachim Wipper. Weighted Extended B-Spline Approximation of Dirichlet Problems. *SIAM J. Numer. Anal.*, 39(2):442–462, 2001.

[20] L. Hsu, R. Kusner, and J. Sullivan. Minimizing the squared mean curvature integral for surfaces in space forms. *Experiment. Math.*, 1(3):191–207, 1992.

[21] H.J. Johnson and G.E. Christensen. Consistent landmark and intensity-based image registration. *IEEE Trans. Med. Imaging*, 21(5):450–461, 2002.

[22] Anand A. Joshi, David W. Shattuck, Paul M. Thompson, and Richard M. Leahy. Cortical surface parameterization by p-harmonic energy minimization. In *ISBI*, pages 428–431, 2004.

[23] Anand A. Joshi, David W. Shattuck, Paul M. Thompson, and Richard M. Leahy. A framework for registration, statistical characterization and classi cation of cortically constrained functional imaging data. In Gary E. Christensen and Milan Sonka, editors, *Information Processing in Medical Imaging*, Berlin, July 2005. Springer-Verlag.

[24] P. Keall. 4-dimensional computed tomography imaging and treatment planning. *Seminars in Radiation Oncology*, 14(1):81–90, 2004.

[25] J. Kybic. *Elastic Image Registration Using Parametric Deformation Models*. PhD thesis, Swiss Federal Institute of Technology Lausanne, EPFL, Lausanne, Switzerland, 2001.

[26] Jan Kybic, Philippe Thevenaz, Arto Nirkko, and Michaek Unser. Unwarping of unidirectionally distorted epi images. *IEEE Transactions on Medical Imaging*, 19(2):80–93, February 2000.

[27] Jan Kybic and Michael Unser. Fast parametric elastic image registration. *IEEE Transactions on Image Processing*, 12(11):1427–1442, November 2003.

[28] Baojun Li. *The Construction of a Normative Human Lung Atlas by Inter-Subject Registration and Warping of CT Images*. PhD thesis, The University of Iowa, Iowa City, IA, 52242, 2004.

[29] Baojun Li, Gary E. Christensen, John Dill, Eric A. Hoffman, and Joseph M. Reinhardt. 3-D inter-subject warping and registration of pulmonary CT images for a human lung model. In A.V. Clough and C.T. Chen, editors, *Medical Imaging 2002: Physiology and Function from Multidimensional Images*, volume Proceedings of SPIE Vol. 4683, pages 324–335, San Diego, CA, 23-28 Feb. 2002.

[30] Baojun Li, Gary E. Christensen, Geoffrey McLennan, Eric A. Hoffman, and Joseph M. Reinhardt. Establishing a normative atlas of the human lung: Inter-subject warping and registration of volumetric CT. *Academic Radiology*, 10(3):255–265, March 2003.

[31] Baojun Li and Joseph M. Reinhardt. Automatic generation of object shape models and their application to tomographic image sequence. In *Proc. SPIE Conf. Medical Imaging*, volume 4322, pages 311–322, San Diego, CA, 17-22 Feb. 2001.

[32] B. Likar and F. Pernuš. A hierachical approach to elastic registration based on mutual information. *Image and Vision Computing*, 19:33–44, 2001.

[33] F. Maes, A. Collignon, D. Vandermeulen, G. Marchal, and P. Suetens. Multimodality image registration by maximization of mutual information. *IEEE Transactions on Medical Imaging*, 16(2):187–198, April 1997.

[34] Frederik Maes, Dirk Vandermeulen, and Paul Suetens. Medical image registration using mutual information. *Proceedings of IEEE*, 91(10):1699–1722, October 2003.

[35] R. Timothy Marler. *A Study of Multi-Objective Optimization Method for Engineering Applications*. Ph.D. Dissertation of The University of Iowa, Iowa City, IA, 2005.

[36] D. Mattes, D.R. Haynor, H. Vesselle, T.K. Lewellen, and W. Eubank. Pet-ct image registration in the chest using free-form deformations. *IEEE Transactions on Medical Imaging*, 22(1):120–128, Jan. 2003.

[37] C.R. Maurer, R. Qi, and V. Raghavan. A Linear Time Algorithm for Computing Exact Euclidean Distance Transforms of Binary Images in Arbitrary Dimensions. *IEEE Trans. Pattern Anal. and Machine Intelligence*, 25(2):265–270, Feb. 2003.

[38] Theophano Mitsa and Jiang Qian. Image registration using elastic contours and internal landmarks. In *IEEE Instrumentation and Measurement Technology Conference*, pages 451–455, May 1998.

[39] B. Nayroles, G. Touzot, and P. Villon. Generalizing the finite element method: Diffuse approximation and diffuse elements. volume 10, pages 307–318. 1992.

[40] Andrzej Osyczka. Multicriterion optimization in engineering. *Ellis Horwood Limited*, 1984.

[41] Yan Pan, Dinesh Kumar, Eric A. Hoffman, Eric A. Hoffman, Gary E. Christensen, Geoffrey McLennan, Joo Hyun Song, Alan Ross, Brett A. Simon, and Joseph M. Reinhardt. Regional lung expansion via 3d image registration. In *Proc. SPIE Conf. Medical Imaging*, volume 5746, pages 453–464, Feb. 2005.

[42] J.P.W. Pluim, J.B.A. Maintz, and M.A. Viergever. Mutual-information-based registration of medical images: a survey. *IEEE Transactions on Medical Imaging*, 22(8):986–1004, 2003.

[43] Jiang Qian, Theophano Mitsa, and E.A. Hoffman. A physically based model for the registration of a 2d image sequence. In *Proc. of IEEE Int. Conference on ASSP*, pages 2195–2198, May 1996.

[44] K. Rohr, M. Fornefett, and H.S. Stiehl. Approximating thin-plate splines for elastic registration: Integration of landmark errors and orientation attributes. In A. Kuba and M. Samal, editors, *Information Processing in Medical Imaging*, LCNS 1613, pages 252–265, Berlin, June 1999. Springer-Verlag.

[45] K. Rohr, M. Fornefett, and H.S. Stiehl. Spline-based elastic image registration: integration of landmark errors and orientation attributes. *Computer Vision and Image Understanding*, 90:153–168, 2003.

[46] K. Rohr, H.S. Stiehl, R. Sprengel, T.M. Buzug, J. Weese, and M. H. Kuhn. Landmark-based elastic registration using approximating thin-plate splines. *IEEE Transactions on Medical Imaging*, 20(6):526–534, June 2001.

[47] Karl Rohr. Fundamental limits in 3d landmark localization. In *Proc. 19th Internat. Conf. on Information Processing in Medical Imaging (IPMI'05)*, pages 286–298, Colorado, USA, 2005.

[48] D. Rueckert, L.I. Sonoda, C. Hayes, D.L.G. Hill, M.O. Leach, and D.J. Hawkes. Nonrigid registration using free-form deformations: application to breast mr images. *IEEE Transactions on Medical Imaging*, 18(8):712–721, 1999.

[49] V. L. Rvachev, T. I. Sheiko, V. Shapiro, and I. Tsukanov. On Completeness of RFM solution structures. *Comp. Mech.*, 25:305–316, 2000.

[50] V. L. Rvachev, T. I. Sheiko, V. Shapiro, and I. Tsukanov. Transfinite interpolation over implicitly defined sets. *Comput. Aided Geom. Design*, 18:195–220, 2001.

[51] T.L. Saaty. A scaling method for priorities in hierarchies, multiple objectives and fuzzy sets. 15(3):234–281, 1977.

[52] D. Shen and C. Davatzikos. Hammer: hierarchical attribute matching mechanism for elastic registration. *IEEE Trans. on Medical Imaging*, 21(11):1421–1439, Dec 2002.

[53] Brett A. Simon. Regional ventilation and lung mechanics using x-ray ct. *Academic Radiology*, 12(11):1414–1422, 2005.

[54] Brett A. Simon, Gary E. Christensen, Daniel A. Low, and Joseph M. Reinhardt. Computed tomography studies of lung mechanics. *Proc Am Thorac Soc*, 2:517–521, 2005.

[55] Hemant D. Tagare. Shape-based nonrigid correspondence with application to heart motion analysis. *IEEE Trans. Med. Imaging*, 18(7):570–579, July 1999.

[56] J. Talairach and P. Tournoux. *Co-Planar Stereotactic Atlas of the Human Brain.* Beorg Thieme Verlag, Stuttgart, 1988.

[57] J.P. Thirion. Image matching as a diffusion process: an analogy with maxwell's demons. *Medical Image Analysis*, 2:243–260, 1998.

[58] P.M. Thompson, D. MacDonald, M.S Mega, C.J. Holmes, A.C. Evans, and A.W. Toga. Detection and mapping of abnormal brain structure with a probabilistic atlas of cortical surfaces. *Journal of Computer Assisted Tomography*, 21(4):567–581, 1997.

[59] P.M. Thompson and A.W. Toga. A surface-based technique for warping three-dimensional images of the brain. *IEEE Transactions on Medical Imaging*, 15(4):1–16, 1996.

[60] Duygu Tosun and Jerry L. Prince. Cortical surface alignment using geometry driven multispectral optical flow. In Gary E. Christensen and Milan Sonka, editors, *Information Processing in Medical Imaging*, Berlin, July 2005. Springer-Verlag.

[61] M. Unser. Splines: A perfect fit for signal and image processing. *IEEE Signal Processing Magazine*, 16:22–38, 1999.

[62] Marc Vaillant and Joan Glaunès. Surface matching via currents. In Gary E. Christensen and Milan Sonka, editors, *Information Processing in Medical Imaging*, pages 381–392, Berlin, July 2005. Springer-Verlag.

[63] Kelvin Woods, Yue Wang, Li Fan, and Chang Wen Chen. Model supported image registration and warping for change detection in computer-aided diagnosis. In *29th Applied Imagery Pattern Recognition Workshop*, pages 180–186, October 2000.

[64] R.P. Woods, S.T Grafton, C.J. Holmes, S.R. Cherry, and J.C. Mazziotta. Automated Image Registration: I. General Methods and Intrasubject, Intramodality Validation. *Journal of Computer Assisted Tomography*, 22(1):139–152, 1998.

[65] Li Zhang and Joseph M. Reinhardt. 3d pulmonary ct image registration with a standard lung atlas. In C. Chen and A. Clough, editors, *SPIE Conf. Medical Imaging*, pages 67–77, Feb. 2000.